Volume 18
Number 12
26 March 2026
Pages 6125-6632

Nanoscale

rsc.li/nanoscale

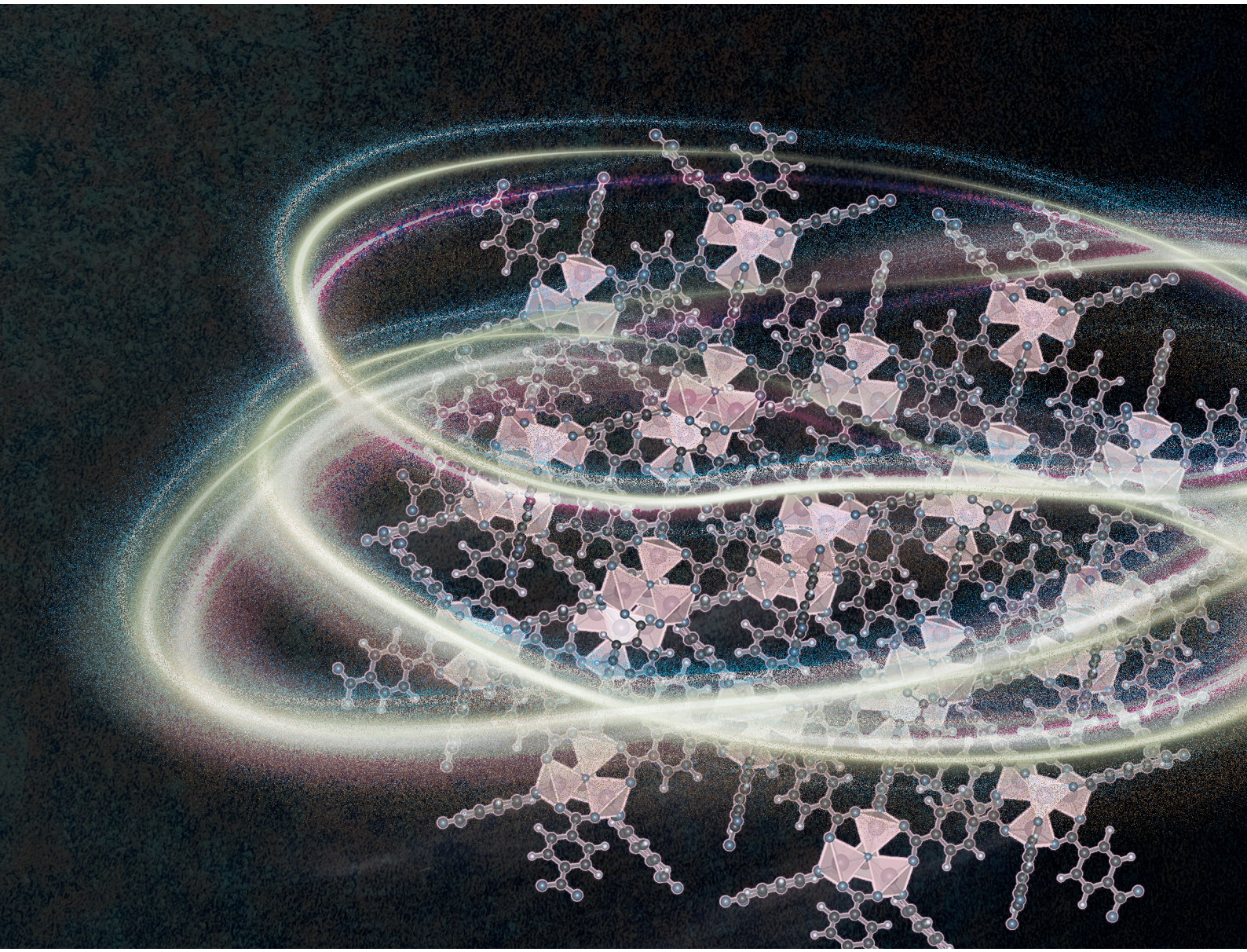

ISSN 2040-3372

ROYAL SOCIETY OF CHEMISTRY

REVIEW ARTICLE
Santosh U. Sharma and Hung-Ju Yen
Conductive metal–organic frameworks: emerging strategies for high-performance energy storage

NCNST

Nanoscale

REVIEW

View Article Online
View Journal | View Issue

Cite this: *Nanoscale*, 2026, **18**, 6139

Conductive metal–organic frameworks: emerging strategies for high-performance energy storage

Santosh U. Sharma and Hung-Ju Yen *

Conductive metal–organic frameworks (c-MOFs) have emerged as a distinctive class of crystalline, electronically active materials that bridge molecular design with electrochemical energy-storage functionality. Their significance is underscored by the recent Nobel Prize in Chemistry recognizing pioneering advances in MOF chemistry, which highlights the transformative impact of reticular design on modern materials science. Unlike conventional MOFs, whose insulating coordination bonds limit charge transport, c-MOFs integrate extended π–d conjugation, redox-active metal nodes, and permanent porosity to enable simultaneous electronic and ionic transport within an ordered framework. This review critically examines the fundamental charge-transport mechanisms governing c-MOFs-including through-bond, through-space, mixed-valence, and guest-mediated pathways-and elucidates how coordination geometry, defect chemistry, pore topology, and interfacial structure collectively regulate charge mobility and redox accessibility. By systematically linking these structure–property relationships to device-level behavior, we compare the performance of c-MOFs across lithium-, sodium-, and potassium-ion batteries, metal–air systems, supercapacitors, and redox-flow batteries, while clarifying their advantages and intrinsic limitations relative to carbons, metal oxides, conducting polymers, and perovskites. Particular emphasis is placed on identifying which conduction mechanisms and framework architectures remain most effective under practical operating conditions, including high areal loading, extended cycling, and commercial electrolytes. Beyond summarizing recent advances, this review provides a critical perspective on unresolved challenges-such as durability, scalable synthesis, and interfacial compatibility-and outlines emerging strategies, including hierarchical pore engineering, hybrid MOF-based architectures, data-driven materials discovery, and chemistry-conserving scale-up routes, that define concrete pathways toward deployable energy-storage technologies.

Received 16th December 2025,
Accepted 25th February 2026

DOI: 10.1039/d5nr05297a

rsc.li/nanoscale

1. Introduction

Metal organic frameworks (MOFs) represent one of the most transformative families of materials to emerge from modern chemistry.[1–6] Built from metal ions or clusters linked together by organic ligands, they embody the core philosophy of reticular chemistry: taking simple, well-defined molecular pieces and stitching them into extended, predictable architectures.[7–10] This modularity gives MOFs an almost unmatched degree of structural freedom.[11] Chemists can fine-tune pore size, shape, and chemical environment simply by choosing different linkers, metals, or synthetic routes, allowing precise control over both geometry and functionality.[12–14] Over the years, this design strategy has led to a breathtaking expansion of the field. What began as a curiosity-porous coordination solids-quickly evolved into a vast library of crystalline networks, now numbering in the tens of thousands. These structures span one-, two-, and three-dimensional frameworks, from rigid open lattices to flexible"-breathing" architectures that respond to external stimuli.[15–17] Their exceptional surface areas, tunable pore apertures, and chemically programmable interiors set them apart from traditional porous materials such as zeolites or activated carbons, which offer far less freedom in design.[18–20] Because of this tunability, MOFs have steadily moved from academic curiosity to practical relevance. They have become powerful platforms for gas storage[21,22] and separation,[22,23] selective catalysis,[24,25] environmental remediation,[26–28] drug delivery,[29–32] and sensing technologies.[33–36] In many cases, their performance stems from features that are difficult to achieve simultaneously in other materials-high crystallinity, open metal sites, tailored functional groups, and well-defined diffusion pathways.[37–39] As a result, MOFs are no longer just a new branch of materials chemistry; they are now central to discussions on sustainable energy,[40] clean technologies,[41] and next-generation molecular devices.[40,42]

1.1 Evolution of MOFs: from structural materials to functional frameworks

The journey of MOFs began with archetypal systems such as MOF-5 ($Zn_4O(BDC)_3$)[43] and HKUST-1 ($Cu_3(BTC)_2$),[44,45] which

Institute of Chemistry, Academia Sinica, 128 Academia Road, Section 2, Nankang, Taipei 11529, Taiwan. E-mail: hjyen@gate.sinica.edu.tw

demonstrated that coordination chemistry could produce permanently porous crystalline materials.[46] The subsequent development of the MIL series, including MIL-101(Cr)[47] and MIL-53 (Al),[48] introduced frameworks with high stability, flexibility, and functional tunability. Parallel advances in zeolitic imidazolate frameworks (ZIFs)[49] and covalent organic frameworks (COFs)[50] expanded the structural toolkit, offering new topologies and chemical robustness. Over time, the field evolved from simply making new structures to engineering new functions. Researchers began introducing redox-active centres, catalytic moieties, and photo-responsive linkers, transforming MOFs from passive hosts to chemically active materials.[51] This functionalization enabled MOFs to act as heterogeneous catalysts, photocatalysts, and platforms for energy conversion reactions.[52] Yet, despite their architectural sophistication, conventional MOFs were limited by a key drawback-their inherently poor electrical conductivity.[53,54] With conductivities often below 10^{-8} S cm^{-1}, charge transport in early MOFs was largely confined to localized hopping between guest molecules or metal sites, rather than through the framework itself.[55] This insulating nature severely restricted their use in electrochemical and electronic applications, where efficient electron mobility is essential.

The search for electrically active frameworks therefore became a defining challenge: could one design a MOF that maintained crystallinity and porosity while allowing electrons to flow freely? This question catalyzed a new era of research-one that merged solid-state physics with coordination chemistry and gave rise to a transformative subclass of materials: conductive metal–organic frameworks.

The Fig. 1 illustrates the chronological evolution of metal–organic frameworks, tracing how the field expanded in both structural sophistication and functional capability over the past four decades. Early porous MOFs, developed around the 1980s, primarily served as crystalline hosts for gas storage and molecular separation.[56] By the 2000s, growing synthetic control enabled the creation of functional and redox-active MOFs, which opened pathways for catalysis, chemical sensing, and selective adsorption.[57] The emergence of conductive MOFs around 2020 marked a major paradigm shift, demonstrating that extended π–d electronic communication could coexist with permanent porosity.[58] This breakthrough unlocked new electrochemical applications, including electrocatalysis,[59] supercapacitors,[60] and rechargeable Li/Na batteries.[61] Building on these advances, the current era (2025 onward) has seen the rise of hybrid and smart MOFs-such as MOF composites,[62] MOF@MXenes,[63] MOF@graphene systems,[63] and bio-MOFs[64]-which integrate multiple material classes to achieve synergistic performance. At the frontier, AI-driven MOF design, flexible energy-storage architectures, and solid-state ionic conductors are shaping the next generation of MOF-based technologies. Together, this timeline highlights how MOFs have progressed from simple porous networks to multifunctional and electronically active materials tailored for advanced energy applications.

1.2 Emergence of conductive MOFs: bridging structure and electronics

The emergence of conductive MOFs reshaped the scope of reticular chemistry by demonstrating that crystalline porous networks could simultaneously sustain long-range electronic transport. The central idea was straightforward yet transformative: engineer intentional orbital overlap between metal d-orbitals and π-conjugated ligands to generate continuous pathways for charge movement. This required careful selection of planar, π-extended linkers, redox-active metal centers, and short coordination distances all of which promoted efficient π–d conjugation. Importantly, these design choices amplified electronic conductivity while retaining the chemical tunability and structural diversity that define traditional MOFs (Fig. 2).

Santosh U. Sharma

Dr Santosh U. Sharma completed his PhD in polymeric materials chemistry for energy storage applications, such as lithium-ion batteries and supercapacitors, under the guidance of Prof. Jyh-Tsung Lee at National Sun Yat-sen University, Taiwan. He holds an MS in Industrial Polymer Chemistry and a BS in Chemistry, both from the University of Mumbai, India. Currently, he is a Postdoctoral Researcher at the Institute of Chemistry, Academia Sinica, Taiwan, working in Dr Hung-Ju Yen's group. His research interests include the development and synthesis of redox-active molecules, including small molecules, polymers, and porous materials, for batteries and supercapacitors.

Hung-Ju Yen

Dr Hung-Ju Yen is currently an Associate Research Fellow at Academia Sinica. He earned his B.S. and M.S. from National Chi Nan University and then completed his Ph.D. degree from National Taiwan University (NTU) in 2011. He joined Los Alamos National Laboratory as the J. Robert Oppenheimer Fellow (2013–2017) after postdoctoral training at NTU (2011, 2012–2013). Dr Yen joined Academia Sinica as an assistant research fellow in 2017 and was promoted to associate research fellow in 2025. Dr Yen's main research interest lies in the bottom-up chemical synthesis of nanographenes and electroactive high-performance polymers for optoelectronic and energy applications.

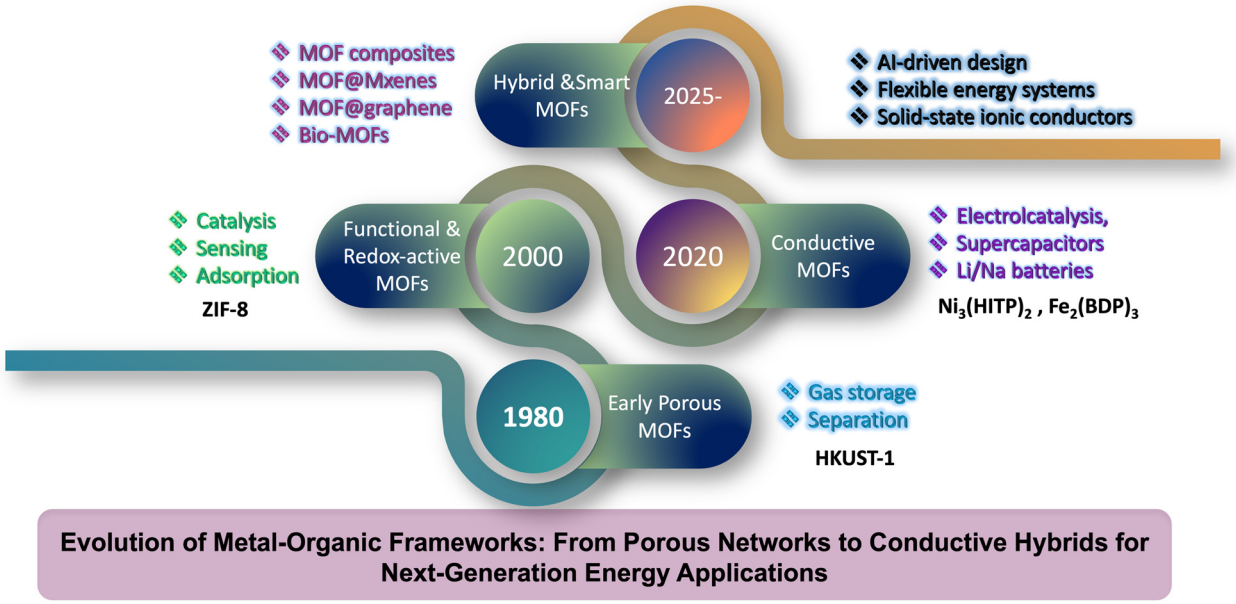

Fig. 1 Chronological roadmap illustrating the transformation of MOFs from basic porous networks to redox-active and electronically conductive frameworks, ultimately leading to multifunctional hybrid MOFs. The expanding application landscape from adsorption and catalysis to supercapacitors, batteries, and electrocatalysis reflects the increasing structural and electronic sophistication of MOFs. Future opportunities lie in AI-guided discovery, flexible power systems, and solid-state ion conductors.

A decisive breakthrough came in 2014, when Sheberla *et al.* introduced **$Ni_3(HITP)_2$** (HITP = 2,3,6,7,10,11-hexaiminotriphenylene), a two-dimensional honeycomb lattice-exhibiting strong in-plane π–d interactions and intrinsic conductivities approaching 40 S cm^{-1}.[73] This was the first clear evidence that porosity, crystallinity, and long-range electronic communication could coexist within a single framework. Soon after, the closely related $Cu_3(HHTP)_2$ (HHTP = 2,3,6,7,10,11-hexahydroxytriphenylene) was reported, displaying similar metallic-like conduction combined with accessible redox activity.[74] Together, these early 2D c-MOFs established a structural blueprint for electronically active coordination solids. Progress continued rapidly. In 2016, Fe_2(DEBDC) (DEBDC = 1,4-dioxido-2,5-benzenedicarboxylate) highlighted how mixed-valence Fe sites could facilitate electron hopping, broadening the design landscape for semiconducting MOFs.[75] By 2018 donor–acceptor systems incorporating tetrathiafulvalene (TTF), porphyrin, and phthalocyanine linkers enabled deliberate bandgap modulation reaching values as low as ~0.2 eV and introduced pronounced photo- and electroactive behaviors.[76] These advances confirmed that c-MOFs could be tuned with a precision similar to that of molecular and polymeric semiconductors.

A shift toward device relevance occurred around 2020, when thin-film $Ni_3(HITP)_2$ micro-supercapacitors delivered high arealcapacitances, rapid charge dynamics, and mechanical flexibility.[77] Their performance demonstrated that c-MOFs were not merely model systems but viable candidates for functional electronics and energy storage. From 2021 to 2024, the field expanded toward hybrid architectures-including MOF/rGO,[78–85] MOF/MXene,[86–90] and MOF@COF[91–95] composites-which integrated intrinsic c-MOF conductivity with improved mechanical strength, hierarchical transport channels, and more scalable processing. Together, these milestones established c-MOFs as a versatile platform at the intersection of molecular design and applied electronics, offering tunable pathways for charge transport while preserving the modularity that makes MOFs unique.

1.3 Chemistry–function relationship and emerging applications of c-MOFs

The unique performance of c-MOFs arises from a tight chemistry–function coupling, where electronic delocalization, redox activity, and intrinsic porosity operate together rather than as isolated features. The deliberate overlap of metal-centered d-orbitals with π-conjugated ligand states establishes both through-bond and through-space conduction pathways. At the same time, incorporating redox-active centers such as Ni^{2+}/Ni^{3+}, Fe^{2+}/Fe^{3+}, Co^{2+}/Co^{3+}, and Cu^{2+}/Cu^{3+} enables mixed-valence charge transport.[96,97] Complementing these electronic features, the open channels inherent to the framework allow ion migration and electrolyte penetration, producing a bi-continuous architecture for simultaneous ion and electron movement. This dual-transport nature sets c-MOFs apart from dense inorganic semiconductors and conventional insulating MOFs. These intertwined electronic and structural attributes make c-MOFs particularly well-suited for electrochemical energy storage. As electrodes in lithium-, sodium-, or potassium-ion batteries, they offer uniformly distributed redox centers and continuous charge-transport pathways. Their π-conjugated linkers stabilize injected charges and help buffer

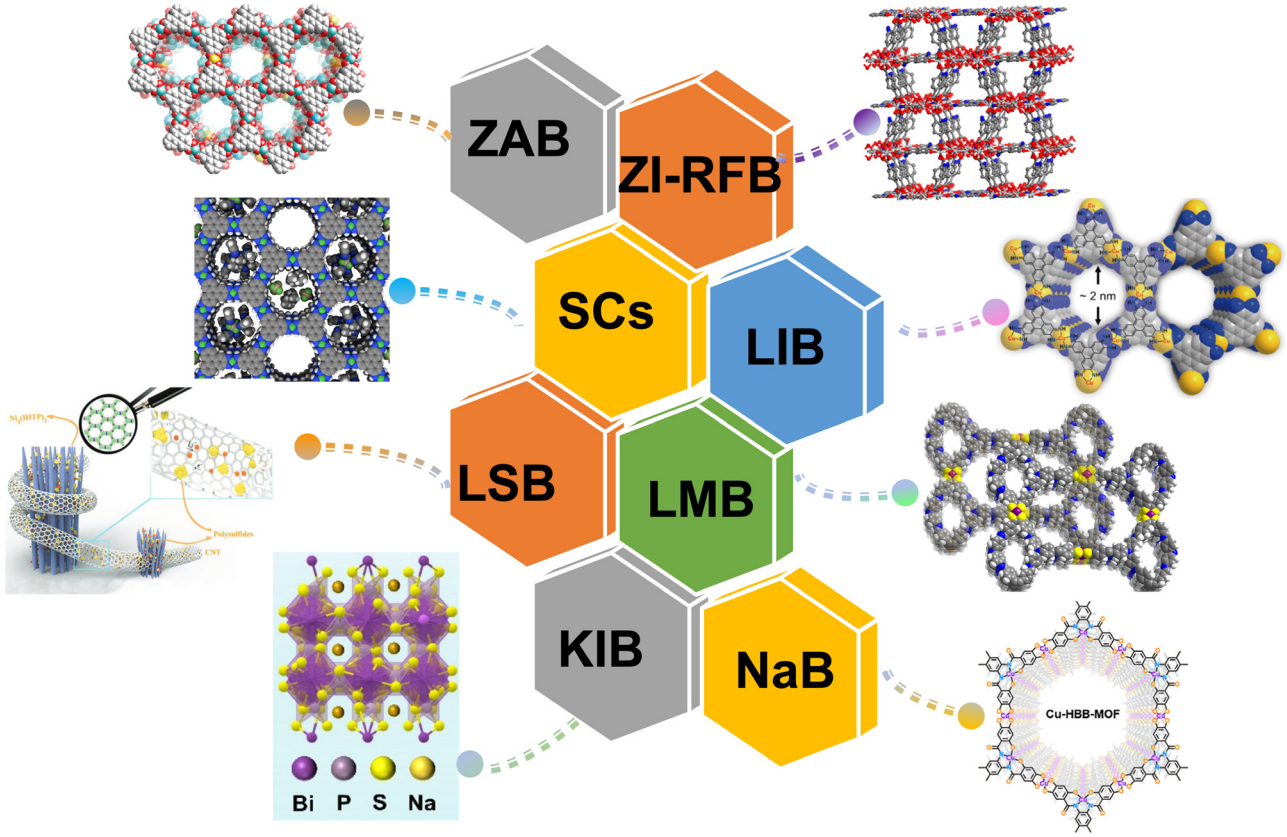

Fig. 2 Representative classes of conductive MOFs (c-MOFs) employed across diverse electrochemical energy-storage systems, including zinc-air batteries (ZABs) Reproduced with permission from ref. 65 Copyright 2014 American Chemical Society. Redox-flow batteries (RFBs) Reproduced with permission from ref. 66 Copyright 2015 John Wiley and Sons. Supercapacitors (SCs) Reproduced with permission from ref. 67 Copyright 2015 American Chemical Society. Lithium-ion batteries (LIBs) Reproduced with permission from ref. 68 Copyright 2025 Elsevier. Lithium–sulfur batteries (LSBs) Reproduced with permission from ref. 69 Copyright 2020 Elsevier. Lithium-metal batteries (LMBs) Reproduced with permission from ref. 70 Copyright 2016 Royal Society of Chemistry. Sodium-ion batteries (SIBs) Reproduced with permission from ref. 71 Copyright 2017 Elsevier, and potassium-ion batteries (PIBs) Reproduced with permission from ref. 72 Copyright 2016 Royal Society of Chemistry.

structural strain during cycling, enabling high reversible capacities and strong rate performance. In supercapacitors, 2D frameworks such as $Ni_3(HITP)_2$ and $Cu_3(HHTP)_2$ exhibit metallic-level conductivities together with large numbers of accessible electroactive sites.[98] Their ordered nanopores promote fast ion diffusion, while electronically delocalized layers support rapid electron transport-resulting in hybrid capacitive behaviours that merge the advantages of electrical double-layer capacitors with the higher energy density of faradaic systems.[99]

Beyond storage devices, c-MOFs have emerged as efficient electrocatalysts.[59] Their conjugated metal–ligand motifs generate electronically coupled active sites capable of mediating charge transfer during catalytic turnover. Ni-, Co-, and Fe-based frameworks have shown notable performance in oxygen evolution and hydrogen evolution reactions, whereas Fe- and Cu-containing analogues demonstrate promising activity and selectivity in CO_2 reduction and oxygen reduction.[100,101] The permanent porosity ensures continuous access for reactants and facilitates rapid removal of products, while the crystalline order stabilizes active sites more effectively than amorphous metal oxides, hydroxides, or sulfides.[102] Growing interest is also directed toward thermoelectric, optoelectronic, and sensing applications.[104] Their tunable band structure, adjustable carrier density, and intrinsically low thermal conductivity make c-MOFs appealing for thermoelectric energy conversion.[105] Porphyrin- and phthalocyanine-based frameworks, with strong optical absorption and favourable charge-separation behaviour, show potential in photodetectors and solar-energy harvesting devices.[106] Additionally, their conductivity responds sharply to external stimuli-including gas adsorption, humidity fluctuations, and mechanical strain-enabling high-performance chemiresistive and piezoresistive sensors.

Crucially, the modular chemistry of MOFs allows these properties to be tailored through metal–ligand substitution, heterometal incorporation, guest doping, or post-synthetic modification, all while preserving crystallinity. Such molecular-level control over charge density, bandgap, and active-site distribution is rarely achievable in traditional inorganic solids. Consequently, c-MOFs serve as a powerful bridge between coordination chemistry and solid-state electronics, offering a unified platform where structure, function, and performance are fundamentally interconnected (Fig. 3).

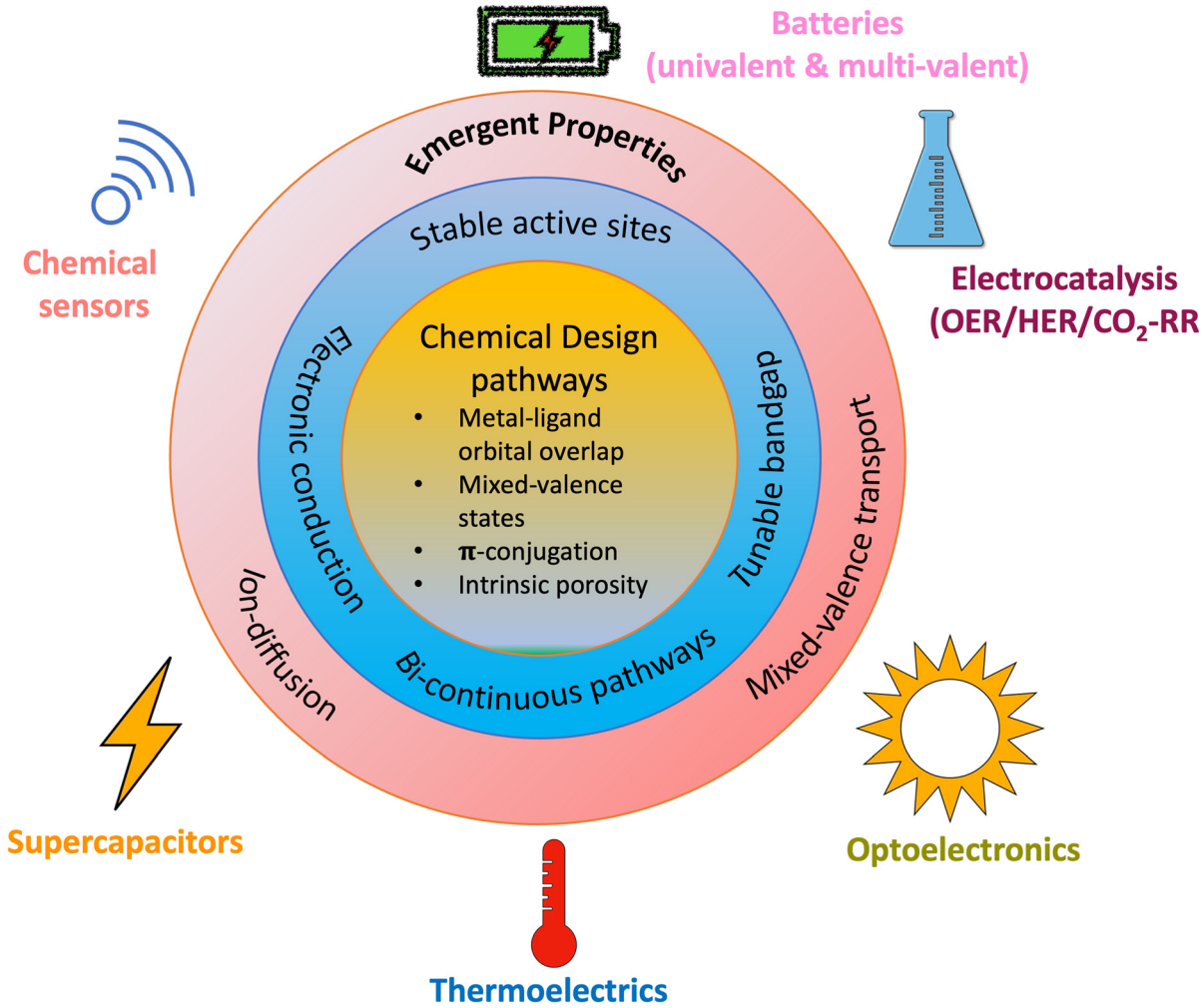

Fig. 3 A unified framework illustrating how fundamental chemical design principles in c-MOFs translate into emergent charge-transport and catalytic properties, which in turn drive their versatility across energy and electronic applications. The synergy between orbital engineering, mixed-valence chemistry, and intrinsic porosity underpins their performance in batteries, electrocatalysis, supercapacitors, thermoelectric, optoelectronics, and chemical sensing.

Despite rapid progress, many recent reviews on conductive MOFs have tended to focus on isolated aspects, such as record electrical conductivities, specific linker chemistries, or individual device demonstrations. Comparatively less attention has been paid to systematically connecting fundamental charge-transport mechanisms with structure–property–performance relationships across different c-MOF families and energy-storage platforms. As a result, design principles that translate molecular-level conductivity into durable, scalable device performance remain fragmented. This review addresses this gap by integrating mechanistic understanding, quantitative performance comparisons, and device-relevant considerations into a unified framework.[107–109]

It is important to explicitly distinguish conductive MOFs from both conventional insulating MOFs and MOF-derived materials. Traditional MOFs typically exhibit negligible intrinsic electronic conductivity and function primarily as porous hosts, ion reservoirs, or sacrificial templates in energy-storage systems. In such cases, charge storage is often mediated by guest species, surface reactions, or by conversion to conductive derivatives during cycling. In contrast, conductive MOFs are deliberately designed so that the framework itself participates directly in charge transport through extended π–d conjugation, mixed-valence metal centers, or through-space electronic coupling, enabling simultaneous electron and ion transport within an intact crystalline lattice. MOF-derived materials represent a fundamentally different class, where thermal or chemical transformation destroys the reticular framework and yields conductive carbons or inorganic phases whose properties are governed by conventional solid-state mechanisms rather than coordination chemistry. This review therefore treats c-MOFs as a distinct materials platform that bridges molecular design and solid-state electronics, while MOF-derived materials are discussed separately as framework-templated conductive architectures.

1.4 Scope of this review

This review provides a comprehensive overview of conductive MOFs as a rapidly expanding class of materials for high-performance energy storage and related electrochemical technologies. We first discuss the fundamental principles that govern charge transport in framework solids (Section 2), establishing the concepts necessary to understand electronic conduction in c-MOFs. Section 3 examines the synthetic and post-synthetic strategies used to tailor their electrical behavior, coordination environment, and structural features. Building on these foundations, Sections 4–5 analyze structure–property–performance relationships and highlight major advances in batteries, supercapacitors, and hybrid energy storage systems. In the final part of the review, we outline emerging opportunities-including computational screening, hybrid material design, and flexible device integration-and discuss how c-MOFs may transition from conceptual frameworks to practical, scalable components in next-generation sustainable energy technologies.

While several excellent reviews published in the past 3–5 years have focused on the synthesis, conductivity enhancement, or electrochemical performance of conductive MOFs, the present work offers a complementary and distinct perspective. Rather than cataloguing materials or device metrics alone, this review systematically connects charge-transport mechanisms, framework chemistry, and structure–property–performance relationships across different energy-storage platforms. Particular emphasis is placed on (i) differentiating intrinsic framework conductivity from guest- or derivative-dominated transport, (ii) identifying recurring structural motifs that govern durability and ion–electron coupling, and (iii) evaluating scalability, reproducibility, and interfacial limitations that are often underrepresented in prior reviews. By integrating mechanistic understanding with device-relevant constraints and emerging data-driven design strategies, this review aims to provide a unified framework for translating conductive MOFs from molecular design to practical energy-storage systems.

2. Mechanisms of conductivity in metal–organic frameworks

Electrical conductivity in metal–organic frameworks arises from the migration of charge carriers-electrons, holes, or ions-through extended networks of metal nodes and organic linkers. In contrast to inorganic solids, where strong metallic or covalent bonds create continuous electronic bands, most conventional MOFs exhibit poor electrical transport because their coordination bonds are predominantly ionic or σ-type, which greatly limits orbital overlap. As a result, pristine MOFs typically function as porous insulators rather than electronic conductors.

In contrast to conventional MOFs, conductive MOFs are deliberately designed to overcome charge localization by promoting strong electronic coupling across the framework. While conventional MOFs rely on largely ionic or σ-type metal–ligand coordination that confines charge carriers to isolated nodes or linkers, conductive MOFs incorporate π-conjugated ligands, redox-active metal centers, or mixed-valence motifs that enable efficient charge delocalization. This design shift transforms charge transport from thermally activated hopping between localized states into band-like or strongly coupled transport pathways, depending on framework topology and orbital alignment. As a result, conductive MOFs exhibit fundamentally distinct charge-transport mechanisms that underpin their superior electrochemical performance in energy-storage applications.

Over the past decade, however, deliberate molecular engineering has led to the emergence of conductive MOFs capable of bypassing these intrinsic limitations. Through strategic design of metal–ligand coordination geometry, incorporation of π-conjugated linkers, control of redox-active centres, and introduction of guest charge carriers, researchers have established well-defined pathways that enable efficient charge transport. This shift has transformed MOFs from passive host lattices into tunable electronic materials with properties that rival organic conductors, carbon materials, and even some inorganic semiconductors. Moreover, the modular nature of reticular chemistry allows researchers to fine-tune these electronic pathways with atomic precision, enabling conductivity enhancements that would be difficult to achieve in traditional materials.

A deeper understanding of these conduction principles is crucial, not only for improving intrinsic charge mobility but also for translating molecular structure into practical electrochemical performance in batteries, supercapacitors, and electrocatalytic systems. Charge transport in MOFs is inherently structure-dependent, and small modifications in linker planarity, metal–ligand orbital alignment, or stacking behaviour can drastically alter macroscopic conductivity by several orders of magnitude. Additionally, the porous nature of MOFs introduces opportunities unavailable in dense crystals: charge carriers can be stabilized, shuttled, or modulated by encapsulated guests, solvated ions, or redox-active molecules that reside within the framework channels.

Collectively, four principal mechanisms govern conductivity in MOFs: through-bond, through-space, mixed-valence, and guest-mediated or ionic transport. Through-bond conduction relies on continuous π–d conjugation between metal centres and planar linkers, promoting band-like delocalization. Through-space pathways instead utilise π–π stacking between adjacent 2D sheets, enabling vertical hopping of electrons across layers. Mixed-valence systems exploit variable oxidation states within the framework to facilitate intervalence charge transfer. Finally, guest-mediated or ionic conduction leverages mobile ions or redox-active molecules residing in the pores to provide additional transport pathways independent of the structural backbone.

Each mechanism offers unique advantages and tuning parameters for energy-storage applications (Fig. 4). Through-bond systems afford high intrinsic conductivity, through-space stacking offers anisotropic transport favourable for layered

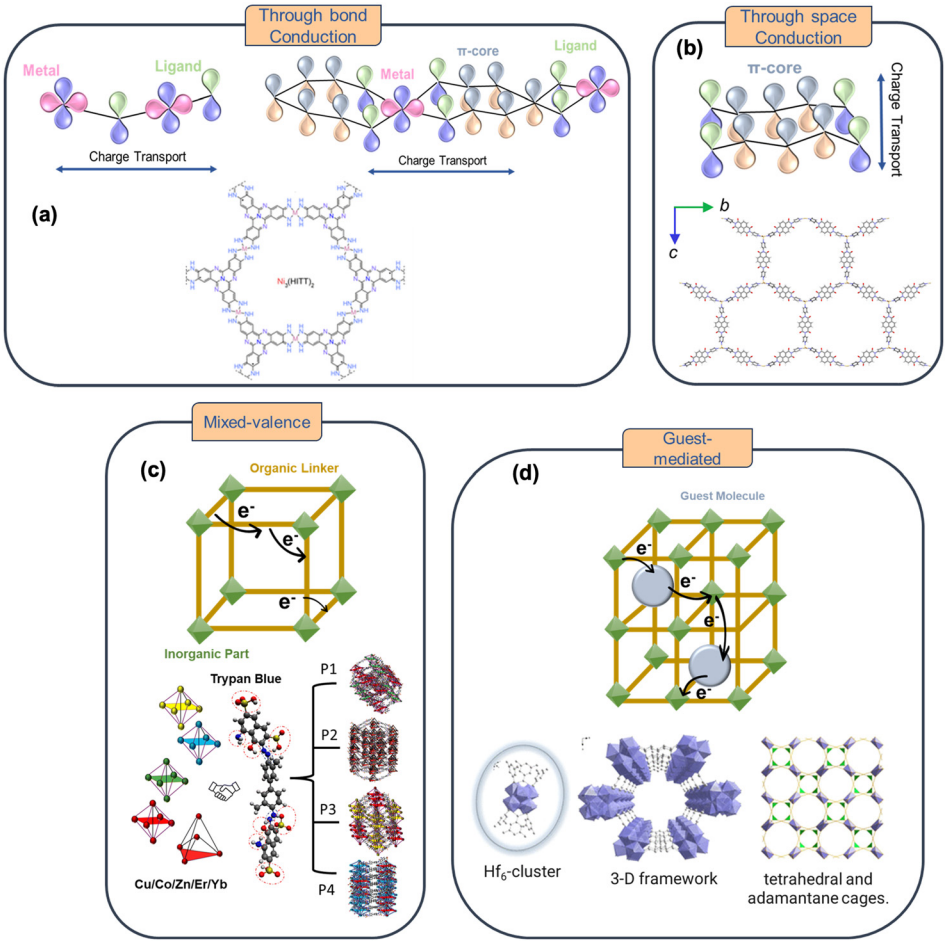

Fig. 4 Overview of charge-transport pathways in c-MOFs. Top panels: schematic representation of the fundamental conduction mechanisms: (a) through-bond transport arising from metal–ligand orbital coupling, (b) through-space transport enabled by π–π stacking between adjacent conjugated cores, (c) mixed-valence frameworks where intervalence transfer occurs through inorganic–organic linkages and (d) guest-mediated systems where encapsulated clusters or molecules create additional pathways for charge hopping within the framework Bottom panels: structural examples that correspond to each mechanism. Reproduced with permission from ref. 103 Copyright 2020 American Chemical Society.

electrodes, mixed-valence structures enable fast redox kinetics, and guest-mediated frameworks provide opportunities for dual electronic-ionic conduction. Understanding how these modes arise-and how they interplay-now forms the foundation for rational design of next-generation c-MOFs with precisely engineered electronic architectures.

2.1 Through-bond (band-type) conduction

This mechanism involves continuous π–d coupling between metal centers and conjugated ligands, creating delocalized bands like those in organic semiconductors. Planar geometries, partially filled d-orbitals, and rigid aromatic linkers maximize overlap, enabling metallic or narrow-gap semiconducting behavior.[113] Numerous MOF design strategies have therefore focused on enhancing this overlap by tuning the coordination environment or substituting metal-binding atoms to strengthen through-bond interactions.[114] As illustrated in Fig. 4a, early-generation MOFs with localized σ-type bonds exhibit poor electronic connectivity due to interrupted orbital overlap (left), whereas π-conjugated 2D frameworks with extended metal–ligand delocalization planes enable efficient band-type conduction (right). One widely adopted approach involves substituting the metal-coordinating atoms to strengthen metal–ligand interactions and thereby improve through-bond electronic conductivity.[103,115] A representative example of through-bond delocalization is observed in $Ni_3(HITT)_2$, a two-dimensional conductive MOF constructed from *ortho*-diamine-based HITT linkers. Diffuse-reflectance UV-vis-NIR spectroscopy reveals pronounced near-infrared absorption and a broad low-energy background, characteristic of extended π–d conjugation and the presence of delocalized charge carriers. The strong in-plane overlap between Ni^{2+} d orbitals and the conjugated π-system of the ligand promote the formation of a quasi-metallic conduction band, resulting in a room-temperature conductivity of 4.5 S cm^{-1}. The electronic coupling across the planar coordination network enables efficient charge transport within the layers, consistent with a granular-metal conduction model, where carrier delocalization dominates but is partially constrained by grain boundaries and interparticle effects.[116]

This mechanism is therefore most relevant for high-power energy-storage devices, such as supercapacitors and fast-charging battery electrodes, where low electronic resistance is critical.

2.2 Through-space (hopping) conduction

In frameworks lacking direct metal–ligand conjugation, electrons hop between localized redox sites *via* π–π stacking or guest bridges. The process follows Marcus-type kinetics, with the charge-transfer rate governed by the electronic coupling (V) and reorganization energy (λ).[120] A striking example of through-space charge transport is found in PMC-20, a flexible naphthalenediimide-based MOF that exhibits a unique quadruple stacking topology (Fig. 4b). The framework consists of wavy honeycomb sheets linked through Cd^{2+} nodes, where the π-conjugated NDI cores align vertically to form infinite columnar stacks. These closely packed π–π arrays provide continuous pathways for electron migration *via* orbital overlap rather than direct metal–ligand bonding. The flexible coordination environment of Cd^{2+} facilitates this tight stacking geometry, thereby enhancing intermolecular coupling and minimizing activation energy. As a result, PMC-20 achieves the highest electrical conductivity reported among single-crystalline NDI frameworks, underscoring the pivotal role of π–π stacking and framework flexibility in governing through-space charge transport within porous molecular conductors.[121] Although intrinsically slower than band-type transport, through-space conduction plays an important role in layered electrodes where redox accessibility and structural flexibility outweigh absolute conductivity.

2.3 Mixed-valence and metal-centered conduction

In mixed-valence frameworks containing metals with multiple oxidation states (*e.g.*, Fe^{2+}/Fe^{3+}, Co^{2+}/Co^{3+}), electron transport proceeds *via* intervalence hopping between adjacent nodes. The metal–ligand bridges mediate super exchange coupling, and partial delocalization yields semiconducting character.

A representative case of hopping-type electronic conduction is observed in Trypan Blue-based bimetallic MOFs (Cu–Co–Try, Cu–Zn–Try, Cu–Er–Try, Cu–Yb–Try), where multifunctional linkers containing amino, hydroxyl, azo, and sulfonate groups coordinate multiple metal nodes simultaneously (Fig. 4c). The coexistence of mixed 3d–3d and 3d–4f metal centers generates localized redox sites that facilitate intervalence charge transfer through a thermally activated hopping mechanism. Charge mobility values ranging from 10^{-7} to 10^{-3} $cm^2\ V^{-1}\ s^{-1}$ confirm the presence of localized electron hopping rather than delocalized band transport. The bimetallic Cu–Co and Cu–Zn systems exhibit higher conductivities and lower charge-transfer resistance compared to their 3d–4f counterparts, owing to stronger electronic coupling between transition-metal orbitals. Moreover, thermal treatment partially carbonizes the organic ligand, enhancing intermetallic connectivity and redox-driven conductivity. These findings underscore how multi-metallic coordination and mixed valence states can create synergistic hopping networks, offering tunable pathways for electron transfer and redox activity in conductive MOFs.[122] Such hopping-dominated mechanisms are particularly relevant for battery electrodes, where localized redox activity enables high capacity and long-term cycling stability.

2.4 Guest-mediated and ionic conduction

Mobile ions or redox-active guests confined within MOF channels can also mediate charge transport. Protonic conduction occurs through hydrogen-bond networks (*e.g.*, imidazole-based MOFs, $\sigma \approx 10^{-2}$ S cm^{-1}), while electron hopping can occur between guests such as TCNQ or I_3^-.[123] These hybrid conduction processes produce dual ionic–electronic pathways, beneficial for solid-state batteries where both Li^+ mobility and electronic continuity are required.

A representative system that highlights guest-assisted proton transport is Im@MOF-808(Hf), in which imidazole or triazole molecules were confined within the channels of a robust spin-type framework *via* post-synthetic sublimation (Fig. 4d). These heterocyclic guests generate continuous hydrogen-bond chains that enable Grotthuss-type proton hopping, boosting conductivity by nearly 27-fold compared with pristine MOF-808(Hf) (σ = 0.127 S cm^{-1} at 100 °C, 98% RH). At lower humidity, triazole-loaded analogues transition to a Vehicle mechanism, where proton diffusion proceeds through mobile carriers rather than fixed H-bond relays. This humidity-dependent switch clearly demonstrates how guest chemistry and pore polarity modulate ionic conduction pathways, providing a versatile approach for tuning transport properties without compromising framework stability. Such guest-mediated conduction unites molecular dynamics with solid-state transport, offering design principles for next-generation protonic and hybrid ionic-electronic MOFs in batteries and fuel-cell devices.[124] Guest-mediated conduction is especially relevant for solid-state and hybrid devices, where coupled ion-electron transport rather than purely electronic conductivity dictates performance.

2.5 Band-structure engineering and design implications

The electrical conductivity of metal–organic frameworks arises from a subtle interplay between dimensionality, orbital topology, and electronic coupling between metal nodes and organic linkers.[125] Two-dimensional lattices that promote extended π–d overlap typically exhibit metallic or small-band-gap semiconducting behavior, whereas three-dimensional frameworks depend on super-exchange or thermally activated hopping across orthogonal directions.[126] Structural modulation through reduced interlayer π–π separation, enhanced ligand planarity, or the introduction of heteroatoms such as sulfur, selenium, or nitrogen-can effectively tune the Fermi level and carrier effective mass, thereby controlling charge delocalization and band dispersion.[127]

Different conduction regimes correspond to distinct functional behaviors within MOFs. Band-type frameworks provide rapid electron transport suitable for high-rate electrochemical and catalytic processes; while hopping or mixed-valence systems favor localized redox activity that supports high charge

storage and catalytic turnover. Guest-mediated or ionic pathways bridge the gap between electronic and ionic transport, enabling coupled ion-electron conduction valuable for solid-state and hybrid devices.

Understanding how atomic geometry and electronic configuration dictate these band-structure features allows researchers to rationally design frameworks with tailored conductivity, optimized redox accessibility, and mechanical resilience. Such band-engineered MOFs hold promise not only for durable, high-performance energy-storage systems but also for emerging areas including electrocatalysis, sensing, photonics, and molecular electronics, where tunable charge transport is essential.

From a practical perspective, no single conduction mechanism alone defines device performance. Instead, the most effective c-MOFs for energy-storage applications combine delocalized electronic transport with ion-accessible porosity and redox-active sites. Band-type conduction governs power capability, mixed-valence and hopping mechanisms control capacity and reversibility, and guest-mediated pathways regulate ionic transport and interfacial stability. Recognizing this hierarchy allows conduction mechanisms to be selected and engineered according to the specific requirements of batteries, supercapacitors, and solid-state systems.

Critical insight: while multiple charge-transport mechanisms have been identified in conductive MOFs, their relevance to practical energy-storage devices is highly context dependent. Through-bond and mixed-valence mechanisms offer superior intrinsic conductivity, whereas through-space and guest-mediated pathways provide greater structural tolerance and ionic accessibility. Future efforts should prioritize mechanisms that balance electronic delocalization with framework stability under realistic electrochemical conditions.

3. Synthetic and post-synthetic strategies for conductive MOFs

The emergence of c-MOFs has shifted the role of MOFs from purely porous adsorbents to genuinely electronic materials. Turning an insulating coordination lattice into a mixed ionic-electronic conductor, however, demands careful control over coordination chemistry, π-conjugation, defect topology, and interfacial connectivity. Over the past decade, several design "levers" have crystallized: planar π-linkers that couple strongly to metal d-orbitals, redox-flexible metal centers, extrinsic dopants and guests that tune carrier density, engineered defects and heterointerfaces, and post-synthetic modifications that adjust all of the above without destroying crystallinity. Together, these strategies underpin the transition of MOFs into viable components for batteries, supercapacitors and electrocatalytic devices.

3.1 π-Conjugated linker design and band-structure engineering

In most c-MOFs, the organic linker is the primary highway for charge transport. Planar, rigid π-conjugated ligands overlap efficiently with the frontier d-orbitals of square-planar metals, forming extended π–d networks that enable band-type transport. Strong metal coordination enhances in-plane delocalization, while π–π stacking between layers supports vertical charge hopping as shown in Fig. 5a.[58] Hence, the rational design of π-planar ligands with optimized electronic densities is essential for achieving high-mobility c-MOFs. Reported conductivities span more than twelve orders of magnitude (10^{-10}–10^{2} S cm^{-1}), and this enormous spread is largely traced back to linker geometry, electronic structure, and stacking, rather than to porosity alone. Early archetypes such as $Ni_3(HITP)_2$ illustrate the key design rules. Triphenylene-based ligands enforce planarity and C_3 symmetry, while Ni^{2+} nodes provide an appropriate energy match for strong π–d coupling, giving bulk conductivities in the S cm^{-1} range (Fig. 5b).[127] Highly conjugated sheets derived from metalladithiolene or sulfur-rich ligands push this idea further: Ni-bis(dithiolene) nanosheets and Fe_2(DSBDC) chains, for example, (Fig. 5c) use soft S donors to strengthen metal–ligand overlap along $(M–S)_\infty$ backbones and move the electronic structure toward metallic behaviour.[111] Heteroatom content within the π-core is equally important. Nitrogen-rich ligands can either stabilize delocalisation or trap charge depending on how they reshape orbital energies.[110] The isostructural pair $Ni_3(HITAT)_2$ and $Ni_3(HITBim)_2$ is a nice illustration: both form 2D honeycomb lattices, but subtle differences in electron distribution across the truxene-type cores lead to dramatically different conductivities, from the mS cm^{-1} regime to tens of mS cm^{-1}. Post-synthetic mesylation of indole N–H sites in $Ni_3(HITAT)_2$ then shows how even small electron-withdrawing groups at the linker periphery can widen the bandgap, reduce carrier density and suppress conductivity by almost an order of magnitude.[73,74,111,112,132] Beyond O, N and S, heavier chalcogens such as Se have been proposed in π-cores to further soften the donor set and lower orbital energies, though their long-term framework stability is still being explored.[133,134] For example, catechol-functionalized hexa-*peri*-hexabenzocoronene (HBC) ligands afford Cu-HBC MOFs with multiple coordination centers; the c-HBC-12O-Cu variant exhibits a conductivity of 3.31 S m^{-1}, attributed to dense coordination and efficient charge percolation as shown in Fig. 5d.[112] Overall, π-linker design gives a direct handle on band dispersion, Fermi-level position, and carrier mobility, and is therefore the first and most powerful lever in c-MOF synthesis.

3.2 Metal-center selection and mixed-valence modulation

The metal center's electronic configuration and oxidation state strongly dictate charge transport in c-MOFs, since the frontier d-orbitals of the metal nodes directly couple with the π-orbitals of the ligands. Mixed-valence behavior, especially Robin–Day Class II and III regimes, creates efficient intervalence charge transfer (IVCT) and enables long-range electron mobility.[135] A classic benchmark is Prussian blue (Fe^{2+}/Fe^{3+}), which shows semiconductor-type conductivity *via* IVCT, illustrating the power of redox-active metal pairs.[136–138]

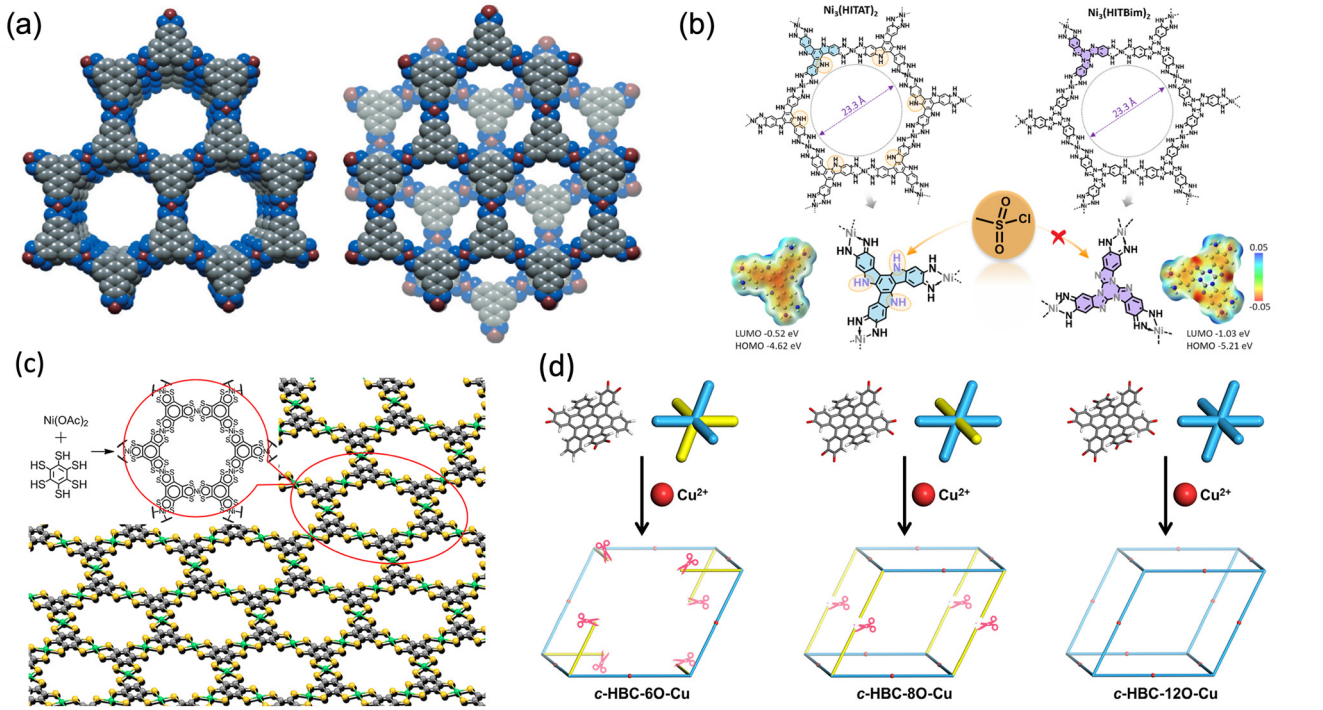

Fig. 5 Structural and electronic design strategies in π-conjugated c-MOFs. (a) Eclipsed and staggered stacking configurations in layered c-MOFs, highlighting the influence of interlayer packing on charge delocalization. Reproduced with permission from ref. 58 Copyright 2016 John Wiley and Sons. (b) Molecular structures of $Ni_3(HITAT)_2$ and $Ni_3(HITBim)_2$ with computed electrostatic potential maps and HOMO–LUMO levels, showing the electron-deficient character of HATBim and the effect of N heteroatom substitution on π–d coupling. Mesylation of indole N–H (bottom) demonstrates post synthetic tuning of conductivity *via* electron-withdrawing substitution. Reproduced with permission from ref. 110 Copyright 2023 American Chemical Society. (c) Structural model of Ni-bis(dithiolene) 2D sheets showing extended –S–Ni–S– conjugation. Reproduced with permission from ref. 111 Copyright 2013 American Chemical Society. (d) Schematic synthesis of c-HBC-Cu with 60°, 80°, and 120° linker geometries, illustrating coordination-angle control of pore topology and electronic connectivity. Reproduced with permission from ref. 112 Copyright 2023 American Chemical Society.

In MOFs, Fe-, Cu-, and Ni-based mixed-valent lattices are the most developed.[139] Early systems such as Fe-MIL-53·H_2O and Fe-MIL-100 demonstrated Fe^{3+}/Fe^{2+} interconversion coupled with Li^+ storage, while Fe(BDC)(DMF,F) and layered anilato frameworks showed Fe^{2+}/Fe^{3+} coexistence, leading to electron delocalization and even magnetic ordering.[140–142] Redox matching of metals and linkers further boosted conductivity: Dincă's replacement of O with S in DOBDC to form DSBDC enhanced Mn- and Fe-MOF conductivities by an order of magnitude due to infinite $(M–S)_n$ conduction chains.[75,143] Sun's $Fe(TRI)_2(BF_4)_x$ series pushed this further stoichiometric oxidation produced $Fe(TRI)_2(BF_4)_{0.33}$ with 0.3 S cm^{-1} conductivity (Fig. 6a).[58,117] Likewise, partial reduction of $Fe_2(BDP)_3$ to $K_xFe_2(BDP)_3$ delivered a 10 000-fold increase (to 0.025 S cm^{-1}) through defect-induced mid-gap states, and $Fe_2(BDT)_3$ achieved 1.8 S cm^{-1} single-crystal conductivity *via* continuous Fe–N–N chains and spontaneous Fe^{2+}/Fe^{3+} fluctuations.[144,145]

Mixed-valent copper systems display similar flexibility.[146] $Cu[Cu(PDT)_2]$ toggles between Cu(I)/Cu(III) and Cu(II)/Cu(II) states, showing IR-visible IVCT and 6×10^{-4} S cm^{-1} conductivity at 300 K.[147] Its analogue $Cu[Ni(PDT)_2]$ is less conductive (1×10^{-8} S cm^{-1}), but iodine oxidation quadruples its p-type conductivity, highlighting guest-controlled mixed valency.[148] Beyond single-metal systems, bimetallic design is equally powerful: in NiCo-MOF hollow spheres, partial substitution of Ni^{2+} with Co^{2+} increased conductivity 34-fold (0.0017 to 0.058 mS cm^{-1}) (Fig. 6b),[118] while NiCo-MOF/NiO core-shells generated internal electric fields that accelerated Ni^{2+}/Ni^{3+} redox kinetics and delivered 3010 mF cm^{-2} areal capacitance.[149] Hierarchical Ni/Co microspheres with a 1 : 2 ratio also showed reduced charge-transfer resistance and higher capacity (339 C g^{-1}).[150]

Together, these studies show that engineering the metal centre, through mixed valency, redox tuning, heterometallic substitution, or post-synthetic oxidation, effectively tailor's carrier pathways and pushes c-MOFs toward metallic-level conductivity while unlocking multifunctionality for catalysis, magnetism, and energy-storage applications.

3.3 Doping, guest intercalation, and defect engineering

Even when the linker-metal combination is favourable, the as-synthesized framework often sits in a low-conductivity state. Doping, guest intercalation, and controlled defect creation provide additional degrees of freedom to tune carrier density, Fermi-level position, and local transport pathways.

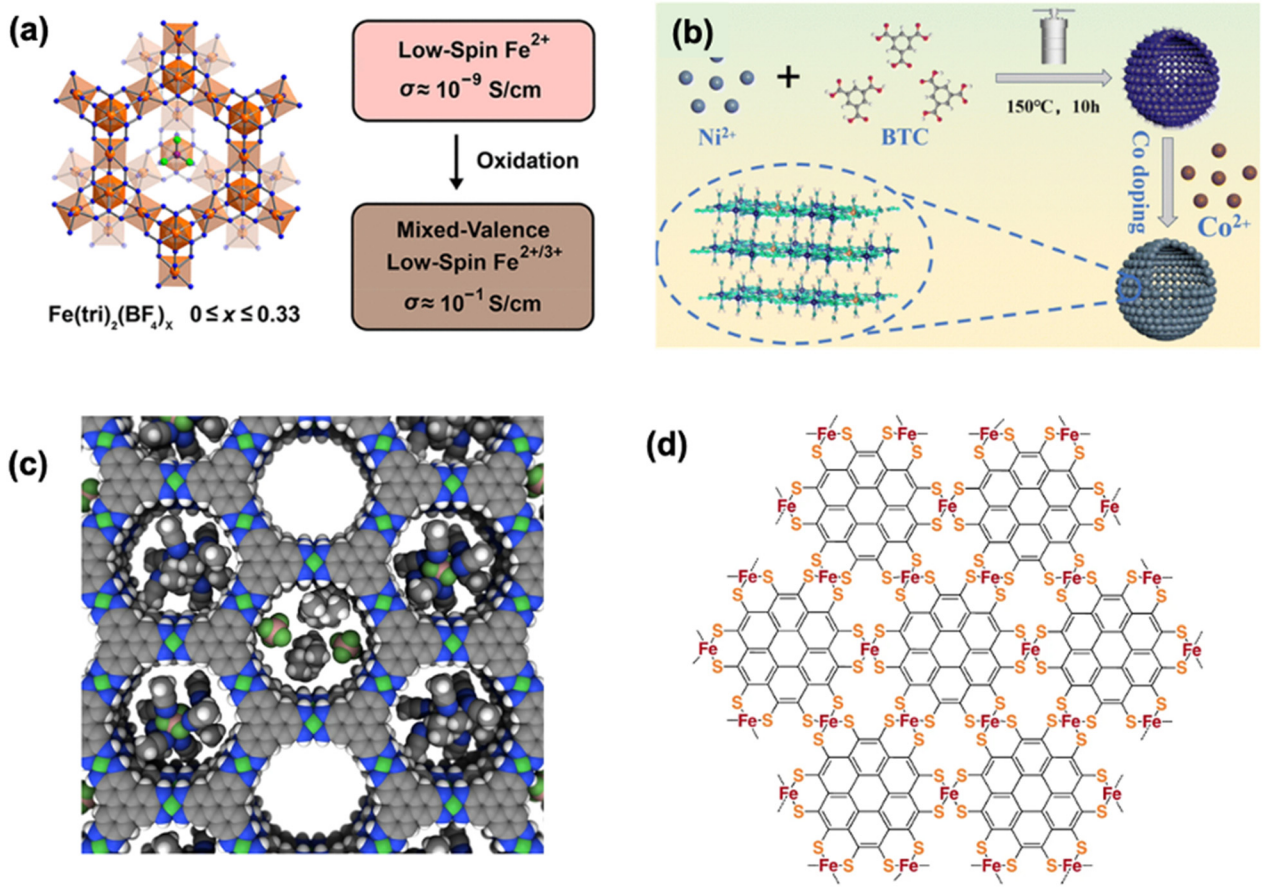

Fig. 6 (a) Mixed-valence sublattice of $Fe(tri)_2(BF_4)_x$ (tri^- = 1,2,3-triazolate; x = 0.09, 0.22, 0.33), illustrating the strong increase in electrical conductivity with higher iron oxidation states. Reproduced with permission from ref. 117 Copyright 2018 American Chemical Society. (b) Schematic of the NiCo-MOF synthesis route, showing how Co^{2+} incorporation refines the framework morphology and markedly boosts its electronic conductivity. Reproduced with permission from ref. 118 Copyright 2025 Royal Society of Chemistry. (c) Space-filling representation of idealized $Ni_3(HITP)_2$ highlighting the relative sizes of the framework pores compared to Et_4N^+ and BF_4^- ions and acetonitrile molecules-demonstrating that the large electrolyte species required for EDLC operation can be readily accommodated. Reproduced with permission from ref. 67 Copyright 2015 American Chemical Society. (d) Molecular structure of a 2D MOF synthesized solvothermally using perthiolated coronene linkers and iron-bis(dithiolene) nodes, enabling continuous π–d conjugation within the layered framework. Reproduced with permission from ref. 119 Copyright 2018 Nature.

Molecular dopants are a simple starting point. Oxidative doping of $Ni_3(HITP)_2$ with iodine vapour, for instance, increases conductivity several-fold by withdrawing electrons from the conjugated Ni–N network and introducing new hole carriers (Fig. 6c).[67] Charge-transfer guests such as TCNQ can boost conductivity by even larger factors: when TCNQ is infiltrated into a Co-porphyrin MOF or HKUST-1, donor–acceptor complexes form inside the pores, producing mid-gap states and enhancing π–π and through-bond coupling.[151] Electrochemical insertion of alkali cations into Fe-triazolate frameworks likewise tunes mixed valence *in situ*, raising conductivity by orders of magnitude as Fe^{2+}/Fe^{3+} populations are adjusted.[152,153]

A recent coronene-Fe(dithiolene) 2D c-MOF (Fig. 6d) further illustrates the role of defects in dictating electronic behaviour. Although its high conductivity (~10 S cm^{-1}) originates from a fully conjugated π–d network, grain boundaries, edge terminations, and vacancy-type defects were shown to influence magnetic coupling between Fe(III) centres, enabling low-temperature ferromagnetism. These results highlight that controlled defect landscapes-beyond classical chemical dopants or guest molecules-can serve as an additional lever for tuning charge transport and emergent spin properties in c-MOFs.[119]

Defects provide a more structural route to the same goal. Monocarboxylate modulators commonly used in solvothermal syntheses (acetic acid, formic acid, trifluoroacetic acid and so on) induce missing-linker or missing-cluster defects in archetypal systems such as HKUST-1[154] and UiO-66.[155,156] These defects generate coordinatively unsaturated metal sites and local strain fields that can lower activation barriers for charge hopping, change local band edges and, in some cases, create percolating networks of higher conductivity.[157] Post-synthetic treatments, acid/base etching, plasma exposure, mild thermal activation can further enrich oxygen vacancies or nanocrystalline domains, often narrowing the bandgap and improving both electronic and ionic transport. The challenge is to keep

defect density high enough to be electronically useful, but below the point where the lattice collapses or ion pathways become blocked.[128]

3.4 Hybrid and composite frameworks

A practical way to address the low conductivity and mechanical fragility of pristine MOFs is to hybridise them with conductive or robust secondary phases. This approach combines the high surface area and redox activity of MOFs with the electrical pathways and elasticity of carbon materials, metal oxides, or other MOFs, producing interconnected charge- and mass-transport architectures. A strong demonstration is the $BiPS_4$/C@Ni-HHTP composite, where Bi-MOF-derived $BiPS_4$/C pillars are coated with conductive Ni-HHTP nanorods (Fig. 7a). The Ni-HHTP shell traps polysulfides and forms a continuous electron network, while the carbonized Bi-MOF core absorbs sodiation strain' yielding 1063/1181 mAh g^{-1} at 0.1 A g^{-1} and 99% retention over 2000 cycles at 2 A g^{-1}.[128]

Further, biomass-derived hierarchical porous carbons are promising low-cost, sustainable supercapacitor materials owing to their conductivity and stability, though typically hindered by complex synthesis and low capacitance. Here, these limitations were overcome through the rational design of metal-enriched porous carbon nanotubes (M/p-CNTs, M = Cu, Co, W, Bi, Mo) *via* a green, one-pot ultrasonic impregnation of coconut silks in metal precursor solutions followed by nitrogen pyrolysis (Fig. 7b).[129] This process eliminates hazardous activation steps and drives nanotube formation through strong metal–carbon interactions, inducing metal electron deficiency. The resulting M/p-CNTs exhibit a high BET surface area (288.6 m^2 g^{-1}) and interconnected tri-modal porosity that enhances charge mobility and ion transport.[129] Similarly, in VY-MOF@CNT hybrids, sonication-assisted hydrothermal coupling of $V^{3+}/V^{4+}/Y^{3+}$ MOF nanoparticles with CNT networks creates hierarchical diffusion channels and dual charge-storage behaviour: electric-double-layer capacitance from CNTs and pseudocapacitance from the MOF. The resulting symmetric device delivers 60 Wh kg^{-1} at 1200 W kg^{-1} with 92% capacity retention after 10 000 cycles.[158] Similar enhancements appear in $FeCoS_2$@NC-G[159] and Co-MOF/Co_3O_4/rGO systems,[160] where carbon confinement prevents particle agglomeration and maintains electronic continuity. Beyond composite powders, electrochemically assisted self-assembly (EASA) enables room-temperature deposition of mesoporous MOF thin films on conductive substrates. These films consist of hexagonally ordered 3D microcrystals with 2D honeycomb-

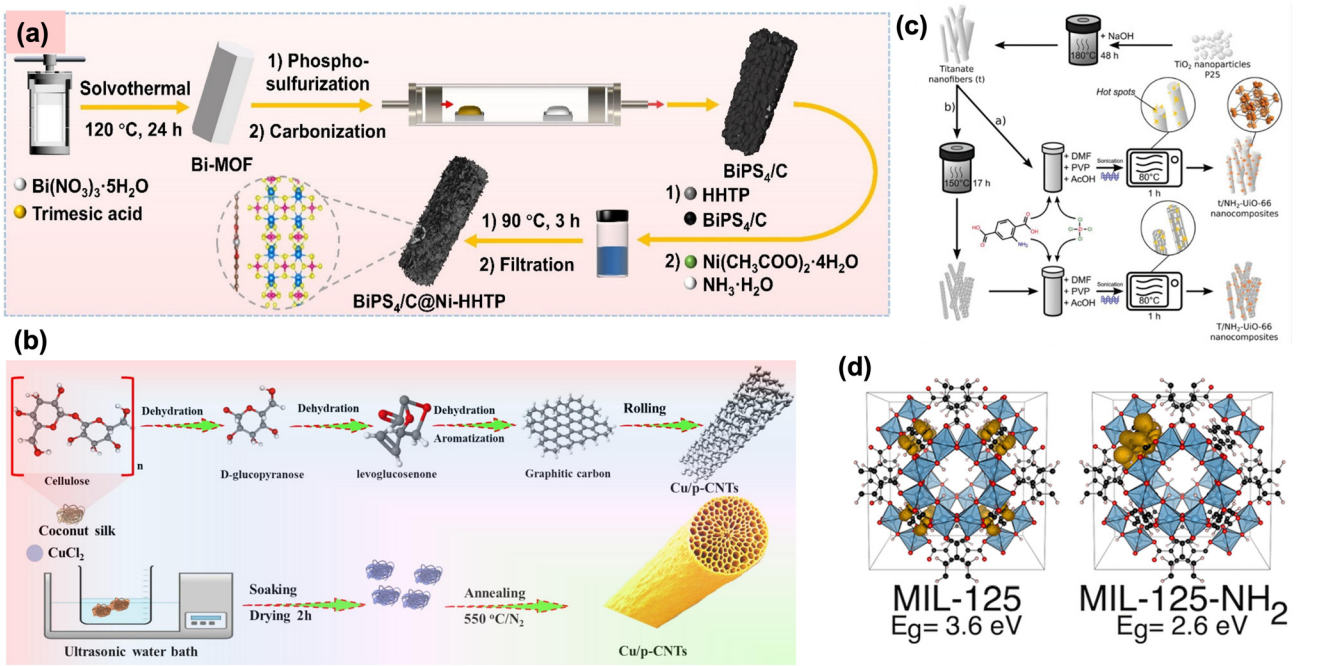

Fig. 7 (a) Schematic of the synthesis of porous core–shell $BiPS_4$/C@Ni-HHTP, where Ni-HHTP conductive MOF nanostructures grow *in situ* on Bi-MOF-derived $BiPS_4$/C, forming a synergistic architecture that combines high conductivity, abundant porosity, and a large accessible surface area. Reproduced with permission from ref. 128 Copyright 2025 Elsevier. (b) Illustration of the formation process of Cu/p-CNTs, in which strong metal–carbon interactions, controlled electron-deficiency of metal sites, and preserved multimodal porosity (micro-, meso-, and macropores) enable a balanced combination of conductivity, ion transport, and capacitive performance. Reproduced with permission from ref. 129 Copyright 2025 Elsevier. (c) Synthetic route for TiO_2/NH_2-UiO-66 nanocomposites, prepared by first converting TiO_2 (P25) into titanate nanofibers *via* hydrothermal treatment, followed by *in situ* growth of MOF particles on the 1D fibers to enhance interfacial charge transfer. Reproduced with permission from ref. 130 Copyright 2019 John Wiley and Sons. (d) Sublattice structure of MIL-125 (TiO_2/1,4-benzenedicarboxylate) and its aminated derivatives, demonstrating how linker functionalization can systematically tune the optical properties and reduce the bandgap, highlighting the combined power of synthetic and computational design in optimizing hybrid MOF materials. Reproduced with permission from ref. 131 Copyright 2013 American Chemical Society.

like channels, supporting high permeability and fast charge transfer for sensing and energy applications.[161] MOF/TiO_2 heterojunctions further highlight the importance of interface engineering; band bending drives electrons from TiO_2 into the MOF and holes in the reverse direction, markedly improving CO_2 photoreduction (Fig. 7c).[130] At the manufacturing scale, microwave-assisted continuous synthesis of HKUST-1 in ethanol demonstrates how such hybrid systems can be produced with exceptional space–time yields.[162]

3.5 Post-synthetic functionalization and redox/ionic co-transport

Post-synthetic modification (PSM) has become a powerful route for tuning the electronic landscape of conductive MOFs without disturbing their long-range order. Unlike de-novo synthesis, which fixes composition at crystallisation, PSM allows targeted adjustment of π-orbital overlap, band alignment, and carrier concentration through covalent linker editing, metal-node exchange, or guest doping.

Covalent modification of linkers provides molecular-level control over band structure. In $Ni_3(HITAT)_2$, Dincă's sulfonation of the indole N–H sites introduced electron-withdrawing methane sulfonyl groups, reducing π-electron density in the truxene core. The resulting $Ni_3(HITAT\text{-}SO_2CH_3)_2$ showed a 20-fold drop in electrical conductivity compared to the pristine 44 mS cm^{-1}, demonstrating how small changes at the linker periphery can strongly regulate carrier mobility.[110] In contrast, electron-donating groups such as $-NH_2$ or –OH elevate the Fermi level and strengthen delocalization-seen in aminated MIL-125(Ti), where $-NH_2$ substitution narrows the bandgap from 3.6 eV to 2.6 eV and improves photoconductivity by an order of magnitude (Fig. 7d).[131]

Metal-center exchange offers another precise lever by inserting redox-active or mixed-valence ions into an electronically passive framework. Long's Fe^{2+} exchange in $Mn_2(DOBDC)$ transformed the insulating parent ($\sim 10^{-12}$ S cm^{-1}) into $Fe_2(DOBDC)$ with 5.8×10^{-8} S cm^{-1} conductivity-over four orders of magnitude higher-due to new Fe d-states near the Fermi level that promote intervalence charge transfer.[75] Similar redox tuning was achieved in Cu-HKUST-1, where partial replacement of Cu^{2+} with Co^{2+} or Ni^{2+} subtly altered the Cu–O–C geometry and produced a threefold conductivity enhancement while preserving crystallinity.[163] A third route, guest infiltration or post-synthetic doping, modulates the electronic structure by introducing redox-active species directly into the pores. Talin's infiltration of TCNQ into HKUST-1 formed a charge-transfer complex that boosted conductivity from 10^{-8} to 7×10^{-2} S cm^{-1} (a six-order-of-magnitude increase). UPS revealed new mid-gap states from π–π stacking between TCNQ and the Cu-carboxylate nodes.[163] Likewise, iodine exposure of $Cu[Ni(PDT)_2]$ oxidised the Ni centres, converting it into a p-type semiconductor with fourfold higher conductivity ($10^{-8} \rightarrow 10^{-4}$ S cm^{-1}). Notably, such doping is reversible, showing that MOFs can behave as tunable "redox sponges".[148] Taken together, these synthetic and post-synthetic strategies establish the foundational "knobs" that determine how a MOF ultimately conducts charge. Choices made during linker design, metal selection, defect creation, or guest incorporation do not merely modify chemical composition-they sculpt the underlying electronic landscape by altering orbital overlap, redox accessibility, pore connectivity, and lattice dynamics. As a result, the transport behaviour of a conductive MOF emerges directly from these structural decisions: whether electrons move through delocalized π–d bands, hop between mixed-valence centres, migrate along π-stacked columns, or couple with ionic carriers depends on how its building blocks are arranged at the atomic and mesoscopic scales. Having established how synthetic routes create these structural motifs, the next section examines how specific structural features; coordination geometry, defects, porosity, heterometallic interfaces, and hybrid networks, govern the resulting electrochemical properties. Understanding this structure–property relationship is essential for translating chemical design into predictable, high-performance energy-storage behaviour.

Critical insight: although diverse synthetic and post-synthetic strategies enable precise tuning of conductivity, many high-performing c-MOFs rely on complex or solvent-intensive routes. Bridging the gap between laboratory-scale optimization and scalable synthesis remains a key challenge. Developing chemistry-conserving and defect-tolerant strategies will be essential for translating c-MOFs into practical energy-storage platforms.

4. Structure–property relationships

Rather than benchmarking absolute performance values, the studies discussed in this section are selected to elucidate generalizable structure–property relationships, including both performance gains and inherent trade-offs. The electrochemical behavior of c-MOFs and their derivatives is intimately governed by the interplay between crystal chemistry, defect topology, pore architecture, and electronic connectivity.[164] Understanding how atomic- and mesoscale features dictate conductivity, ion transport, and redox dynamics is central to designing next-generation energy-storage materials.[165] Recent studies demonstrate that small structural variations, whether in coordination environment, defect density, ligand conjugation, or morphology, can dramatically alter charge mobility and electrochemical kinetics, transforming otherwise insulating coordination solids into efficient charge-storage frameworks.[166] To enable meaningful cross-comparison across chemically distinct c-MOF families, we consistently connect framework descriptors (electrical conductivity, ion-transport indicators such as transference/MSD trends, and interfacial charge-transfer metrics) to device outputs including capacity/capacitance, rate performance, and cycling retention. While absolute values depend on electrode architecture and testing protocols, recurring quantitative correlations emerge across 2D π–d frameworks, defect/OMS-rich Zr-MOFs, heterometallic systems, and MOF-based hybrids.[167]

Furthermore, to visually consolidate the structure–property distinctions between intrinsic conductive MOFs and MOF-

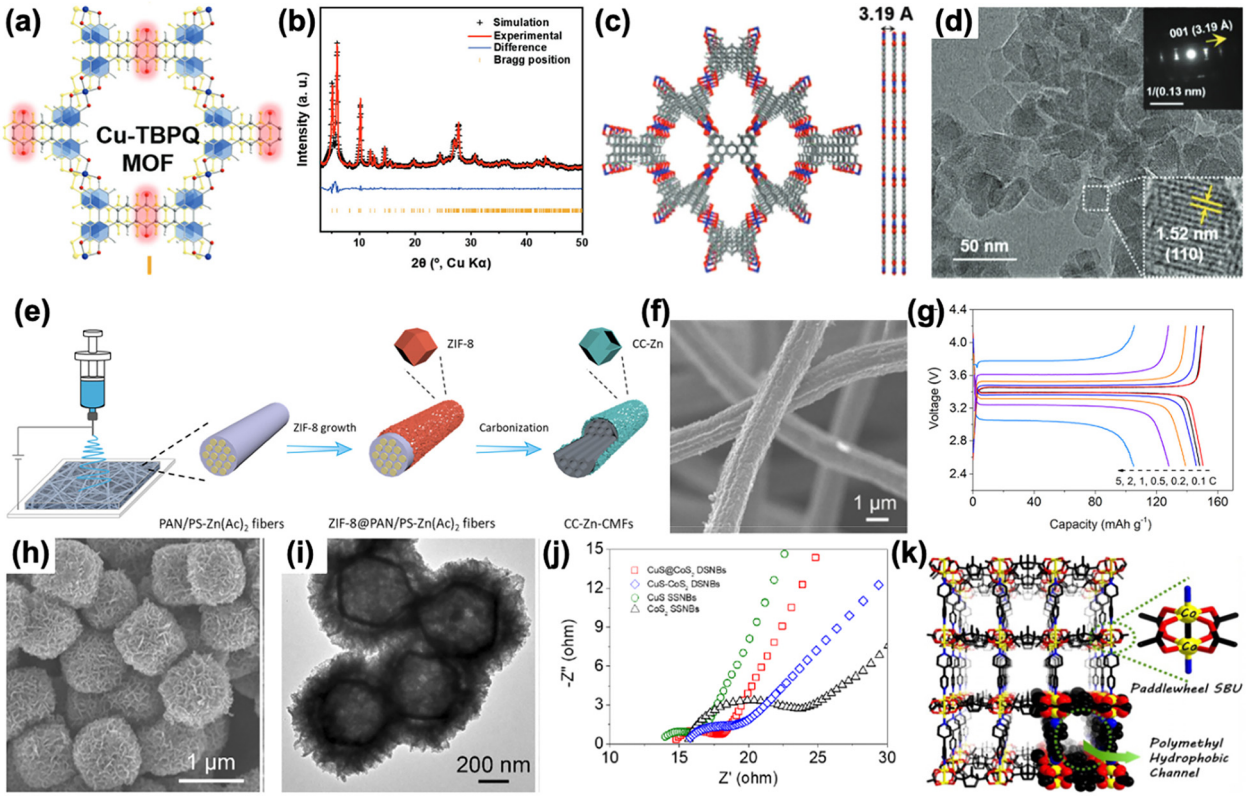

Fig. 8 (a) Schematic structure of the Cu-TBPQ MOF, where grey, red, white, and blue spheres represent C, O, H, and Cu atoms, respectively. (b) Experimental and refined PXRD patterns of the Cu-TBPQ MOF collected using Cu Kα radiation (λ = 1.5418 Å). (c) Structural model of the Cu-TBA framework, illustrating its ordered coordination topology. (d) TEM images of Cu-TBPQ MOF with magnified views from the highlighted region and corresponding out-of-plane diffraction pattern. (e) Schematic illustration of the synthetic route for CC-Zn-CMFs. (f) FESEM image of CC-Zn-CMFs showing the fibrous morphology. (g) Galvanostatic charge–discharge voltage profiles of the CC-Zn-CMFs–Li//LFP full cell measured at different current rates. (h) FESEM image and (i) TEM images of CuS–CoS_2 double-shell nanoboxes (DSNBs). (j) Comparative Nyquist plots of different MOF-based electrodes. (k) Three-dimensional structural representation of the Co-bpy framework.

derived materials, Fig. 8 summarizes representative structural, morphological, and electrochemical characterization. Fig. 8(a) presents the idealized coordination structure of a Cu-TBPQ conductive MOF, highlighting extended π-conjugation and metal–ligand orbital overlap that enable intrinsic electronic transport within the crystalline framework. The experimental validity of this ordered structure is confirmed by refined PXRD data in Fig. 8(b), where the close agreement between simulated and experimental patterns demonstrates long-range crystallinity.[168] The corresponding structural model in Fig. 8(c) and lattice-resolved TEM image in Fig. 8(d) further verify the preservation of periodic framework order at the nanoscale, establishing conductive MOFs as electronically active crystalline solids rather than insulating porous hosts.[169]

In contrast, Fig. 8(e) illustrates a representative post-synthetic transformation route, where a MOF precursor is converted into a derived conductive architecture through controlled growth and carbonization. The resulting fibrous morphology observed in Fig. 8(f) confirms that MOF-derived materials retain structural templating but no longer rely on framework-based electronic delocalization. This distinction is reflected electrochemically in Fig. 8(g), where the galvanostatic charge–discharge profiles indicate enhanced rate capability arising from improved electronic percolation and interfacial ion transport rather than intrinsic band-type conduction.[170] Additional morphological reconstruction is evident in Fig. 8(h) and (i), where SEM and TEM images reveal hierarchical and hollow nanostructures formed after framework decomposition, highlighting the transition from ordered coordination networks to heterogeneous conductive matrices. The impedance comparison in Fig. 8(j) further demonstrates reduced charge-transfer resistance in MOF-derived systems, consistent with interface-dominated transport mechanisms.[171] Finally, Fig. 8(k) schematically contrasts the two material classes, illustrating how conductive MOFs support directional charge transport through ordered metal–ligand pathways, whereas MOF-derived materials rely on reconstructed heterointerfaces and conductive scaffolds.[172]

Together, these results establish a clear mechanistic distinction: conductive MOFs operate as crystalline electronic materials with intrinsic charge delocalization, while MOF-derived materials function as structurally templated composites in which conductivity emerges from post-synthetic reconstruction and interfacial effects.

4.1 Coordination environment and ligand design

The fundamental origin of electronic and ionic transport in c-MOFs lies in their coordination chemistry. Planar geometries that enforce π–d overlap, such as those in $Ni_3(HITP)_2$ or $Cu_3(HHTP)_2$, establish continuous delocalization pathways, while new ligand systems are being designed to extend conjugation and create multiple redox centers.[175]

For instance, the introduction of a hexahydroxy salicylamide (6OH-HBB) ligand in a 2D Cu-HBB-MOF led to strong N_2O_2 coordination pockets (Fig. 9a) and planarization, yielding enhanced charge delocalization and K^+ diffusion channels. The resulting cathode delivered 228 mAh g^{-1} with exceptional cycling life, showing that multisite coordination and ligand planarization directly translate to redox utilization and electronic stability due to the Cu-HBB-MOF possessing a high density of redox-active sites, with each repeating unit capable of storing up to 12 K^+ (Fig. 9b).[72] Similarly, in Ni-MOFs grown *in situ* on graphene oxide, the d–π orbital hybridization between Ni centers and the GO matrix improved charge delocalization and prevented structural collapse, achieving over 700 mAh g^{-1} capacity as a LIB anode.[176] These studies reveal that the chemical identity and conjugation of linkers, along with hybrid interfacial bonds, modulate both the electronic structure and the exposure of redox-active sites. Across these coordination-driven designs, the effect is reflected in clear performance outputs, spanning 228 mAh g^{-1} for a multisite Cu-HBB-MOF potassium cathode to >700 mAh g^{-1} for Ni-MOF/GO lithium anodes, reinforcing ligand conjugation/orbital alignment as a transferable quantitative lever.

4.2 Defect chemistry and open metal sites

Defect engineering provides another powerful handle for tuning framework properties. Rationally created ligand and metal-site vacancies increase open metal site (OMS) density, alter local coordination, and modulate Lewis acidity. In Hf-based MOF quasi-solid electrolytes, defect engineering increases the exposure of open metal sites (OMS), strengthening Lewis acid–base interactions with LiTFSI. Charge-difference density maps show electron accumulation on $TFSI^-$ oxygen atoms and depletion around OMS, forming polarized pathways that promote Li^+ migration. DFT analysis further confirms that while LiTFSI binds weakly on perfect UiO-66(Hf), defect sites elongate Li–O and Li–N bonds (from ~1.90/1.95 Å to 2.16/2.11 Å), and anion immobilization enables high ionic conductivity (1.0 mS cm^{-1}) and long-term Li‖NCM811 cycling stability (Fig. 9c).[173] Similarly, dual-defect engineering in bimetallic Ni–Co MOF-74 introduced both ligand vacancies and cation disorder, arising from the partial substitution of 2,5-dihydroxyterephthalic acid (H_4dobdc) with the lower-coordination salicylic acid (SA) ligand and the weaker coordination affinity between SA and Co^{2+}. This

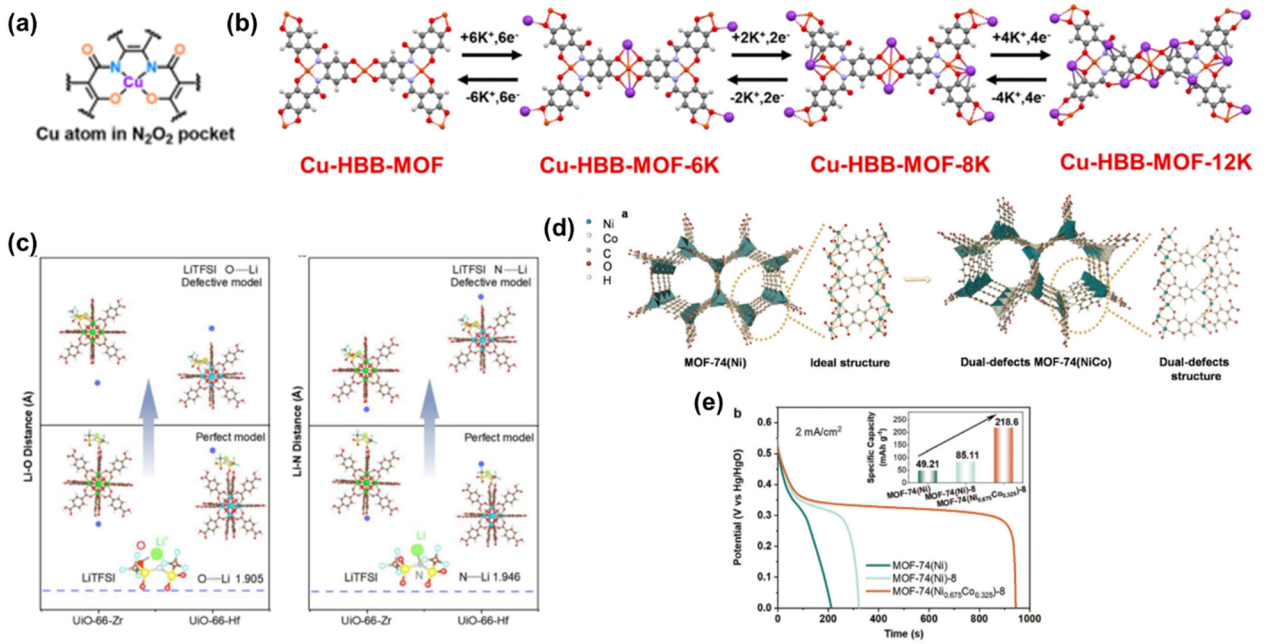

Fig. 9 (a) Schematic illustration of the construction strategy for the Cu-HBB-MOF electrode, showing multiple accessible active sites engineered within the framework. (b) Structural evolution of the Cu-HBB-MOF during the potassium-ion insertion and extraction processes. Reproduced with permission from ref. 72 Copyright 2016 Royal Society of Chemistry. (c) Comparison of Li–O and Li–N bond distances for LiTFSI coordinated within different MOF environments. Reproduced with permission from ref. 173 Copyright 2025 American Chemical Society. (d) Structure of the defect-engineered MOF: illustrative pathway showing the transformation from pristine MOF-74(Ni) to dual-defect MOF-74(NiCo), generated through solvothermal synthesis using salicylic acid (SA) as a modulator and Co^{2+} incorporation to create both ligand and metal-node defects. (e) Electrochemical performance of MOF electrodes in 3 M KOH: galvanostatic charge–discharge (GCD) curves of MOF-74(Ni), defect-rich MOF-74(Ni)-8, and bimetallic defect-engineered MOF-74($Ni_{0.675}Co_{0.325}$)-8 at 2 mA cm^{-2}, with the inset showing their corresponding calculated specific capacities. Reproduced with permission from ref. 174 Copyright 2024 John Wiley and Sons.

combination generated abundant oxygen vacancies and disrupted the local coordination environment, which in turn facilitated the *in situ* transformation of the framework into highly active oxyhydroxides during cycling (Fig. 9d). As a direct consequence of these structural defects and enhanced reconfigurability, the Ni–Co MOF-74 exhibited nearly four times the capacity of pristine MOF-74 (Fig. 9e).[174] These examples highlight how defect concentration must be precisely balanced; sufficient to introduce active sites and enhance orbital coupling, but not so excessive as to destabilize the lattice or obstruct ion channels. Quantitatively, defect/OMS enrichment repeatedly couples stronger anion regulation with improved transport and kinetics, as seen in $\sigma \approx 1.0$ mS cm^{-1} and stable Li||NCM811 cycling for defect-engineered UiO-type electrolytes, alongside ~4× capacity enhancement for dual-defect Ni–Co MOF-74 relative to pristine MOF-74.

4.3 Pore architecture, dimensionality, and ion transport

Pore geometry exerts a decisive influence on ionic conductivity and electrolyte infiltration. Systematic studies on nanocrystalline MOFs show that pore aperture strongly governs ion transport: larger channels accommodate more Li salt, while open metal sites help immobilize anions and increase the Li^+ transference number. As illustrated in the structural schematics in Fig. 10a, wider pores favor vehicle-type transport of solvated ions, whereas narrower channels or OMS-rich environments promote partial desolvation and stronger anion binding. Molecular dynamics simulations further support this trend, showing that solvated ions move rapidly through wide channels, while desolvated ions hop through confined pathways. This behavior is reflected in the MSD profiles in Fig. 10b, where each MOF exhibits a distinct Li^+/$TFSI^-$ diffusion pattern. Zn-MOF-74, with abundant OMS, strongly anchors $TFSI^-$ and allows Li^+ to diffuse more freely, producing clear ion-sieving behavior. HKUST-1, with fewer and weaker OMS sites, shows nearly overlapping MSD curves, indicating limited anion regulation. In contrast, MOF-5-lacking OMS altogether permits rapid $TFSI^-$ motion, resulting in poor anion immobilization and reduced selectivity.[177] This OMS/pore-governed ion selectivity provides a quantitative bridge between simulations and experiments, where suppressed anion mobility (Zn-MOF-74) aligns with more effective cation transport and improved reversibility compared with OMS-deficient analogues (MOF-5). A similar structure–transport relationship is observed in Li–O_2 systems, where MOFs with uniformly distributed micropores and accessible open metal sites (*e.g.*, Mn-MOF-74) enrich O_2 concentrations by up to eighteen fold and provide selective adsorption pathways that dramatically improve discharge capacities (≈9420 mAh g^{-1}), far exceeding those of carbon-only electrodes. In energy-storage electrodes, dimensionality dictates anisotropy of conduction: 2D c-MOFs exhibit strong in-plane delocalization, whereas 3D frameworks rely on hopping and super-exchange across orthogonal directions.[179] The flake-like microstructure of $Cu_3(HHTP)_2$ (Fig. 10c inset) offers a clear transport advantage, the thin lateral geometry shortens ion-diffusion pathways and enables markedly better rate performance than rod-like or agglomerated counterparts. In A-CuHHTP, these 'flake-like' particles contain pores

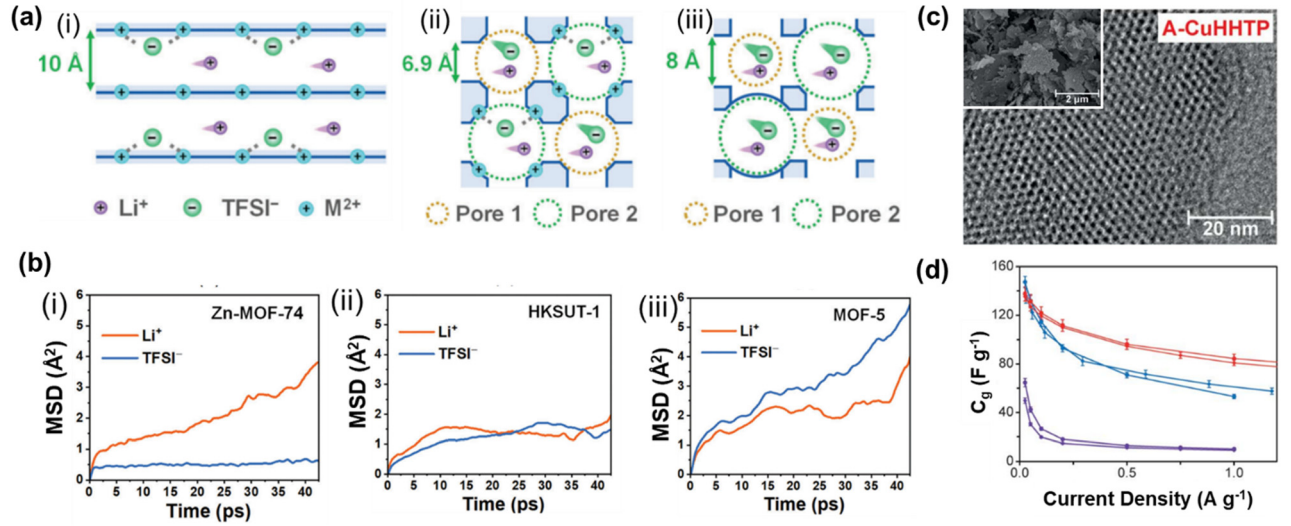

Fig. 10 (a) Schematic illustration of ion-transport behavior within the pore environments of three MOFs: (i) M-MOF-74, (ii) HKUST-1, and (iii) MOF-5. The M^{2+} cyan spheres in panels (i and ii) represent the open metal sites present in M-MOF-74 and HKUST-1 frameworks. (b) Mean square displacement (MSD) plots for Li@Zn-MOF-74, Li@HKUST-1, and Li@MOF-5, demonstrating that $TFSI^-$ anions are strongly immobilized within Zn-MOF-74, partially restricted in HKUST-1, but remain mobile in MOF-5. Reproduced with permission from ref. 177 Copyright 2023 John Wiley and Sons. (c) TEM image of A-CuHHTP nanosheets. (d) Electrochemical characterization of symmetric supercapacitors assembled with A-CuHHTP, B-CuHHTP, and C-CuHHTP composite electrodes using NEt_4BF_4/ACN electrolyte. Specific capacitance values (C_g) *versus* current density are shown up to 1 V, with results reported for two independent cells per material. C_g values were calculated based solely on the mass of active $Cu_3(HHTP)_2$ in the electrodes. Reproduced with permission from ref. 178 Copyright 2022 Royal Society of Chemistry.

oriented perpendicular to the flat face of each flake (Fig. 10c), creating a dense array of short, straight channels. As a result, ions can access the pore network quickly and move through the particles with minimal tortuosity, which directly contributes to their superior kinetics diffuse more freely, producing clear ion-sieving behavior (Fig. 10d).[178] The microporous channels of MOF-5 embedded within the composite separator further illustrate how angstrom-scale pore architectures can act as selective ion-gating pathways, enabling fast Li^+ transport while sterically excluding larger redox-active species such as $Fc_1N_{11}^{2+}$, thereby achieving a $Li^+/Fc_1N_{11}^{2+}$ selectivity ratio of 26.6 and directly enhancing coulombic efficiency in non-aqueous redox flow systems.[183] Such results underscore that pore size, dimensionality, and particle morphology jointly govern the balance between electronic conduction and ionic accessibility.

4.4 Composition modulation and heterometallic synergy

Mixed-metal and heteroatom substitution strategies offer further control over electronic configuration and catalytic activity. The introduction of Co into the Zn-MOF lattice generates defect-rich, disordered bimetallic centers (Fig. 11a), which locally modulate the electronic density and create stronger Lewis-acidic sites. These defect sites markedly enhance LiPS adsorption, as evidenced by the suppressed UV-Vis. peak in Fig. 11b, and accelerate bidirectional redox conversion at the cathode.

Benefiting from this defect-engineered electronic environment, the $Co_{0.75}Zn_{0.25}$-MOF/rGO composite delivers high sulfur utilization with a Li^+ diffusion coefficient of 7.9×10^{-11} $cm^2\ s^{-1}$ and excellent catalytic reversibility.[85]

Similarly, Ti–Co bimetallic MOFs used as interfacial membranes in Li–metal batteries activate dormant Li and accelerate charge-transfer kinetics through spontaneous redox interactions, delivering over 1000 hours of stable cycling. This behavior aligns with their intrinsic electronic structure: the electrostatic potential (ESP) map reveals pronounced charge polarization around Co sites (Fig. 11c), indicating electron redistribution that strengthens charge transfer and redox activity-key factors for efficient energy storage. Consistent with this, Fig. 11d shows significant increases in C–C, C–O, C–O–C, and C═C/O peak intensities during Li^+ desorption, followed by their decline upon intercalation, confirming that incorporating MOF(Co–Ti) reshapes the local coordination environment to enhance reversible redox-driven Li storage and improve ion regulation.[180]

Extending this concept, NiS_2/CuS@C hybrid spheres derived from MOF precursors (Fig. 11e) illustrate how heterostructure

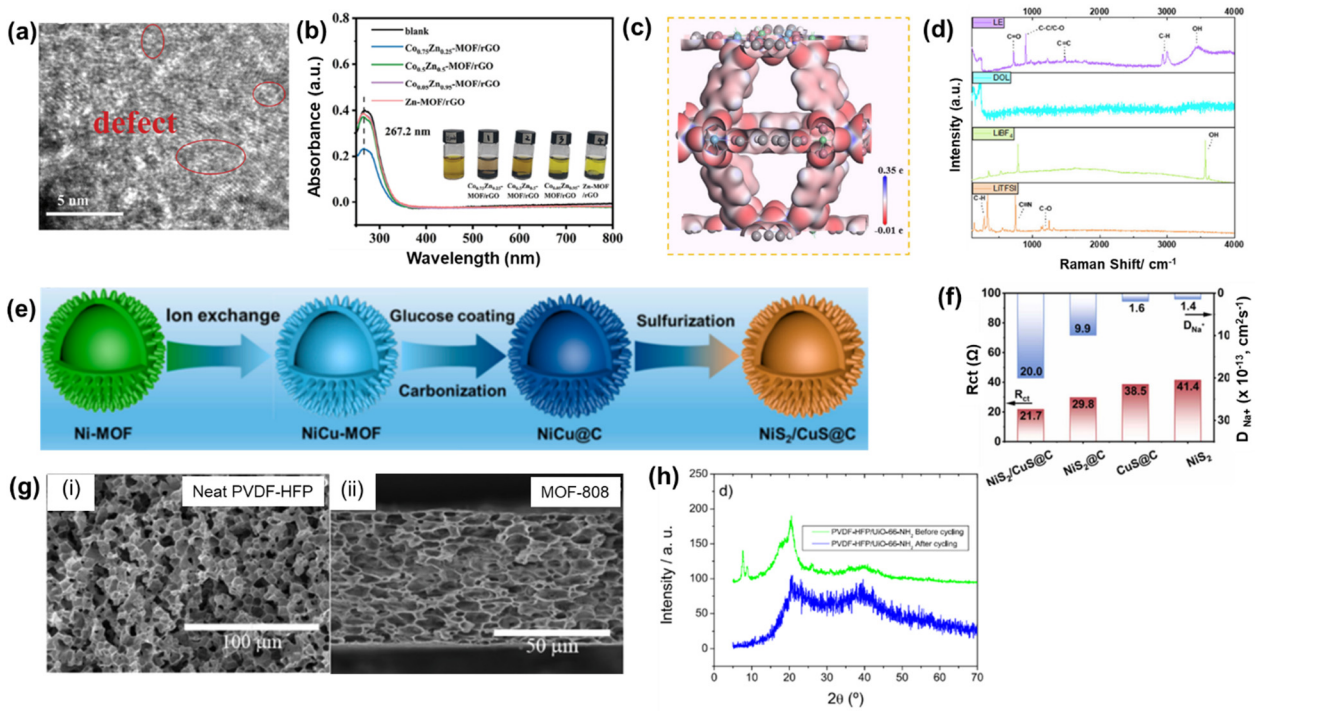

Fig. 11 (a) SEM images of the Co_xZn_{1-x}-MOF/rGO composites showing morphology evolution with varying Co/Zn ratios. (b) Photographs of $Co_{0.75}Zn_{0.25}$-MOF/rGO, $Co_{0.5}Zn_{0.5}$-MOF/rGO, $Co_{0.05}Zn_{0.95}$-MOF/rGO, and Zn-MOF/rGO after 12 h static adsorption in Li_2S_6 solution, along with the corresponding UV-vis spectra of the supernatant (inset), demonstrating their polysulfide-trapping capability. Reproduced with permission from ref. 85 Copyright 2024 John Wiley and Sons. (c) Electrostatic potential (ESP) mapping of MOFs (Co-Ti series) illustrating sulfur-species adsorption behavior. (d) *In situ* FT-IR and Raman spectra revealing Li^+ transport kinetics in G@MOF(Co-Ti). Reproduced with permission from ref. 180 Copyright 2025 Royal Society of Chemistry. (e) Schematic illustration of the synthesis procedure for the NiS_2/CuS@C heterostructure. (f) Calculated charge-transfer resistance (R_{ct}) and Na^+ diffusion coefficients (D_{Na^+}) for NiS_2/CuS@C, NiS_2@C, CuS@C, and NiS_2, highlighting the kinetic advantages of the heterostructure. Reproduced with permission from ref. 181 Copyright 2025 Elsevier. (g) Cross-sectional images of (i) pristine PVDF-HFP membrane and (ii) PVDF-HFP/MOF-808 composite membrane. (h) XRD patterns of the PVDF-HFP/UiO-66-NH_2 composite membrane before and after cycling, indicating structural stability during operation. Reproduced with permission from ref. 182 Copyright 2022 Elsevier.

engineering can further optimize charge transport and mechanical resilience. The strong interfacial coupling between NiS_2 and CuS creates built-in electric fields that enhance Na^+ diffusion and electronic conductivity, while dual carbon confinement maintains structural integrity under long-term cycling. NiS_2/CuS@C delivers the lowest charge-transfer resistance and the highest Na^+ diffusion coefficient (Fig. 11f) among all samples because its NiS_2–CuS heterojunction and carbon shell synergistically enhance interfacial conductivity, stabilize the built-in electric field, and accelerate ion transport.[181] A similar heterometallic effect is observed in NiCo-MOF-modified graphite felt electrodes, where the mixed Ni/Co nodes provide complementary redox centers and unsaturated coordination sites that enhance $2Br^-/Br_2$ reaction kinetics, boosting coulombic and energy efficiencies in Zn–Br redox flow batteries while preserving structural stability during long-term cycling.[184] These findings confirm that heterometallic coupling introduces synergistic orbital overlap and charge redistribution, improving both conductivity and redox kinetics. These heterometallic effects are repeatedly expressed in measurable kinetic descriptors, including enhanced Li^+ diffusion (*e.g.*, 7.9×10^{-11} cm^2 s^{-1} for $Co_{0.75}Zn_{0.25}$-MOF/rGO) and prolonged cell stability (*e.g.*, >1000 h in Li–metal configurations), indicating charge redistribution around mixed-metal nodes as a broadly applicable design rule.

4.5 Hybridization and interfacial engineering

Hybrid frameworks that integrate MOFs with conductive substrates or polymers demonstrate remarkable performance gains due to improved electron percolation and mechanical stability. A similar strategy has been applied to Zn–Ce redox flow batteries, where carbon felt electrodes modified with ZIF-8 and ZIF-67 derivatives introduce abundant N/O-rich active sites and porous interfaces that guide uniform Zn nucleation, suppress dendrite formation, and enhance energy efficiency to ~80–86% at 20 mA cm^{-2}.[185] Similarly, depositing high-surface-area MOFs such as MIL-125-NH_2 and UiO-66-CH_3 onto graphite felt electrodes in zinc–polyiodide redox flow batteries has been shown to accelerate the I^-/I_3^- redox couple and raise energy efficiency by ~6.4% and ~2.7%, respectively, owing to improved interfacial charge-transfer kinetics and enhanced electrochemical accessibility.[66] Embedding MOFs into PVDF-HFP separators refines polymer crystallinity and pore architecture, yielding a more uniform, low-resistivity network that suppresses capacity fading. SEM evidence (Fig. 11g), shows that MOF nanoparticles decorate the pore walls to form a two-phase composite in direct contact with the electrolyte, enhancing Li-ion transport. Although IR analysis indicates partial MOF collapse during cycling (Fig. 11h), the resulting amorphous metal–oxide residues remain active and reinforce the separator much like ceramic fillers, stabilizing interfacial transport and improving overall battery performance.[182] Likewise, MOF/graphene[108] and MOF/MXene hybrids[186] combine intrinsic porosity with conductive networks, enabling efficient electron pathways while preserving electrolyte accessibility key for long-life flexible electrodes. A complementary approach is the integration of active nanostructures with flexible conductive substrates, exemplified by ZnO@ZnO-QDs/C core–shell nanorod arrays grown directly on carbon cloth, where the vertically aligned ZnO backbone provides rapid electron pathways while a thin carbon shell buffers volume change and eliminates binder-related interfacial resistance, enabling high reversible capacities (≈1055–530 mAh g^{-1} from 100 to 1000 mA g^{-1}) and excellent cycling stability (≈11% loss after 100 cycles).[187] Further emphasizing the power of interfacial engineering, 3DG/MOF-derived Fe_2O_3 aerogels-where porous Fe_2O_3 nanoframeworks are spatially confined within a three-dimensional graphene network-offer highly interconnected conductive pathways, abundant stress-buffering voids, and intimate MOF-graphene contact, yielding exceptional performance (≈1129 mAh g^{-1} at 0.2 A g^{-1} and 98% retention over 1200 cycles at 5 A g^{-1}).[188]

A MOF–polymer hybrid (MOF808-D@PS) was developed to overcome the sluggish Li^+ transport in dense sulfur-based polymer electrodes. Introducing nitrogen-rich ligands into MOF808 (Fig. 12a) creates polar coordination sites that boost Li^+ diffusion by nearly three orders of magnitude compared to pristine sulfur polymers. As shown in Fig. 12b, the hybrid delivers the highest capacitance contribution across 0.1–0.4 mV s^{-1}, reflecting much faster electrochemical kinetics. The nitrogen-enriched, defect-engineered framework offers abundant Li^+ pathways and rapid redox dynamics, enabling MOF808-D@PS to function as an efficient sulfur-polymer electrode. Overall, this design shows how MOF–polymer hybridization can ease diffusion limitations while preserving the high-energy characteristics of sulfur hosts.[189]

In redox-flow systems, similar interfacial engineering benefits are observed when 2D Ni-MOF nanosheets are assembled onto porous polymer separators, where the angstrom-scale interlayer galleries selectively impede active-species crossover while maintaining fast supporting-electrolyte transport, enabling markedly improved coulombic and energy efficiencies (91.0% and 85.1%) and higher discharge capacity (1.30 Ah L^{-1}) compared with pristine Celgard.[190] Across these hybrid strategies, improvements recur in comparable device metrics-higher EE/CE in flow systems, reduced interfacial resistance and capacity fade in separators, and enhanced long-term retention in MOF-derived hybrid electrodes-highlighting interface engineering as the most scalable route to reproducible gains.

Taken together, Sections 4.1–4.5 show that c-MOF structure–property relationships can be rationalized using a compact set of quantitative descriptors: σ captures electronic percolation efficiency, OMS/defect density governs anion binding and effective cation transport, and pore architecture/morphology controls diffusion length and electrolyte accessibility. These descriptors consistently map onto capacity/capacitance, rate performance, and cycling stability across distinct c-MOF families and device formats, motivating the derived-framework strategies discussed next. See Table 3 for various physical properties.

4.6 MOF-derived carbon frameworks

Transforming MOFs into carbon materials through thermal treatment yields hierarchical architectures that preserve the

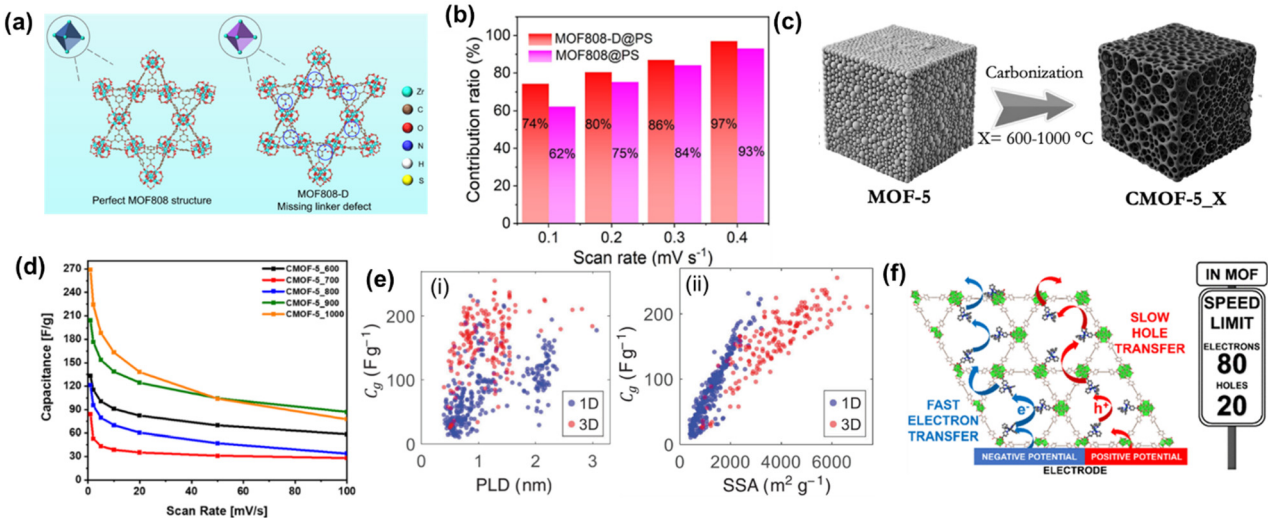

Fig. 12 (a) Schematic illustrations of the MOF808@PS and defect-engineered MOF808-D@PS composites. (b) Pseudocapacitive contribution ratios of MOF808-D@PS and MOF808@PS at various scan rates. Reproduced with permission from ref. 189 Copyright 2025 American Chemical Society. (c) Carbonization pathway employed to obtain the CMOF-5-*X* series of carbon-derived MOF samples. (d) Gravimetric capacitance values of the CMOF-5-*X* electrodes measured at different scan rates. Reproduced with permission from ref. 193 Copyright 2025 Royal Society of Chemistry. (e) Correlation of gravimetric capacitance with (i) pore-limiting diameter (PLD) and (ii) SSA, highlighting structure–property relationships. Reproduced with permission from ref. 194 Copyright 2025 John Wiley and Sons. (f) Conceptual illustration of asymmetric charge-carrier transport in a conductive MOF, showing fast electron transfer under negative potentials and substantially slower hole transport under positive potentials due to the intrinsic electronic structure of the framework. Reproduced with permission from ref. 195 Copyright 2024 American Chemical Society.

parent framework's porosity while introducing graphitic conductivity. A similar approach was demonstrated using MOF-76 (Gd), where carbonization produced a conductive, microporous host capable of encapsulating sulfur and effectively confining polysulfides, yielding 658 mAh g^{-1} initial capacity with ~93% retention after 200 cycles at 0.5 C owing to improved conductivity, flexible pore buffering, and enhanced shuttle suppression.[191] Controlled carbonization temperature has been shown to dictate graphitization degree, pore volume, and conductivity. Kukułka *et al.* reported the solvothermal synthesis of pristine MOF-5 through a modified procedure of Park *et al.*,[192] followed by carbonization under an inert atmosphere at 600–1000 °C to obtain CMOF-5. This temperature-dependent carbonization route provides tunable porous carbons derived from MOF-5 (Fig. 12c) carbonized MOF-5 at 1000 °C achieved 50 S m^{-1} conductivity and delivered simultaneous high energy (166.9 Wh kg^{-1}) and power density (9234 W kg^{-1}) in Zn-ion systems (Fig. 12d).[193] Similarly, honeycomb-like hierarchical carbons derived from ZIF-8 composites exhibited dual micro/mesoporosity, balancing ion diffusion and charge storage to achieve 361 F g^{-1} capacitance and excellent flexibility in solid-state supercapacitors.[196] These results collectively demonstrate that template-guided porosity and carbon ordering inherited from MOFs translate directly into superior charge storage and mechanical robustness. ZIF-67-derived yolk–shell CoSe/C dodecahedra further highlight the versatility of MOF-templated carbon frameworks, where *in situ*-formed CoSe nanoparticles (~15 nm) confined within nitrogen-doped, graphitized mesoporous carbon enable high Na^+ storage (≈597 mAh g^{-1} at 0.2 A g^{-1}) and excellent high-rate performance (≈362 mAh g^{-1} at 16 A g^{-1}) due to improved electronic conductivity, electrolyte penetration, and buffered volume changes.[197] Hollow MOF-derived metal oxides offer similar advantages; for example, $NiFe_2O_4$ nanocages obtained from NMOF precursors retain a hierarchical voided architecture that shortens Li^+ diffusion paths, buffers volume change through stepwise Ni–Fe redox transitions, and delivers exceptional capacities (≈652 mAh g^{-1} at 10C and ≈1017 mAh g^{-1} after 200 cycles at 1C) owing to their mechanically resilient, porous shells.[198] MOF-derived ZnO electrodes prepared from Zn-MOF precursors similarly benefit from the inherited high surface area and tailored morphology, with carbon-consolidated ZnO delivering improved Zn/Zn^{2+} reversibility and high voltage efficiency (≈92% at 5 mA cm^{-2}) in an all-zinc redox flow battery setup.[199] A MOF-derived V_2O_3@C hollow microcuboid produced from MIL-47 further exemplifies this principle, where V_2O_3 nanoparticles provide strong chemical anchoring for polysulfides and the 3D carbon framework delivers high conductivity and mesoporous buffering, enabling excellent cycling stability (62.3% after 1000 cycles at 1 C) and high-rate performance even at elevated sulfur loading (3.7–7.9 mg cm^{-2}).[200]

4.7 Data-driven and mechanistic insights

Beyond experimental tuning, data-centric approaches are beginning to clarify the complex interdependence between structure and function. Machine-learning analyses of hundreds of MOF electrodes revealed that specific surface area (SSA) and porosity overwhelmingly dictate capacitance and charging rate, whereas pore-limiting diameter plays only a secondary role, as visualized in Fig. 12e.[194] These findings align

with molecular-level understanding-ion coordination and diffusion pathways depend more on accessible surface and pore connectivity than on nominal size metrics. Likewise, redox-hopping studies using Ru-functionalized MOFs established that charge-carrier type and spacing between redox centers, rather than intrinsic redox potential, determine hopping rates emphasizing the need to control spatial arrangement at the molecular level (Fig. 12f).[195]

***Critical insight*:** Structure–property relationships in c-MOFs are governed by subtle but interdependent parameters, including coordination geometry, defect density, pore architecture, and interfacial coupling. While enhanced conductivity and ion transport are often achieved through increased complexity, excessive structural precision can compromise robustness and reproducibility. Future studies should focus on identifying tolerant design windows that deliver reliable performance across different MOF families.

5. Applications in energy storage-advances in c-MOF-based electrodes for Li-, Na-, and K-ion batteries and pseudocapacitive systems

Conductive metal–organic frameworks have begun to reshape how we think about electrodes in modern energy-storage systems. What makes them stand out is their ability to merge crystalline order with genuine electronic conductivity-something that traditional MOFs could never offer. Over the past few years, researchers have started using c-MOFs not just as model materials, but as functional electrodes in batteries, supercapacitors, and even emerging redox-flow systems. Their tunable pore networks, open metal sites, and extended π-conjugated pathways allow ions and electrons to move with unusual efficiency, opening doors to higher capacities, faster kinetics, and better long-term stability. As a result, c-MOFs are no longer viewed as niche designer materials; they are now entering the conversation as practical candidates for next-generation storage technologies.

5.1 Zinc–air batteries

Zinc–air batteries rely on a straightforward yet highly efficient chemistry: zinc serves as the anode, while the air cathode catalyzes oxygen-related reactions that ultimately dictate the overall battery performance. During discharge, the oxygen reduction reaction (ORR) proceeds at the gas–liquid–solid interface, involving multiple electron-transfer steps that inherently slow down the reaction kinetics. A similar challenge exists for the oxygen evolution reaction (OER) during charging, where sluggish kinetics and catalyst degradation often limit reversibility.[201] Conventional ORR/OER catalysts-typically noble metals-deliver good activity but suffer from high cost and limited durability.[202,203] These constraints have pushed the field toward MOF-based catalysts and electrolytes, where the combination of structural tunability, abundant active sites, and emerging electronic conductivity provides a promising platform for stable, high-performance ZABs.[1,204] Recent progress highlights how MOFs can contribute not only as cathode catalysts but also as solid electrolytes and interfacial regulators for zinc-based systems. Xia and co-workers introduced an anionic MOF electrolyte constructed by coordinating oxo cluster, yielding a single-ion Zn^{2+} conductor with exceptional conductivity (0.83 mS cm^{-1} at −40 °C, 2.75 mS cm^{-1} at 25 °C, and 7.9 mS cm^{-1} at 120 °C), a remarkably high Zn^{2+} transference number ($t_{Zn^{2+}}$ = 0.90), low activation energy (0.19 eV), and excellent interfacial compatibility (Fig. 13a).[205] a carboxylic-acid-functionalized tetraphenylborate with a Zr_6-when paired with an $NH_4V_4O_{10}$ cathode in a quasi-solid-state zinc-ion battery (Fig. 13b), this MOF enabled efficient single-ion conduction pathways (Fig. 13c) and delivered impressive capacities of 497 mAh g^{-1} at 0.3 A g^{-1} under ambient conditions, retaining 420, 350, and 270 mAh g^{-1} at 1, 5, and 10 A g^{-1}, respectively, with nearly 100% capacity and coulombic efficiency maintained over 2500 cycles (Fig. 13d). Even at −40 °C or at ultrahigh current densities up to 100 A g^{-1}, the system sustained stable and reversible cycling, demonstrating how anionic porous frameworks can redefine electrolyte design for zinc and other multivalent batteries.[205]

Parallel advances have been made on the air-cathode side, where conductive MOFs offer a pathway to overcome the poor intrinsic conductivity and agglomeration tendencies of conventional MOF-based ORR catalysts. Liu *et al.* developed a room-temperature electrochemical cathodic electrodeposition strategy to form uniform, binder-free 2D bimetallic conductive MOF films using the HITP ligand and controlled Ni/Cu ratios (Fig. 13e).[206] Density functional theory analyses confirmed that the ORR activity could be fine-tuned through the electronic configuration of the metal centers, where unpaired 3d electrons and Jahn–Teller distortion in Cu sites optimize the adsorption energetics. The resulting $Ni_{2.1}Cu_{0.9}(HITP)_2$ electrode delivered a high ORR onset potential of 0.93 V and, when assembled into an aqueous ZAB, produced a specific capacity of 706.2 mAh g^{-1} and outstanding long-term cycling stability exceeding 1250 charge–discharge cycles. The discharge potential remained stable from 1–10 mA cm^{-2} and fully recovered upon current reversal, reflecting excellent reversibility. A red LED lamp could even be powered by two such batteries connected in series (Fig. 13f). The $Ni_{2.1}Cu_{0.9}(HITP)_2$ cathode outperformed both $Ni_3(HITP)_2$ and $Cu_3(HITP)_2$, showing higher specific capacities (706.2 *vs.* 685.3 and 536.7 mAh g^{-1}) and maintaining a nearly unchanged voltage gap after 1250 cycles (Fig. 13g).[206] Beyond cathodes and electrolytes, MOFs have also emerged as powerful regulators for zinc metal anodes. By comparing MOF-based interfacial layers with distinct channel sizes, researchers demonstrated that MOF-5W-with its confined pore network-strikes an ideal balance between ion flux and Zn^{2+} desolvation kinetics. Its activated surface sites promote spontaneous desolvation and accelerate Zn^{2+} migration through both internal channels and intergranular pathways. Consequently, MOF-5W@Zn anodes exhibit exceptional cycling durability, sustaining stable strip-

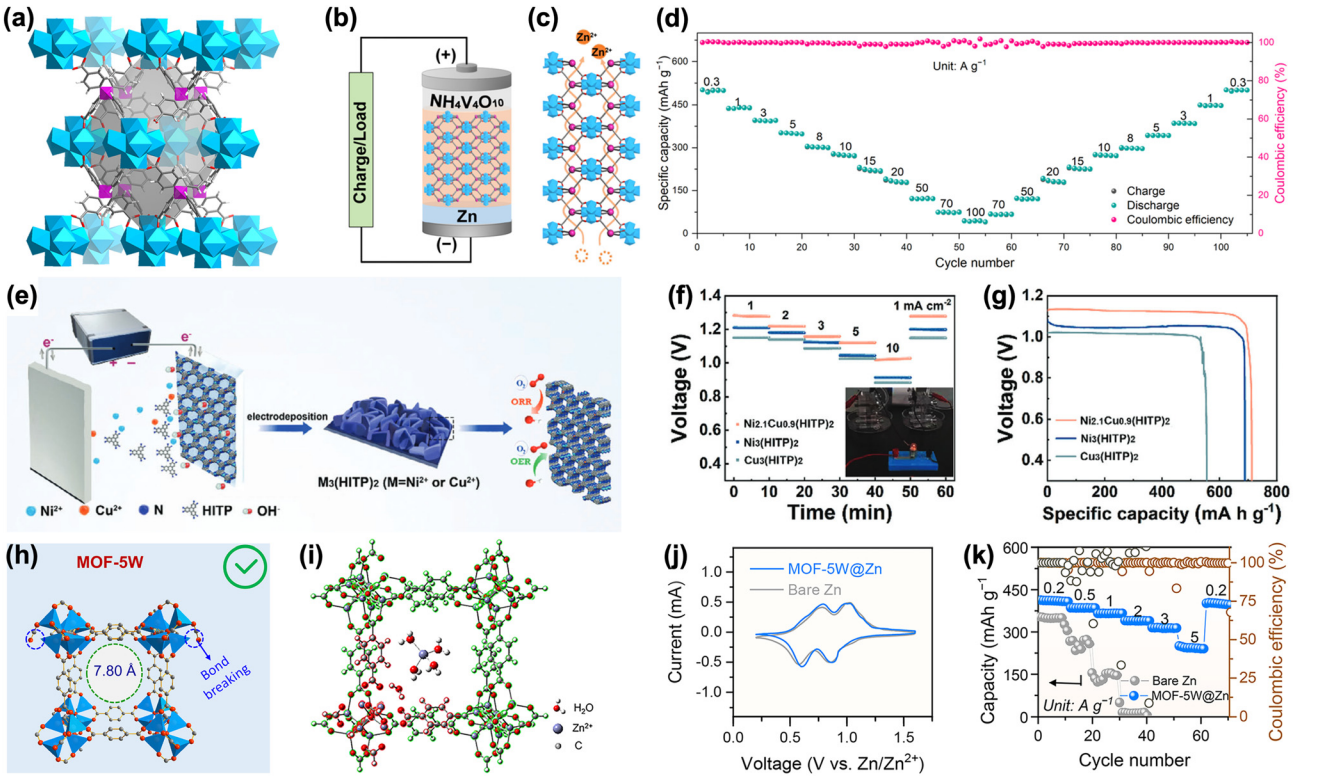

Fig. 13 (a) Three-dimensional porous architecture of the Zn-based MOF. (b) Schematic configuration of the Zn/$NH_4V_4O_{10}$ solid-state battery. (c) Illustration of Zn^{2+} single-ion transport pathways within the Zn-MOF framework. (d) Rate performance at current densities from 0.3 to 100 A g^{-1} at room temperature. Reproduced with permission from ref. 205 Copyright 2025 American Chemical Society. (e) Electrochemical deposition route for forming $M_3(HITP)_2$ (M = Ni^{2+} or Cu^{2+}) films on conductive substrates. (f) Discharge profiles recorded at 1, 2, 3, 5, 10, and 1 mA cm^{-2} (each step held for 10 min); inset shows a red LED powered by two $Ni_{2.1}Cu_{0.9}(HITP)_2$-based aqueous Zn–air batteries connected in series. (g) Discharge capacities measured at 5 mA cm^{-2}. Reproduced with permission from ref. 206 Copyright 2024 John Wiley and Sons. (h) Schematic of hydrated Zn^{2+} migration through the MOF-5 W coating layer. (i) Structural models depicting water adsorption in MOF-5 W. (j) CV curves of full cells using bare Zn and MOF-5W@Zn anodes. (k) Rate performance of full cells with different anodes. Reproduced with permission from ref. 207 Copyright 2024 Elsevier.

ping/plating for over 5000 cycles at 40 mA cm^{-2} and achieving a lifespan of 1050 h at an areal capacity of 10 mAh cm^{-2} (Fig. 13h). DFT calculations further revealed that hydrated Zn^{2+} species readily lose water within MOF-5 W channels, while the larger pores of MOF-808 allow free water molecules to occupy coordination sites and suppress desolvation (Fig. 13i). Subsequent electrochemical testing confirmed that MOF-5 W coatings do not negatively impact cathode behavior-CV curves for bare Zn and MOF-5W@Zn nearly overlap (Fig. 13j)-and significantly enhance full-cell rate performance in Zn//NVO batteries (Fig. 13k). These results highlight how pore-engineered MOF interlayers can simultaneously regulate solvation chemistry, ion transport, and surface stability, offering a robust strategy for long-life zinc metal anodes.[207]

5.2 Redox-flow batteries

Metal–organic frameworks have recently emerged as versatile components for redox flow batteries, contributing as electrode modifiers, catalytic interfaces, membrane fillers, and even dendrite-regulating layers for zinc-based systems. Their tunable porosity, well-defined coordination environments, and ability to be converted into functional metal oxides give MOFs a unique advantage in addressing the long-standing issues of sluggish kinetics, limited reversibility, and instability in aqueous RFB chemistries. The earliest set of advances involved the use of MOF-derived metal oxides to enhance electrode activity in zinc-hybrid RFBs. A NiO/ZnO composite derived from Ni-MOF and Zn-MOF precursors was deposited onto carbon felt (CF) *via* a solid-state reaction followed by ultrasonication, forming an asymmetric electrode configuration for zinc-hybrid RFB testing (Fig. 14a). SEM imaging revealed a superimposed hexagonal and irregular morphology (Fig. 14b), where the Ni-MOF/NiO species overlapped with Zn-MOF/ZnO, producing a roughened microstructure that increases surface irregularity and enables faster ion transfer. HR-TEM analysis further confirmed irregular particle domains (80–90 nm) and crystalline features in the composite (Fig. 14c). Electrochemical testing demonstrated that the NiO/ZnO-modified CF significantly improved Zn^{2+}/Zn redox kinetics, producing a peak current nearly three times higher than pristine CF, owing to the increased number of active sites. During cycling at 40 mA cm^{-2}, the asymmetric electrode configuration exhibited superior voltage efficiency (~88%) and stable operation for the first 25 cycles (Fig. 14d), confirming that pristine CF as the

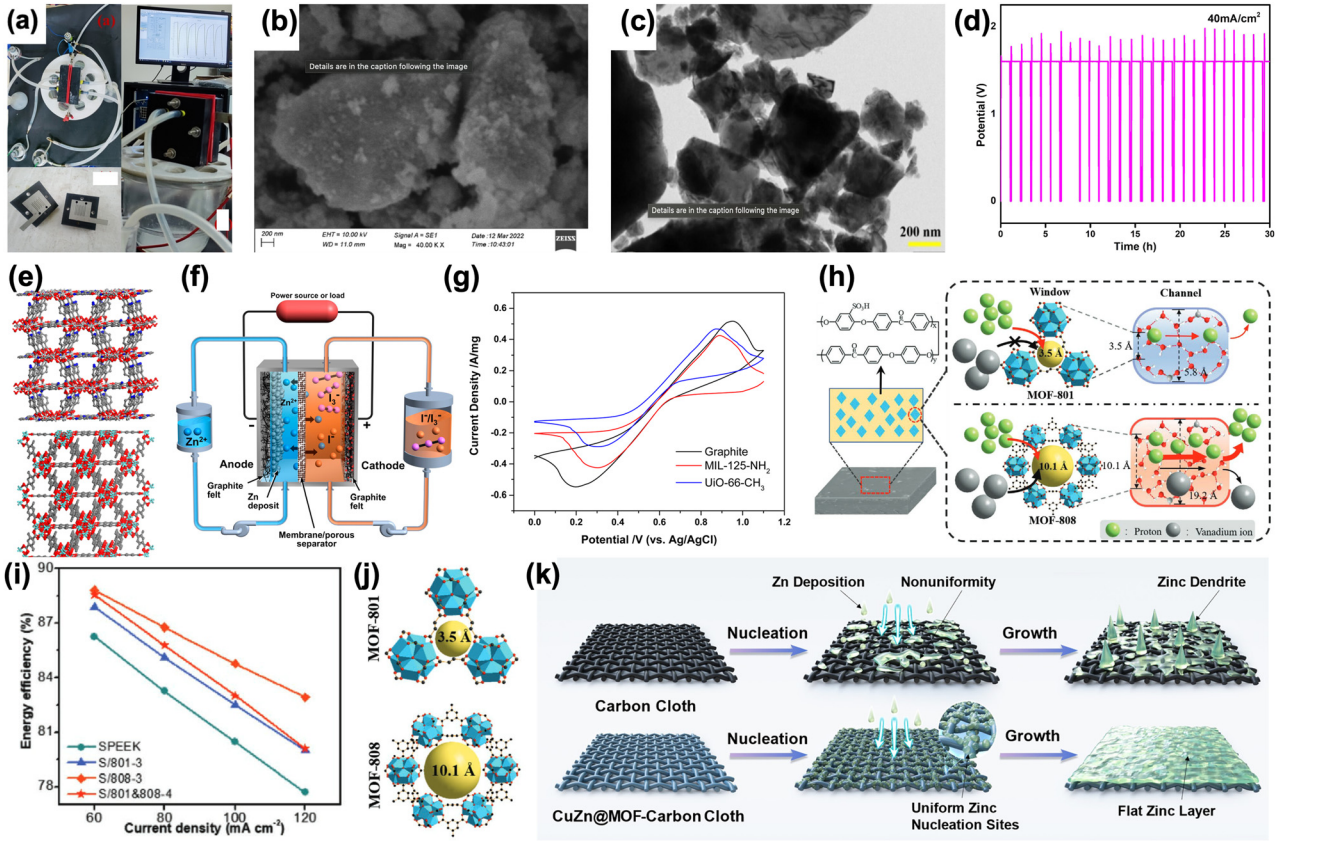

Fig. 14 (a) Schematic representation of the flow-cell setup incorporating a mini peristaltic pump, battery tester, and graphite-felt flow field for RFB operation. (b) SEM images of MOF-derived NiO/ZnO composite showing superimposed hexagonal and irregular morphologies. (c) TEM micrographs of the NiO/ZnO composite confirming irregular particle domains and crystalline features. (d) First 25 charge–discharge cycles of the asymmetric electrode configuration (pristine CF as positive; NiO/ZnO-coated CF as negative) in a zinc-hybrid RFB. Reproduced with permission from ref. 208 Copyright 2023 John Wiley and Sons. (e) Crystal structures of MIL-125-NH_2 (top) and UiO-66-CH_3 (bottom) used as MOF electrocatalysts. (f) Schematic illustration of the zinc–polyiodide redox flow battery system. (g) CV curves of MIL-125-NH_2/graphite, UiO-66-CH_3/graphite, and graphite electrodes recorded at 20 mV s^{-1} in mixed 0.25 M ZnI_2/0.25 M ZnI_6^{2-} electrolyte. Reproduced with permission from ref. 66 Copyright 2015 John Wiley and Sons. (h) Illustration of SPEEK membranes incorporating acid-stable MOF-801 or MOF-808 as pore-tunable fillers. (i) Energy efficiency comparison of VRFB membranes (N212, SPEEK, S/801–3, S/808–3, S/801&808–4) at 40–120 mA cm^{-2}. (j) Structural comparison of MOF-801 (top) and MOF-808 (bottom) showing distinct triangular (≈3.5 Å) and hexagonal (≈10.1 Å) windows. Reproduced with permission from ref. 209 Copyright 2021 John Wiley and Sons. (k) Schematic of zinc nucleation/deposition behavior on carbon cloth (CC) *versus* CuZn@MOF-coated carbon cloth. Reproduced with permission from ref. 210 Copyright 2024 Elsevier.

positive electrode limits symmetry and reduces cell performance.[208]

Building on electrode engineering, Li *et al.* explored Zr- and Ti-node-based MOFs as electrocatalysts in zinc-polyiodide RFBs to address the sluggish I_3^-/I^- redox kinetics that typically plague graphite-felt electrodes. The introduction of two high-surface-area MOFs-MIL-125-NH_2 and UiO-66-CH_3 (structures shown in Fig. 14e)-into the zinc-polyiodide flow cell (schematic in Fig. 14f) dramatically accelerated the I_3^-/I^- conversion process. CV studies (Fig. 14g) revealed higher redox currents for MOF-decorated electrodes compared to pure graphite, confirming enhanced reaction reversibility. At 30 mA cm^{-2}, MIL-125-NH_2 and UiO-66-CH_3 improved the energy efficiency by 6.4% and 2.7%, respectively, with UiO-66-CH_3 showing superior chemical stability in mildly acidic electrolytes.[66] This demonstrated that MOFs can directly address limitations in electrochemical activity and reversibility commonly seen in polyiodide-based RFB chemistries. Following MOF-based electrode catalysis, attention shifted to membrane engineering-another bottleneck in RFB performance.

Acid-stable Zr-MOFs (MOF-801 and MOF-808) with precisely tuned pore structures were incorporated into SPEEK membranes to enhance ion selectivity and reduce crossover (Fig. 14h). The optimized binary composite membrane (S/801&808–3) exhibited the highest energy efficiency among all tested membranes (Fig. 14i). MOF-801, with its smaller triangular pore window (~3.5 Å), and MOF-808, with its larger hexagonal windows (~10.1 Å) (Fig. 14j), both contributed distinct ion-sieving characteristics. Membranes containing MOF-801 showed markedly improved coulombic efficiencies of 98.5–99.2% at 40–120 mA cm^{-2}, outperforming pristine SPEEK (97.1–98.5%). These results underscored how MOF fillers can translate molecular-scale sieving properties into macroscopic membrane performance enhancements for flow batteries.[209]

Most recently, MOFs have been used to address one of the most critical challenges in zinc-based RFBs: zinc dendrite formation. In 2024, Wang and co-workers developed a bimetallic organic framework coating on carbon cloth (CuZn@MOF-CC) *via* a single-step dip-coating strategy to suppress dendrite growth.[210] On pristine carbon cloth, zinc nucleation is sparse and uneven, leading to localized growth and eventual dendrite formation. In contrast, CuZn@MOF-CC provides abundant zincophilic nucleation sites, significantly reducing nucleation overpotential and promoting uniform Zn deposition. Over time, this produces a smooth, dense zinc layer rather than dendritic structures (Fig. 14k). DFT calculations confirmed strong electronic interactions between Zn atoms and Cu sites within the MOF chain, explaining the improved deposition behavior. The resulting zinc anode achieved more than 450 dendrite-free cycles at a high current density of 320 mA cm^{-2}, demonstrating major improvements in cycle life, coulombic efficiency, and operational safety. Together, these studies highlight and establish MOF chemistry as a powerful tool for next-generation large-scale energy storage. Table 4 summarizes recent development of various types of c-MOFs based RFBs.

5.3 Supercapacitors

The development of conductive MOFs for high-performance supercapacitors has advanced through several distinct structural and mechanistic milestones. Supercapacitors have emerged as key electrochemical energy-storage devices owing to their high power density, fast charge–discharge capability, and outstanding cycling lifetimes relative to conventional batteries.[211,212] Their operation is governed by two principal charge-storage mechanisms.[213] The first is electric double-layer capacitance (EDLC), where an applied electric field induces the ordered accumulation of electrolyte cations and anions at the electrode surface, forming an electric double layer.[214,215] This process is highly surface-dependent and therefore favours materials with large accessible surface areas.[216] The second mechanism, pseudocapacitance, arises from rapid and reversible redox or chemisorption reactions involving electroactive species at or within the electrode.[217,218] Achieving high pseudocapacitance requires electrode architectures with abundant redox sites and well-developed porous networks.[219] Although carbon materials,[220] conductive polymers,[221] and transition-metal oxides[222] have been widely investigated, their high cost, limited stability, or insufficient rate capability often constrain practical performance.[227] In contrast, conductive MOFs-combining intrinsic electronic conductivity with high surface area, tunable porosity, and dense arrays of accessible active sites-are increasingly regarded as promising candidates for next-generation supercapacitor electrodes. Early work, by Yaghi and co-workers exhibited conductivity as high as 20 S m^{-1} which remains one of the highest values reported so far.[58,228,229] In this regard, exemplified by Fig. 15a, established Cu-CAT as a model conductive framework, where one-dimensional π–d channels along the *c*-axis provide well-defined pathways for ion migration and electronic transport. Translating these structural advantages into practical electrodes, Fig. 15b shows vertically aligned Cu-CAT nanowire arrays (NWAs) grown directly on carbon fiber paper, enabling efficient electron percolation and high exposure of electroactive sites. Their redox characteristics are confirmed through the multi-rate CV profiles in Fig. 15c, and their device applicability is demonstrated by a solid-state configuration capable of powering an LED (Fig. 15d).[223] To overcome the intrinsic brittleness and limited flexibility of MOFs, subsequent studies incorporated conductive frameworks into nanofibrous substrates. The CNF@c-MOF architecture illustrated in Fig. 15e and the corresponding transport schematic in Fig. 15f highlight how cellulose nanofibers provide a mechanically robust and ion-permeable scaffold that stabilizes the MOF domains while facilitating multidirectional ion diffusion. These structural advantages manifest in the widened-window CV responses (Fig. 15g) and the excellent cycling retention over thousands of cycles (Fig. 15h).[224] With the emergence of electronically conjugated frameworks such as NiHAB, attention shifted toward understanding ion-pore interactions that regulate capacitance. Fig. 15i compares the hydrated radii of Li^+, Na^+, K^+, TBA^+, and THA^+ ions with the calculated pore aperture, revealing a strong dependence of charge storage on size compatibility. Corresponding CV measurements in different alkaline electrolytes (Fig. 15j) validate this trend experimentally, indicating that smaller cations capable of accessing the interior redox centers yield markedly higher current responses.[225] Building upon these mechanistic insights, newer designs have focused on synergistic hybridization to enhance conductivity and structural durability. The CNT-interwoven Cu-MOF composite shown in Fig. 15k demonstrates how carbon nanotube wiring dramatically improves electron mobility, leading to stable capacitive cycling and additional electrocatalytic activity toward hydrogen evolution. Finally, interfacial engineering strategies-such as the Co-MOF@MXene hybrid-provide a powerful route to tune charge transfer at the atomic level.[226] Fig. 15l depicts the layered composite architecture, while Fig. 15m presents the corresponding structural models, revealing strong electronic coupling and optimized active-site environments.[88] Collectively, these figures trace the evolution of conductive MOFs from crystalline frameworks to hierarchical, fiber-supported, and interface-engineered hybrids, underscoring the design principles that now guide the development of next-generation MOF-based supercapacitor electrodes. Table 1 summarizes recent development of various types of c-MOFs based supercapacitors.

5.4 Lithium-ion batteries

Lithium-ion batteries remain the dominant rechargeable energy-storage technology owing to their high energy density and excellent operational stability, which derive from the reversible intercalation and deintercalation of Li^+ ions at the positive and negative electrodes.[230] Commercial LIBs largely rely on graphite anodes and transition-metal-based cathodes; however, the capacity of graphite (372 mAh g^{-1}) is already close to its theoretical ceiling,[231–233] and many transition-metal compounds offer specific capacities below 200 mAh

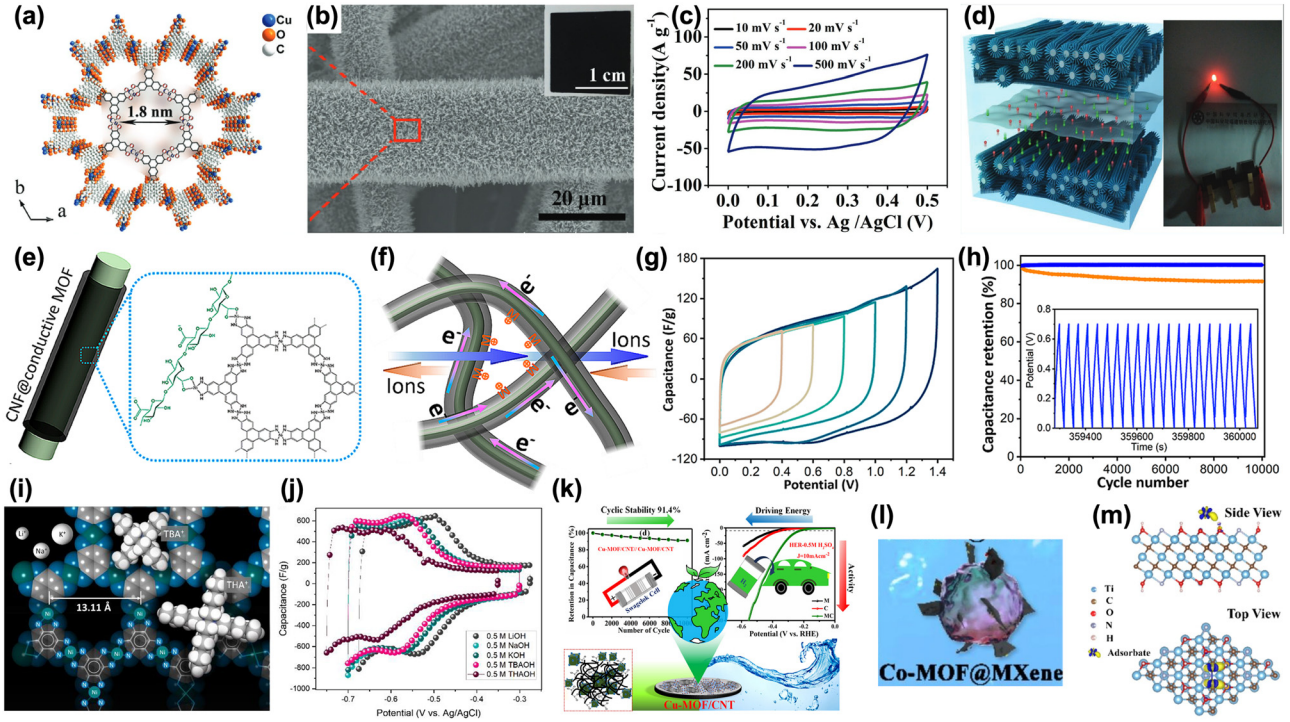

Fig. 15 (a) Crystal structure of Cu-CAT. (b) SEM image of vertically aligned Cu-CAT nanowire arrays grown on carbon fiber paper. (c) CV curves of the Cu-CAT NWAs electrode recorded in a three-electrode configuration at various scan rates. (d) Structural illustration of the assembled solid-state supercapacitor (left) and a demonstration of three devices connected in series powering a red LED (right). Reproduced with permission from ref. 223 Copyright 2017 John Wiley and Sons. (e) Schematic representation of the CNF@conductive-MOF composite architecture. (f) Charge-transfer and ion-transport pathways within the intertwined nanofibrous and conductive networks of CNF@c-MOF nanopapers. (g) CV curves of the CNF@Ni-HITP double-layer supercapacitor at a scan rate of 10 mV s^{-1}. (h) Cycling stability and capacitance-retention profiles of the device operated within 0–0.7 V (blue) and 0–1.0 V (orange). Reproduced with permission from ref. 224 Copyright 2019 American Chemical Society. (i) Schematic illustration comparing the sizes of various cations with the calculated pore aperture of the NiHAB MOF. (j) CV profiles of NiHAB electrodes measured in 1 M LiOH, NaOH, KOH, TBAOH, and THAOH electrolytes at a scan rate of 1 mV s^{-1}. Reproduced with permission from ref. 225 Copyright 2020 American Chemical Society. (k) Illustration of the Cu-MOF/CNT composite demonstrating its long-term cycling stability and electrocatalytic energy-conversion capability. Reproduced with permission from ref. 226 Copyright 2024 American Chemical Society. (l) Schematic diagram of the Co-MOF@MXene composite structure. (m) Constructed atomic-level models of Co-MOF@MXene showing side and top views of the interfacial configuration. Reproduced with permission from ref. 88 Copyright 2020 Royal Society of Chemistry.

g^{-1},[234,235] leaving limited headroom for performance enhancement. Organic redox-active molecules-such as heterocyclic aromatic systems containing C═N, C≡N, and N═N groups-offer attractive theoretical capacities,[236] but their solubility in organic electrolytes severely limits long-term cycling.[237] Conductive MOFs provide an elegant solution, as coordinating metal ions with π-conjugated, redox-active organic linkers yields robust crystalline networks that are inherently insoluble, structurally stable, and capable of sustaining multi-electron redox processes.[238] Beyond π-conjugated conductive frameworks, several structurally diverse MOFs-such as Co/Ni-based electroactive MOFs,[239] dual-ligand Zn-MOFs,[240] and Pb-MOF-derived porous anodes[241] have also shown remarkable Li-storage reversibility. Their performance arises from the presence of redox-active metal centers, abundant open-metal sites, and tunable pore geometries, which together enhance Li^+ uptake, buffer structural changes, and stabilize multi-electron conversion mechanisms. These examples further underscore the breadth of MOF design strategies accessible for LIB anodes. Building upon this broader landscape, recent advances in π-conjugated conductive MOFs have delivered even greater electronic conductivity and faster Li^+ transport, as illustrated in the following representative systems (Fig. 16a–h). Their ordered porosity, abundant active sites, and intrinsic electronic conductivity collectively facilitate rapid Li^+ intercalation and deintercalation, positioning conductive MOFs as a promising class of next-generation electrode materials. Against this backdrop, the following papers highlight recent advances in structural design, redox mechanisms, and electrolyte compatibility that have enabled conductive MOFs to deliver high capacities, fast kinetics, and exceptional cycling performance in LIB systems. A representative example is the Cu-TAC framework, whose optimized structure is shown in Fig. 16a. The model reveals a highly ordered pore network with a 1.9 nm aperture, large enough to accommodate solvated Li^+ species while maintaining a rigid π-conjugated environment around the CuO_4 coordination sites. This structural arrangement enables efficient ion diffusion and facilitates multi-electron redox processes. The resulting electrochemical behavior is reflected in the rate-capability data in Fig. 16b, where the Cu-

Table 1 Summarizes recent development of c-MOFs-based materials for supercapacitors

No.	c-MOF	Electrolyte	Potential window	Specific capacitance in F g^{-1} (current in A g^{-1})	Cyclability (retention%; cycle; current in A g^{-1})	Ref.
1	$CuCo_2S_4$@FeS_2	3 M KOH	0 to 0.55	727.6(1)	89.41; 5500; 10	282
2	Co-MOF/$Ti_3C_2T_x$	3 M KOH	0 to 0.5	3741(0.833)	92.1; 2500; 0.167	283
3	NiMn-LDH/NiCo-MOF (800 s)	1 M KOH	0 to 1.5	1411.30(0.5)	83; 5000;	284
4	Cu-CAT-Rad	3.0 M KCl	-0.4 to 0.4	508(0.2)	88.4; 5000; 0.2	285
5	$Ni_3(HITP)_2$	1 M $TEABF_4$/ACN	0 to 1	111(0.5)	90; 10 000; 2	67
6	ZIF/PPy	1 M Na_2SO_4	0 to 0.6	597.6(0.5)	90.7; 10 000; 20;	286
7	Cu-MOF/rGO	1 M Na_2SO_4	0 to 0.6	685.33(1.6)		287
8	$Cu_3(HHTATP)_2$	1 M KCl	0 to 1	264(0.5)	94; 7000; 5	98
9	Cu-MOF/PANI	1 M H_2SO_4	0 to 1	160.5(0.5)	93; 5000; 10	288
10	Ni_3Co_1-DPTTZ-MOF	3.0 M KOH	0 to 0.4	577.7(1)	77.1; 5000; 5	289
11	NiV-LDH@P,Se-doped VNi-MOF/NF	6 M KOH	−0.3 to 0.8	2083(1)	90; 10 000; 10	290
12	Zn-MOF (MOF-1) with 75% BTC and 25% BDC	6 M KOH	−0.78 to −0.1	683(0.5)	—; 1000; 0.5	291
13	$Ni_3(HITP)_2$	0.5 M Na_2SO_4	0 to 1.00	170 (0.1 mA cm^{-2})	84%; 100 000; 0.1 mA cm^{-2}	292
14	CNF@Ni-HITP	PVA/KCl gel	0 to 1.00	141 (0.075)	90%; 10 000; 1.0	293
15	LSG/Ni-CAT	PVA/LiCl gel	0 to 1.40	15 mF cm^{-2} (0.2 mA cm^{-2})	87%; 5000; 2.0 mA cm^{-2}	294
16	$Ni_3(HITP)_2$	[EMIM][BF_4]	2.10 to 2.80	58, 70, 76 (5.0 mV s^{-1})	—	295
17	Exfoliation $Co_3(HITP)_2$	1 M LiTFSI	0 to 2.25	—	85%; 10 000; 0.5	296
18	$Cu_3(HHTP)_2$	1 M NEt_4BF_4/ACN	0 to 1.00	114 (0.05)	81%; 30 000; 1.0	297
19	$Cu_3(HTTP)_2$ (NWAs on Cu foils)	1 M KCl	−0.60 to 0.02	215 (0.5)	79%; 5000; 10.0	298
20	Cu–CAT NWAs	3 M KCl	−0.40 to 0.50	202 (0.5)	80%; 5000; 0.8 V s^{-1}	223
21	Ni-HAB	1 M KOH	−0.75 to 0.25	420 (0.2 mV s^{-1})	90%; 12 000; 10.0	299
22	$Ni_3(HAB)_2$	0.5 M Na_2SO_4	0 to 1.00	279 (0.1 mA cm^{-2})	81%; 50 000; 1.0 mA cm^{-2}	300
23	$Ni_2[CuPc(NH)_8]$	3 M KCl	−0.80 to 0.80	400 (0.5)	90%; 5000; 10.0	301
24	$Zn_{3.68}Co_{0.32}O(BDC)_3(DEF)_{0.75}$	0.1 M $TBAPF_6$	−1.00 to 0.20	—	92%; 1000; 10.0 mA g^{-1}	302
25	Layered Co-PTA	5 M KOH	0 to 0.35	2564 (1.0)	95%; 3000; 2.0	303
26	Co-PTA	1 M LiOH	0 to 0.60	206 (0.6)	98%; 1000; 0.6	304
27	Ni–Co–$Mn_{0.25}$-PTA	1 M KOH	0 to 0.50	1575 (1.0)	81%; 5000; 2.0	305
28	Ni/Co-BTC (5 : 1)	6 M KOH	0 to 0.60	1498 (1.0)	71%; 3000; 5.0	306
29	$[Ni_3(OH)_2(C_8H_4O_4)_2(H_2O)_4]\cdot 2H_2O$	3 M KOH	0 to 1.30	1021 (0.7)	96%; 5000; 1.4	307
30	$[Ni_3(OH)_2(C_8H_4O_4)_2(H_2O)_4]\cdot 2H_2O$	6 M KOH	0 to 0.35	1127 (0.5)	90%; 3000; 2.0	308
31	Zn-pPDA MOF-5	1 M KOH	−0.30 to 0.70	200 (1.0)	96%; 2000; 1.0	309
32	Co-BTC microspheres	1 M LiOH	0 to 0.60	55 (1.0)	90%; 2000; 6.0	310
33	Cu-BTC-120	3 M KOH	0 to 0.50	228 (1.5)	89%; 3000; 3.0	311
34	Co-HAB	1 M $NaPF_6$	0.50 to 3.00	—	100%; 50; 50.0 mA g^{-1}	312
35	Cu-HAB	1 M KOH	−0.55 to 0.10	215 (0.2 mV s^{-1})	—	299

TAC electrode maintains stable and reversible capacity across a wide current-density range (50–1500 mA g^{-1}). The retention of meaningful capacity even at high rates highlights the rapid Li^+ transport and the intrinsic electronic conductivity imparted by the conjugated TAC ligand.[242]

The underlying Li^+ storage mechanism is further illustrated in Fig. 16c, which outlines the stepwise redox transitions occurring on both the CuO_4 moieties and the TAC organic units. The inorganic Cu centers undergo reversible $Cu^{2+}/Cu^+/Cu^0$ transformations, while the extended π-systems of the TAC ligand participate in additional electron transfer steps.[242] This cooperative inorganic–organic redox behavior significantly amplifies the charge-storage capacity compared to purely metal-based or ligand-based mechanisms. Beyond Cu-TAC, related MOF families derived from the DOBDC ligand (2,5-dihydroxyterephthalic acid) have been systematically tuned to control metal identity, coordination environment, and lithium content. The synthetic routes summarized in Fig. 16d demonstrate the preparation of H_2-M-DOBDC·DMF_2, H_2-M-DOBDC, and Li_2-M-DOBDC (M = Mn, Mg), where the reversible insertion of lithium into the metal-DOBDC framework enables the formation of Li_2-M-DOBDC without structural collapse.[243] The corresponding optical micrographs highlight the morphological uniformity and distinct coloration of each phase, providing visual confirmation of the successful synthetic transformations.

The electrochemical behavior of these Li-inserted DOBDC structures is examined in Fig. 16e, which compares the discharge capacity and coulombic efficiency of Li_2-Mn-DOBDC across multiple electrolyte formulations.[243] Remarkably, the material exhibits high capacity retention and strong reversibility after 100 cycles in several solvent systems, indicating that both the metal-centered redox activity and the ligand coordination environment remain stable under repeated lithium cycling. This electrolyte-dependent performance trend underscores the importance of ion solvation, interfacial compatibility, and Li^+ desolvation kinetics in determining overall MOF electrode behavior. Further mechanistic insight is provided by the Li^+ and PF_6^- migration scheme in Fig. 16f, which shows the structural evolution of the Cu-THQ framework during charge–discharge.[244] As Li^+ inserts and extracts, both the aromatic THQ ligand and the Cu coordination sphere undergo reversible electron redistribution, while PF_6^- interacts weakly with the framework without causing lattice degradation. This ion-coupled molecular breathing effect is characteristic of conductive MOFs and contributes to their excellent structural

Table 2 Summaries recent development of c-MOFs-based materials for various types of batteries

No.	c-MOF	Role	Battery type	Specific capacity (current in mAh g^{-1})	Reversible capacity (current in mAh g^{-1}; cycles; retention)	Ref.
1	Cu-BHT	Cathode	Li-ion (1.5–3)	232 (50)	175 (300; 500; 92.4)	313
2	Cu-CAT	Anode	Li-ion (0.01–3)	631 (200)	540 (500; 500; 81)	314
3	Ni-TIB	Anode	Li-ion (0.8–2.0)	200 (20 000)	83 (20 000; 20 000; 79)	315
4	Ni-DI	Cathode	Li-ion (2–4.5)	155 (10)	~50 (250; 300)	316
5	2D Cu-THQ	Cathode	Li-ion (1.2–4.0)	387 (50)	340 (50; 100; 85)	317
6	ZnCo-MOF/S	Cathode	Li–S (2.8–1.7)	1076 (167)	688 (837; 300; 85)	318
7	$Cu_3(HHTP)_2$	Cathode	Li ion (1.7–3.5)	94.9		319
8	Ni-CAT NRs	Anode	Li-ion (0.01–3)	~982 (0.2)	626 (0.2; 200)	320
9	Cu-CAT NWs	Anode	Li-ion (0.01–3)	713 (200)	646 (200; 320; 91)	314
10	Cu-HHTQ	Anode	Li-ion (0.01–3)	989 (15)	657.6 (600; 200; 82)	321
11	Fe(dhbq)	Cathode	Li-ion (1.5–4)			322
12	$S@Ni_3(HITP)_2$-AB	Cathode	Li–S (1.7–2.8)	1022 (335)	703.2 (335; 100; 95.4)	69
13	Ni-MOF-1D	Cathode	Li–S (0.1–0.5)	1491 (0.1)	869 (0.1; 200; 94.8)	251
14	$Ni_3(HITP)_2$	Separator	Li–S (1.8–3.0)	1220.1 (167.5)	600 (837.5, 200, 70)	323
15	Co/NCNS/CNT	Separator	Li–S (1.6–2.8)	1037.7 (837.5)	799.2 (837.5; 200; 77)	324
16	Janus MXene/MOF	Separator	Li–S (1.7–2.8)	1275.5 (167.5)	687 (167.5; 100; 54)	325
17	ZIF-67/PMIA@PVDF-HFP (MOF-PPH)	Separator	Li–S-PAN (1–3)	1406.1 (335)	1349.1 (335; 200; 95.6)	326
18	UiO-66-F@PP	Separator	Li-ion (2.4 V to 4.2 V)	160 (34)	110 (170; 1000; 84.8)	327
19	glass fiber (GF)@UiO-66-NH_2 + HFP	Separator	Li-ion (2.8 to 4.3 V)	164 (200)	157 (200; 200; 89.3)	328
20	Mn-MOF nanowires (MMNWs)	Separator	Li-ion (2–3.7)	163 (34)	148 (34; 100; 90.8)	329
21	HATN-O-Zn	Anode	Na-ion (0–3)	462 (100)	319 (100; 300)	272
22	Nd-cMOF/ZIF-10-CF	Anode	Na-ion (0–3)	480.5 (100)	409 (100; 500; 85.1)	330
23	Ni-MOF	Anode	Na-ion (0.5–3)	297 (50)	145 (1000; 500; 84)	331
24	Co-HAB-D	Anode	Na-ion (0.5–3.0)	291(50)	226(500; 50)	312
25	NiSx@C-600	Anode	Na-ion (0–3)	987.7 (200)	432.8 (200; 100)	332
26	NFPF-Al/MC	Cathode	Na-ion (2.0–4.0)	115.2 (0.1)	84.3 (1; 100; 88.5)	333
27	P@N-MPC	Anode	Na-ion (0.005–3)	710 (150)	600 (150; 100; 84.5)	334
28	$BiPS_4$/C@Ni-HHTP	Anode	Na-ion (0.01–3.0)	1181.3 (100)	794.1 (100; 50; 67.3)	128
29	CoS_2/NC/S-3	Anode	NC/S (0.8–2.8)	944 (100)	403 (1000; 1000)	335
30	Cu-TBA	Cathode	Na-ion (1.0–3.5)	153.6 (50)	~100 (1000; 3000)	336
31	Cu_2Se@C	Anode	Na-ion (0.5–3)	267.8 (100)	268 (100; 100)	337
32	Cu-TBP	Anode	Na-ion (0–3)	594 (100)	288.4 (1000; 1000; 73.2)	338
33	M_3DP-MXene/Cu-THBQ/Zn-P//G-TEMPO	Anode	Zn-ion (0.4–1.9)	235.4 (200)	223 (4000; 1200; 96.8)	339
34	$Cu_3(HHTP)_2$	Cathode	Zn-ion (0.5–1.3)	228 (50)	124.4 (4000; 500; 75)	340
35	Fe-MET MOF	Cathode	Zn-ion (0.2–1.8)	34 (20)	16 (50; 1200; 60)	341
36	Cu-BTA-H	Cathode	Zn-ion (0.3–1.6)	330 (200)	106.1 (2000; 500)	342
37	DDA-Cu	Cathode	Zn-ion (0.2–1.5)	249.6 (200)	124.8 (200; 200)	343
38	2D Cu-TABQ	Cathode	Zn-ion (0.3–1.5)	294 (200)	98.2 (200; 1000)	344
39	Cu-TABQ	Cathode	Zn-ion (0.2–1.5)	288.6 (50)	110 (4000; 780)	345
40	Cu-TBPQ MOF	Cathode	Zn-ion (0.3–1.4)	371.2 (50)	136.7 (2000; 500; 88)	168
41	ZnCo-MnO/C	Cathode	Zn-ion (0.8–1.9)	~90 (2000)	135.35 (2000; 2000; 93.8)	346
42	MnO_x@N–C	Cathode	Zn-ion (0.8–1.8)	~160 (500)	305 (500; 600)	347
43	HAN-Cu-MOF	Anode	K-ion (0–3)	455 (50)	238 (500; 1000; 95.8)	274
44	Co-MOF-rGO	Anode	K-ion (0–3)	701 (200)	364 (200; 200)	348
45	Co-SNCS-t	Anode	K-ion (0.001–3.0)	209.3 (100)	86.1 (1000; 2000; 93.4)	277
46	Co-CAT MOF	Anode	K-ion (0.001–3.0)	390.3 (200)	230 (1000; 700)	349
47	$[C_7H_3KNO_4]_n$	Anode	K-ion (0.001–2.0)	~200 (10)	123 (50; 150; 90)	6
48	UCF@CNs@BiN	Anode	K-ion (0.001–3.0)	665 (100)	425 (100; 50; 64)	350
49	ZnSe@PCNF	Anode	K-ion (0.01–3.0)	555 (100)	270 (500; 1000)	351

durability. Finally, Fig. 16g–h highlight the design and operation of the Cu-HATN 2D c-MOF, constructed from redox-active HATN (hexaazatrinaphthalene) units coordinated to Cu nodes.[245] The molecular structure shown in Fig. 16g reveals an extended conjugated network that enables intrinsic in-plane electronic conductivity, while the open channels facilitate rapid Li^+ transport. The lithium-storage pathway depicted in Fig. 16h shows successive multi-electron redox events distributed across the HATN ligand and the Cu centers, yielding high capacities and smooth discharge profiles. In addition to this, together, these results demonstrate how rational design of both the inorganic nodes and the ligand electronics enables conductive MOFs to support fast ion diffusion, robust structural stability, and high charge–storage capacities suitable for advanced lithium-ion energy-storage applications energy-storage applications.

5.5 Lithium–sulfur batteries

The exceptionally high theoretical capacity of elemental sulfur (1675 mAh g^{-1}), nearly five times that of $LiCoO_2$, makes Li–S batteries an appealing next-generation system.[246] However, their practical deployment is limited by several intrinsic challenges: the insulating nature of sulfur and lithium polysulfides leads to sluggish reaction kinetics, dissolved polysulfides

Table 3 Representative physical and transport properties of MOFs and their derived materials for energy-storage applications

No.	MOFs-type	Size/morphology	Porosity ($m^2 g^{-1}$)	Electronic conductivity ($S cm^{-1}$)	Ionic/charge transport feature	Application	Ref.
1	$Ni_3(HITP)_2$	2D layered sheets	~630	~5000	Band-type π–d delocalization	Supercapacitor	67
2	Porphyrin-MOF (Ni-Por)	300 nm/2D nanosheets	~629	~40	Redox-assisted transport	Zn-battery	352
3	Co-MOF	8.23 to 9.36 nm/ nanosheets	Porous	Moderate	Electron transfer	Hybrid supercapacitors	283
4	NiMn-LDH/NiCo-MOF (800 s)	0.23 to 0.26 nm nanosheets	Porous	High	Ion diffusion and electron conduction	Supercapacitor	284
5	Cu-MOF	4.60 to 4.78 nm	1321	High	Matrix-assisted	Supercapacitor	288
6	Ni3Co1-DPTTZ-MOF	5–20 μm/microrods	Porous	0.00221	π-Conjugated ligand based electron transfer	Supercapacitor	.289
7	NiV-LDH@P	1 μm/nanorod	Porous	High	Doping	Supercapacitor	290
8	Cu3(HHTP)2	1.8 nm/3D honeycomb	794	0.007	Band-type π–d delocalization	Supercapacitor	297
9	MOF-76(Gd)	needle-like crystals	595	—	Band-type π–d delocalization	Lithium-sulphur batteries	353
10	Ni-MOFs/GO	Membranous	Porous	High	d–p electron conjugation	Lithium ion battery	176
11	MOF-5	10 and 25 mm/cubic aggregates	2151	50.15	ion diffusion and electron conduction	Zinc-ion batteries	193
12	PVDF-HFP $UiO\text{-}66\text{-}NH_2$ MIL-125 MOF-808	1 to 20 μm/ nanoparticles	2.5 303.9 233 3.0	0.0039 0.0031 0.0022 0.0024	Matrix-assisted	Lithium ion battery	182
13	$MIL\text{-}125\text{-}NH_2$ $UiO\text{-}66\text{-}CH_3$	0.6 and 1.2 nm/ Nanoscale dispersed	—	—	Redox-assisted transport	Redox-flow batteries	66
14	Ni/Co-MOF	0.35 and 0.37 nm/ crystalline	98.2	Moderate	Band-type π–d delocalization	Lithium-sulphur batteries	253
15	Bi-MOF-derived $BiPS_4$/C	7–45 nm/irregular bulk structure	398.3	High	Redox-assisted transport	Sodium-ion batteries	71
16	MOF-Fe_2O_3@CNFs@$Ti_3C_2T_x$	2–5 nm/uniform	31.5	High	Conducive 3D network	Lithium and Sodium-ion batteries	354
17	ZIF-67	2–20 nm/nanocubes	110	High	porous carbon matrix	Lithium ion battery	355
18	MOF 1	flat surface	561	0.0022	Nucleation/deposition	Zinc Batteries	356
19	NH2-UiO-66	500 nm/uniform octahedral	Porous	0.00036	Matrix-assisted	Li-O2 batteries	357
20	Ni–Co-ZIF	2–10 nm/rhombic dodecahedral	552	High	Band-type π–d delocalization	Sodium-ion batteries	358
21	Zif-8	3–40 nm/spherical nanocrystals	1486.3	High	Heteroatom-doping	Lithium-sulphur batteries	359

migrate through the electrolyte causing capacity loss and poor coulombic efficiency, and the large volumetric expansion of sulfur during cycling induces structural degradation.[247] Various host materials-such as carbon matrices, metal oxides, and metal sulfides-have been explored to confine sulfur, yet each presents drawbacks. Carbon materials offer good conductivity but weak interactions with polar polysulfides,[248] while metal oxides and sulfides strongly adsorb polysulfides but suffer from low conductivity, restricting redox conversion.[249] Conductive MOFs overcome these limitations by combining polar, size-confined porous architectures with intrinsic electronic conductivity. Their ordered pores provide nanoscale reaction spaces that suppress polysulfide dissolution and buffer sulfur expansion,[250] while their conductive frameworks accelerate the sulfur-polysulfide conversion kinetics.[251] These synergistic attributes make conductive MOFs highly attractive hosts for high-performance Li–S batteries. Fig. 17 brings together several MOF-based design strategies that jointly address the fundamental limitations of Li–S batteries, namely sluggish sulphur conversion kinetics, uncontrolled polysulphide shuttling, and poor long-term stability. The first approach focuses on defect engineering in Zr-MOFs. As shown in Fig. 17a–c, introducing missing-linker defects into MOF808 generates additional open metal sites and more accessible pore channels, enabling stronger chemisorption of Li_2S_x species and more efficient electronic/ionic pathways around the sulfur host. Consequently, the MOF808-D@PS electrode exhibits significantly slower capacity decay and more pronounced redox peaks than pristine MOF808@PS or elemental sulphur.

The reduced voltage polarization and sharper CV response confirm that defect-rich MOFs facilitate both faster electron transfer and more complete $Li_2S \leftrightarrow S_8$ conversion, demonstrating how subtle structural tuning within the MOF lattice directly enhances kinetic activity.[189]

Beyond defect incorporation, catalytic enhancement within the MOF framework provides another powerful route to accelerate sulphur chemistry. Fig. 17d illustrates the MOF-TOC host, where sub-nanometre Ti–O clusters are anchored inside the MIL-101(Cr) pores. These Ti–O clusters effectively immobilise long-chain polysulphides through strong Lewis acidic

Table 4 Summarizes recent development of c-MOFs-based materials for redox-flow batteries

No.	c-MOF	Components	Energy efficiency (%; current in mA cm^{-2})	coulombic efficiency (%; current in mA cm^{-2})	Cyclability (cycle; current in mA cm^{-2})	Ref.
1	CZ-5 (ZIF-8)	Electrode	67; 120	97; 120	5000; 100	360
2	PGF (ZIF-8)	Electrode	68.18; 200	—	3300; 250	361
3	SnO2/GF	Electrode	63.10; 250	—	200; 100	362
4	PNCS (ZIF-8)	Electrode	82; 80	—	200; 80	363
5	N,O/CF (ZIF-8)	Electrode	76.39; 300	—		364
6	PAECF (ZIF-8)	Electrode	79.30; 400	—	600; 200	365
7	N-PGF (ZIF-67)	Electrode	71.90; 300	—	5000; 300	366
8	MDC-GF (UIO-66)	Electrode	61.60; 120	—	100; 100	367
9	HGF-WZ (UIO-66)	Electrode	74.86; 160	97.52; 160	100; 140	368
10	HNC (ZnCo-ZIF)	Electrode	76.80; 400	96.00; 400	2000; 400	369
11	GF@Fe-N/S-CNFs (ZIF-8)	Electrode	62.10; 300	—	350; 150	370
12	NMPC-A (Ni-MOF)	Electrode	82.70; 200	—	1000; 200	371
13	ZrO2@C/GF	Electrode	75.20; 200	—	500; 150	372
14	GF@N C (ZIF-8)	Electrode	56.90; 370	—	175; 200	373
15	NiO/ZnO	Electrode	24.00; 1	38.00; 20	25; 40	208
16	MIL-125-NH2	Electrode	86.00; 10	98.00; 10	50; 30	66
17	UiO-66-CH_3	Electrode	85.00; 10	98.50; 10	50; 30	66
18	Zn-MOF/ZnO	Electrode	21.8; 5	23.70; 5	—	199
19	ZnCF-6	Electrode	79.30; 20	86.01; 20	14; 20	185
20	WZ-22–650	Electrode	83.94; 80	98.26; 80	100; 80	368
21	N/CAU-10-OH 0.3wt%	Electrode	74.81; 160	95.81; 160	50; 160	374
22	MDC-GF-900	Electrode	75.70; 80	97.20; 80	100; 100	367
23	Cu-MOFP-1	Electrode	66.52; 7.50	96.87; 40	40; 7.5	375
24	PANI-MIL-101/GC	Electrode	—	~100; 4	50; 4	376
25	ZrO_2@C	Electrode	75.20; 200	93.50; 50	500; 200	377
26	Ni-MOF	Membrane	85.10; 4	91.00; 4	100; 4	190
27	IMOF (Cd-MOF)	Membrane	85.70; 100	98.20; 100	100; 300	378
28	UIO-66-SO_3H/PVDF	Membrane	88.20; 4	99.00; 4	500; 4	379
29	UiO-66-NH_2/*s*-g-C_3N_4	Membrane	79.90; 150	98.80; 150	300; 150	380
30	Cu-BTC	Membrane	78.60; 4	97.40; 4	300; 4	381
31	S-U66	Membrane	76.10; 220	97.02; 220	1000; 80	382
32	MIL-101	Membrane	87.30; 150	97.00; 150	1500; 150	383
33	UD-66	Membrane	81.00; 80	94.50; 80	800; 80	384
34	MOF-5	Membrane	80.90; 4	99.70; 4	200; 4	183
35	UIO-66OSO_3	Membrane	86.10; 100	99.40; 100	2000; 100	385
36	MOF-801	Membrane	83.00; 120	99.20; 120	850; 120	209
37	CuZn@MOF-CC	Coating	71.70; 80	97.10; 80	450; 320	210
38	sPBIp3-CAUx	Membrane	83.03; 60	93.32; 60	200; 60	386
39	IMOF	Membrane	85.03; 100	98.00; 100	400; 100	378
40	MOF-808	Membrane	83.90; 120	97.80; 20	1600; 120	387

interaction, while simultaneously lowering the activation energy for their conversion through d–p orbital coupling between Ti sites and sulphur species. This creates nanoscale catalytic pockets inside the MOF, where both diffusion and reaction steps of the polysulphide pathway are promoted. As demonstrated in the original study, such catalytic confinement supports high areal capacity and stable cycling even at high sulphur loadings and lean electrolyte conditions–conditions under which most Li–S cathodes rapidly fail.[252]

A different yet complementary strategy is shown in Fig. 17e–g, where improved electronic conductivity is achieved through heterostructuring. Ni/Co-MOF@TCN combines a dual-metal MOF with conductive TCN nanosheets. The presence of both Ni and Co centres tunes the adsorption energy of polysulphides, striking a balance between anchoring strength and catalytic turnover, while the 2D TCN substrate ensures rapid charge transport through the composite. The reduced voltage hysteresis in galvanostatic profiles and the lower charge-transfer resistance in EIS confirm that this hybrid structure accelerates both the nucleation and decomposition steps of Li_2S_x species. This synergy demonstrates how MOFs can be integrated with high-conductivity supports to address their intrinsic electronic limitations.[253]

In parallel to cathode optimisation, functional interlayers derived from MOFs can also regulate polysulphide migration. As seen in Fig. 17h, a MgO-decorated carbon paper (obtained by MOF pyrolysis) effectively immobilises Li_2S_x species through strong ionic interaction, suppressing their diffusion compared with unmodified carbon.[254] This results in more uniform Li_2S deposition and mitigates the continuous loss of active material-a critical step toward high coulombic efficiency at practical loadings. Finally, Fig. 17i–l highlights the increasing importance of MOF-based separators in controlling polysulphide transport on the electrolyte pathway.[255] MIL-101(Cr), with its large mesoporous cages and open metal sites (Fig. 17i), provides abundant binding sites for polysulphide regulation. The strong affinity between polysulphides and dithiothreitol (DTT), demonstrated by the colour change in Fig. 17j, forms the basis for creating redox-active MOF separators. When MIL-101(Cr) is functionalised with DTT to produce

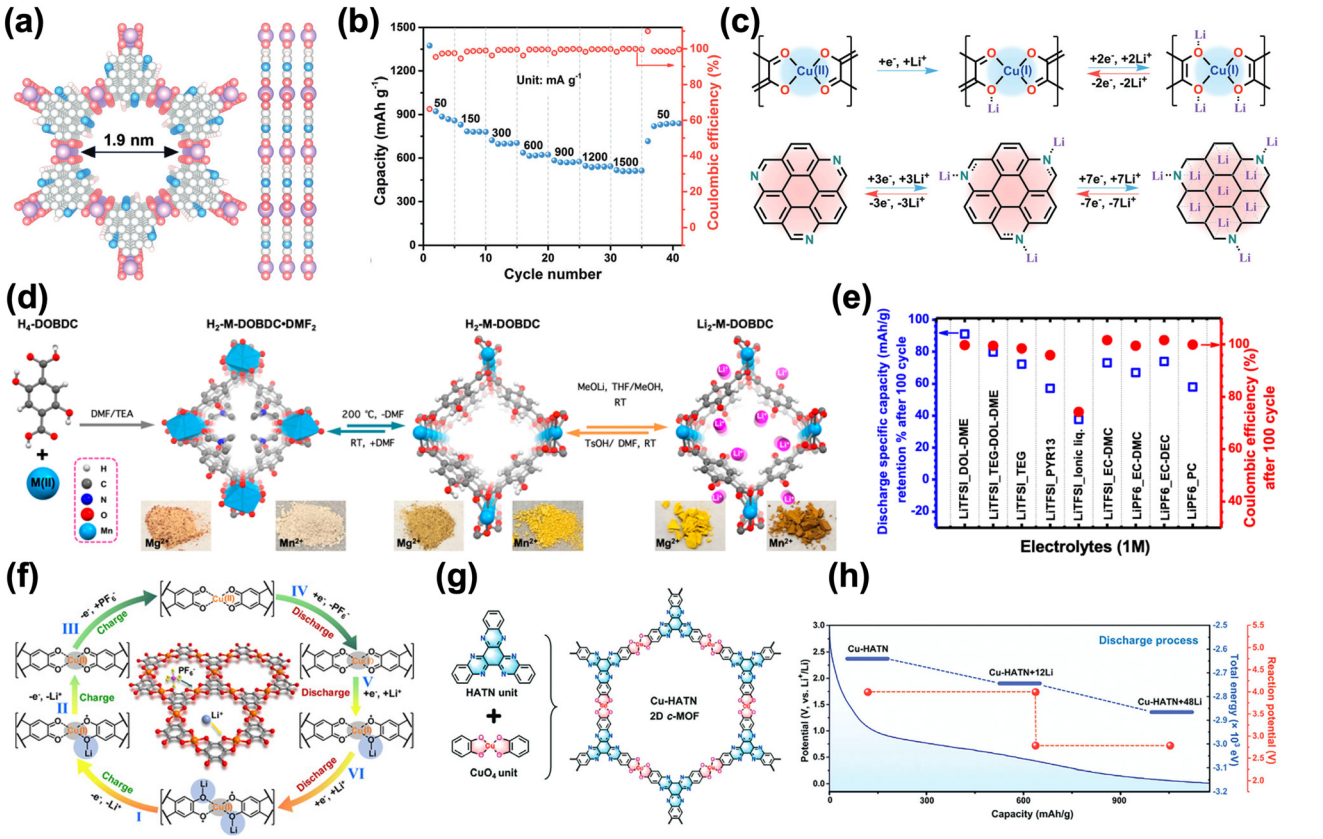

Fig. 16 (a) Calculated structural model of the Cu-TAC framework. (b) Rate performance of the Cu-TAC electrode measured across current densities ranging from 50 to 1500 mA g^{-1}. (c) Proposed Li^+ storage mechanism involving redox-active CuO_4 sites and TAC organic units. Reproduced with permission from ref. 242 Copyright 2024 John Wiley and Sons. (d) Synthetic pathways for H_2-M-DOBDC·DMF_2, H_2-M-DOBDC, and Li_2-M-DOBDC (M = Mn, Mg). (e) Discharge capacity retention and coulombic efficiency of Li_2-Mn-DOBDC electrodes after 100 cycles evaluated in different 1 M electrolyte formulations. Tests were conducted in Li half-cells within a 2.0–3.55 V window (C/2 rate), using electrodes prepared with 40 wt% Super P and 10 wt% PTFE binder. Reproduced with permission from ref. 243 Copyright 2021 American Chemical Society. (f) Illustration of Li^+ and PF_6^- insertion/extraction on Cu-THQ during charge–discharge, depicting the associated structural evolution. Reproduced with permission from ref. 244 Copyright 2020 John Wiley and Sons. (g) Synthetic scheme and molecular structure of the 2D Cu-HATN conductive MOF. (h) Proposed lithium-ion storage pathway in Cu-HATN during the discharge process. Reproduced with permission from ref. 245 Copyright 2023 John Wiley and Sons.

RM-MOF separators, the resulting structure not only traps Li_2S_x species but also catalyses their reversible conversion, substantially improving redox kinetics. This behaviour is reflected in the enhanced rate capability across 0.1–3C in Fig. 17k. The mechanistic comparison in Fig. 17l shows how separators coated with GO, DTT, MIL-101(Cr), and RM-MOF differ in their ability to suppress shuttle and maintain reaction uniformity. RM-MOF separators provide the strongest combination of adsorption, catalytic mediation, and ionic selectivity, enabling more stable long-term cycling. Overall, Fig. 17 demonstrates that MOFs can intervene at multiple points in the Li–S electrochemical system: as tuned sulphur hosts (defect-engineered MOFs), catalytic reactors (MOF-TOC), conductive hybrid structures (Ni/Co-MOF@TCN), polar trapping interlayers (MgO@C), and multifunctional separators (DTT-functionalised RM-MOFs). Each approach tackles a different bottleneck, illustrating the versatility and promise of MOF-based materials in advancing high-energy-density Li–S battery technologies.

5.6 Lithium-metal batteries

LIBs continue to dominate the rechargeable-energy landscape, delivering reliable performance for electronics, electric vehicles, and grid-level storage. Their practical energy density, however, is largely constrained by the graphite anode and oxide/phosphate cathodes, limiting full-cell values to roughly 250–300 Wh kg^{-1}. To break this ceiling, LMBs have gained increasing attention because metallic Li offers an ultrahigh specific capacity (3860 mAh g^{-1}) and the lowest redox potential-attributes that enable cell-level energy densities exceeding 400 Wh kg^{-1}.[261,262] Achieving this performance reliably requires suppressing dendrite growth, stabilizing interfaces, and regulating Li^+ flux-challenges that MOFs and COFs are emerging as powerful tools to solve due to their tunable porosity, redox activity, mechanical stability, and controllable chemistry.

The work begins with the design of conductive, redox-active COFs as interfacial regulators for metallic lithium. Ni-TAP and Ni-TAA (Fig. 18a), introduced by Ke and co-workers, feature

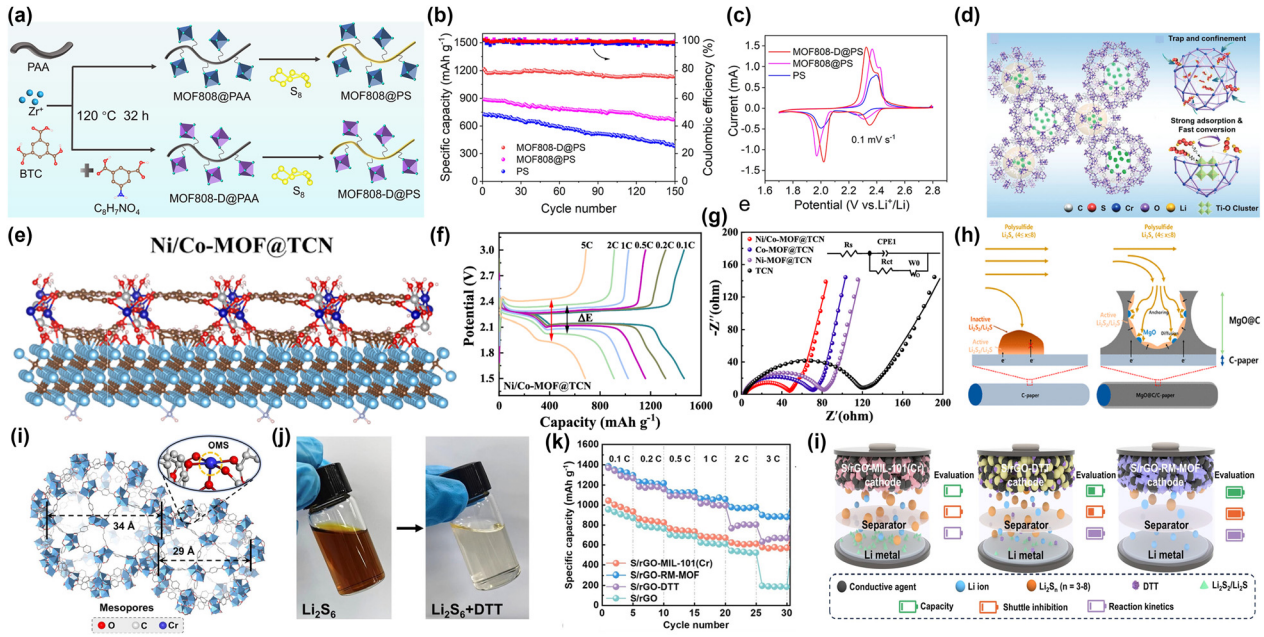

Fig. 17 (a) Schematic illustration of the synthesis routes for MOF808@PS and MOF808-D@PS sulfur composites. (b) Cycling performance of MOF808-D@PS, MOF808@PS, and pristine PS cathodes at 0.3 C. (c) Initial CV curves of the three cathodes recorded at 0.1 mV s^{-1}. Reproduced with permission from ref. 189 Copyright 2025 American Chemical Society. (d) Conceptual diagram of MOF-TOC frameworks acting as polar confinement matrices that trap polysulfides and catalyze their conversion. Reproduced with permission from ref. 252 Copyright 2023 John Wiley and Sons. (e) Synthesis schematic of the Ni/Co-MOF@TCN. (f) Galvanostatic charge–discharge profiles of Li–S cells using the Ni/Co-MOF@TCN/S cathode at various C-rates. (g) EIS of TCN, Ni-MOF@TCN, Co-MOF@TCN, and Ni/Co-MOF@TCN electrodes. Reproduced with permission from ref. 253 Copyright 2025 Elsevier. (h) Comparison of polysulfide transport on bare carbon paper (left) and MgO-coated carbon paper (right), where MgO provides strong anchoring sites that suppress shuttle effects and promote uniform Li_2S_x conversion. Reproduced with permission from ref. 254 Copyright 2023 American Chemical Society. (i) Structural representation of MIL-101(Cr) showing its large mesoporous cages (29–34 Å) and open metal sites. (j) Digital photographs showing the decolorization of Li_2S_6 solution after addition of DTT, indicating strong polysulfide adsorption. (k) Rate capability of Li–S batteries using different cathodes between 0.1 C and 3 C. (l) Schematic summary of the polysulfide shuttle, reaction kinetics, and trapping behavior in Li–S cells employing the four cathode configurations. Reproduced with permission from ref. 255 Copyright 2025 Royal Society of Chemistry.

π-extended organic linkers coordinated to Ni–bis(dithiolene) units, producing highly lithiophilic and electronically conductive 2D frameworks.[256] When used as coatings on Cu current collectors, these COFs generate uniform Li nucleation sites and buffer interfacial charge distribution. As a result, Li‖LFP full cells containing Li@Ni-TAA/Cu or Li@Ni-TAP/Cu (Fig. 18b) deliver higher capacities and much more stable coulombic efficiencies than cells using bare Cu, even at 1–5 C. This directly reflects controlled Li plating/stripping and suppression of dead-Li formation. A related strategy employs metal-covalent organic frameworks (MCOFs) as structural guiding layers. The molecular structures of TAPA-MCOF and NTBCA-MCOF (Fig. 18c) show extended networks containing metal–ligand redox sites that can interact strongly with Li^+. Their impact is seen in long-term Li‖Li symmetric cycling (Fig. 18d): electrodes modified with either MCOF maintain extremely stable and low overpotentials over hundreds of hours, in contrast to unmodified graphite felt. This behavior indicates that MCOFs stabilize the interface, homogenize current density, and prevent dendritic growth.[257]

Moving from interfacial design to solid-electrolyte engineering, Luo *et al.* developed a starfish-inspired composite membrane consisting of ZIF-8 nanoparticles embedded within a fluorinated aramid fibre scaffold and infiltrated by PEO-LiTFSI (Fig. 18e).[258] The rigid–flexible hybrid architecture raises mechanical strength while maintaining continuous ion-conduction pathways. The effect is evident in the impedance spectra in Fig. 18f, where $LiFePO_4$/Li cells incorporating this composite electrolyte show significantly lower interfacial resistance than those using PEO alone. Corresponding galvanostatic curves in Fig. 18g confirm stable capacities and reduced polarization during prolonged cycling, demonstrating how MOF nanocrystals can synergistically reinforce polymer matrices for durable LMB operation.[258] Another example of MOF-enhanced polymer electrolytes is shown in Fig. 18h–j.[259] In this system, Fe-BDC MOF is grown onto PAN fibres to create a porous, highly wettable scaffold that absorbs Li-containing ionic liquids, followed by formation of a PEO/PAN/MOF/IL composite film. The resulting membrane exhibits excellent interfacial contact with lithium and promotes uniform ion transport. This leads to remarkably steady charge–discharge voltage profiles in LFP/CPE/Li cells (Fig. 18i) under extended cycling. Its practical viability is demonstrated in Fig. 18j, where an LFP/FAEEI/Li pouch cell fabricated with this electrolyte suc-

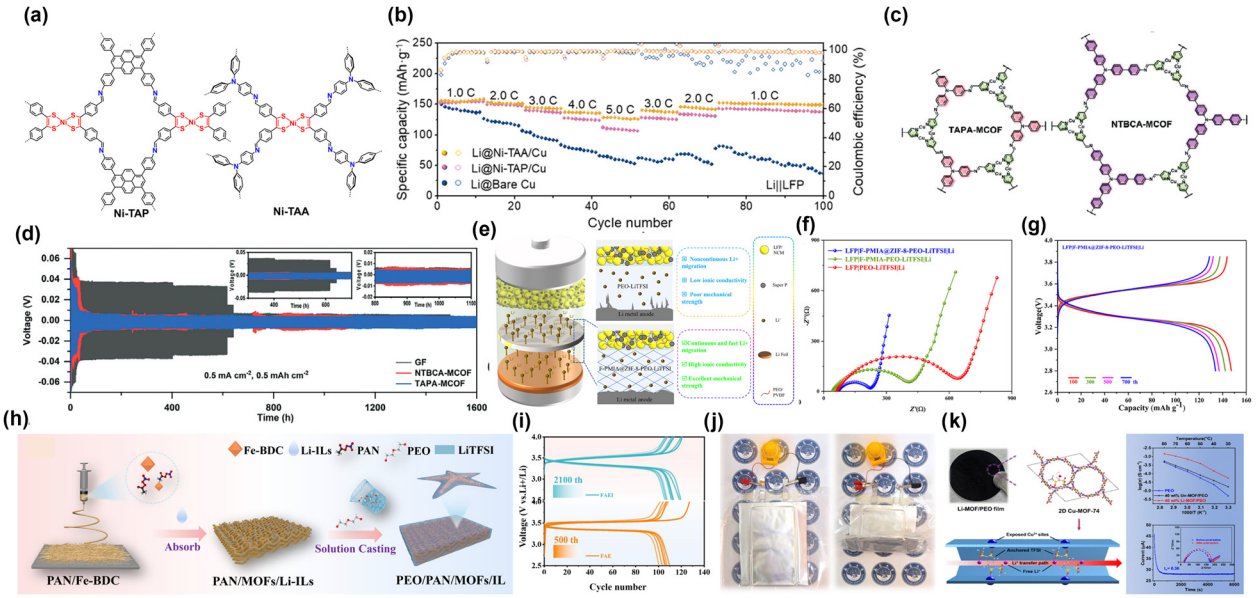

Fig. 18 (a) Molecular structures of Ni-TAP and Ni-TAA COFs. (b) Rate performance of Li||LFP full cells employing Ni-TAP/Cu and Ni-TAA/Cu anodes at current densities from 1C to 5C, compared with bare Cu. Reproduced with permission from ref. 256 Copyright 2022 American Chemical Society. (c) Structural models of TAPA-MCOF and NTBCA-MCOF. (d) Cycling stability of Li||Li symmetric cells at 0.5 mA cm^{-2}. Reproduced with permission from ref. 257 Copyright 2025 John Wiley and Sons. (e) Schematic illustration of the dendrite-free Li-metal architecture of F-PMIA@ZIF-8-PEO-LiTFSI composite electrolyte. (f) EIS spectra of LFP/Li cells. (g) Cycling performance of LFP/Li full cells at 0.5C. Reproduced with permission from ref. 258 Copyright 2023 Elsevier. (h) Fabrication pathway of MOF-enhanced CPE films, including PAN/Fe-BDC, PAN/MOFs/Li-ILs, and PEO/PAN/MOF/IL systems. (i) Charge–discharge profiles of LFP/CPE/Li cells. (j) Demonstration of an LFP/FAEEI/Li pouch cell powering a small fan. Reproduced with permission from ref. 259 Copyright 2025 John Wiley and Sons. (k) Li-MOF/PEO composite electrolyte incorporating 2D Cu-MOF-74, where exposed Cu^{2+} sites anchor $TFSI^{-}$ and create continuous Li^{+} transport channels, leading to enhanced ionic conductivity and higher Li^{+} transference number compared with pristine PEO. Reproduced with permission from ref. 260 Copyright 2022 American Chemical Society.

cessfully powers a small fan, underscoring the robustness and scalability of MOF-integrated polymer electrolytes. The final component of the figure highlights a Li-MOF/PEO composite electrolyte incorporating ultrathin Cu-MOF-74 nanosheets (Fig. 18k).[260] The exposed Cu^{2+} sites within the MOF channels immobilize $TFSI^{-}$ anions, effectively increasing the Li^{+} transference number, while the ordered pore structure provides straight, low-energy pathways for Li^{+} migration. As a combined effect, ionic conductivity rises and Li||Li symmetric cells exhibit far more stable polarization compared with pure PEO electrolytes. This approach demonstrates how even small quantities of suitably chosen 2D MOF fillers can radically reorganize ion transport in polymer hosts.

5.7 Sodium-ion batteries

Sodium-ion batteries are attracting growing interest as sustainable alternatives to lithium-ion systems owing to their low cost and the natural abundance of sodium; however, the larger ionic radius of Na^{+} imposes sluggish diffusion kinetics and severe structural stress on conventional anodes.[263,264] MOFs and MOF-derived materials offer a powerful platform to address these limitations, as their well-defined porosity, tunable vacancy chemistry, and controllable metal–ligand coordination enable precise regulation of ion-transport pathways, redox behaviour, and structural evolution.[265,266] The advances summarized in Fig. 19 illustrate how these design attributes translate into markedly improved Na-storage performance.

Recently, in Fig. 19a, Lu and co-workers demonstrate that introducing Te vacancies into a $CoTe_x$ framework anchored on a nitrogen doped porous carbon network (NSGA/$CoTe_x$@NPC) creates strong Na^{+} adsorption centres while preserving rapid charge transport through a conductive 3D backbone.[267] The resulting architecture accommodates mechanical strain effectively and delivers outstanding high-rate durability in both Na- and K-ion cells, retaining nearly full capacity over thousands of cycles. Complementary behaviour is observed in MOF-derived FeP/Fe_3O_4 composites shown in Fig. 19b and c, where the FeP/Fe_3O_4-73 composition achieves well-defined redox features and stable cycling.[268] The intimate nanoscale mixing inherited from the MOF precursor provides a favourable balance between FeP-driven electronic conductivity and Fe_3O_4-assisted structural buffering, enabling highly reversible Na-ion conversion reactions. Electronic-structure engineering is further exemplified in Fig. 19d, where Zhao and colleagues employ heteroatom-coordinated surface reconstruction to strengthen orbital hybridisation at active sites.[269] The modified electrode exhibits enhanced conductivity, a dominant capacitive contribution, and exceptional long-term cycling stability, consistent with the atomic-scale charge redistribution and DOS characteristics shown. Its ability to power multicoloured LEDs highlights the practical robustness of this design.

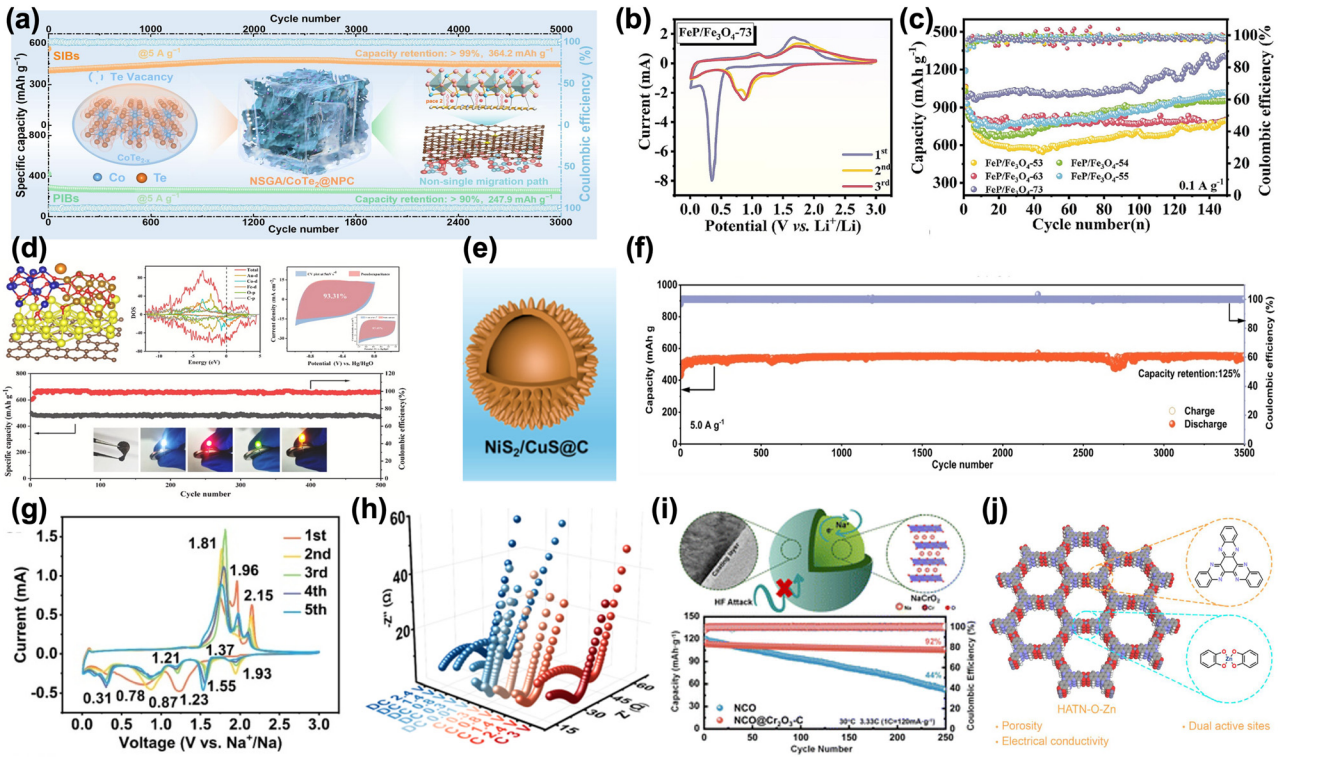

Fig. 19 (a) Structural design and dual-ion storage capability of the NSGA/$CoTe_x$@NPC anode for SIBs. Reproduced with permission from ref. 267 Copyright 2025 Elsevier. (b) CV curves of FeP/Fe_3O_4-73 at 0.2 mV s^{-1} showing characteristic redox transitions during Li^+ insertion/extraction. (c) Cycling performance of FeP/Fe_3O_4 samples at 0.1 A g^{-1} for 150 cycles. Reproduced with permission from ref. 268 Copyright 2025 Elsevier. (d) Illustration, DOS analysis, and CV response of an engineered anode material demonstrating enhanced electronic conductivity and a dominant capacitive contribution (~91.37%), accompanied by long-term cycling stability and practical LED-lighting capability. Reproduced with permission from ref. 269 Copyright 2025 Elsevier. (e) Schematic depiction of the yolk–shell NiS_2/CuS@C architecture. (f) Long-term cycling performance of NiS_2/CuS@C at 5.0 A g^{-1}, showing excellent durability. (g) CV curves of NiS_2/CuS@C at 0.1 mV s^{-1} revealing multiple reversible redox processes. (h) *Ex situ* EIS during the initial charge/discharge cycle, illustrating interfacial resistance evolution. Reproduced with permission from ref. 270 Copyright 2025 Springer Nature. (i) Illustration of the Cr_2O_3/O–C protective shell preventing HF corrosion and stabilizing Na^+ transport in NCO, resulting in significantly improved cycling stability and capacity retention compared to pristine NCO at 5.335 C. Reproduced with permission from ref. 271 Copyright 2025 Royal Society of Chemistry. (j) Schematic representation of the HATN-based 2D c-MOF (HATN-O-Zn), emphasizing its porous structure, intrinsic electrical conductivity, and dual redox-active sites. Reproduced with permission from ref. 272 Copyright 2025 John Wiley and Sons.

The advantages of MOF-derived hollow structures are captured in Fig. 19e–h, where a yolk–shell NiS_2/CuS@C framework accommodates large conversion–reaction volume changes within its internal voids while the carbon shell maintains electrical continuity.[270] The sharp reversible redox peaks, gradual reduction in interfacial resistance during activation, and strong high-rate cycling stability reflect the structural resilience imparted by this engineered architecture. Further, surface stabilisation strategies enabled by MOF chemistry are illustrated in Fig. 19i, which shows how a conformal Cr_2O_3/O–C coating derived from a MOF precursor effectively suppresses HF-induced surface degradation in NCO.[271] The protective layer promotes uniform Na^+ transport,[270] and substantially enhances capacity retention at high current densities relative to pristine NCO, underscoring the importance of interface engineering for durable SIB anodes. Finally, Fig. 19j highlights the emergence of 2D conductive MOFs such as the HATN-based HATN-O-Zn framework reported by Noh and co-workers.[272] The extended π-conjugation and ordered porosity of this material facilitate fast Na^+ diffusion, while dual redox-active sites located on both the ligand and metal units enable efficient multi-electron storage and stable cycling. Collectively, Fig. 19a–j illustrates how vacancy manipulation, electronic-structure tuning, hierarchical hollow architectures, MOF-derived protective interfaces, and conductive 2D MOF frameworks are converging to address key bottlenecks in Na-ion storage. These examples reinforce the central message that MOF-informed chemistry provides a versatile and highly tunable toolbox for creating robust, high-performance SIB anodes capable of operating under demanding electrochemical conditions.

5.8 Potassium-ion batteries

Potassium-ion batteries are being explored as a cost-effective alternative to LIBs because K is earth-abundant, easy to extract and shows high ionic mobility in common electrolytes. At the same time, conventional inorganic electrodes in PIBs suffer from sluggish diffusion, large volume changes and limited capacity.[273] In this context, conductive and porous MOFs are

attractive because their open channels, redox-active metal/ligand sites and structural tunability can be used either to host K^+ in the framework itself or to confine other active materials while buffering strain and guiding ion transport.[102] Recent work has started to use these design levers systematically, and the studies summarized in Fig. 20 illustrate how MOF chemistry is being adapted for both cathodes and anodes in PIBs. In Fig. 20a–c, Su and co-workers design an amide-functionalised 2D Cu-HBB c-MOF as a high-capacity PIB cathode.[72] The hexagonal Cu-HBB framework in Fig. 20a contains multiple redox-active sites-CuO_4 nodes, amide groups and semiquinone units-arranged in a π-conjugated sheet that promotes electronic transport. The HRTEM image in Fig. 20b confirms long-range order and dual-pore channels, consistent with the refined AA-stacked structure. DFT calculations in Fig. 20c compare the binding energies of K^+ at the Cu N_2O_2 pocket, amide oxygens and semiquinone sites, showing that all three can participate in K^+ coordination, which explains the high multi-electron capacity.[72] In a similar study reported by Yang and co-workers as seen in the schematic in Fig. 20d then visualises K^+ insertion/extraction through these similar open channels at elevated temperature (60 °C), while the charge–discharge profile in Fig. 20e demonstrates a large reversible capacity with stable plateaus, highlighting that the framework remains electrochemically and structurally robust under high-rate, high-temperature cycling.[274] Further, building on the idea that MOFs can also act as solid electrolytes or ion-sieving layers, a sulfonated MOF-808-SO_3K is employed as a single-K-ion conducting membrane. In Fig. 20f, the parent Zr-MOF-808 is post-synthetically functionalised *via* solvent-assisted ligand incorporation (SALI) to graft SO_3K groups into the pores, creating fixed anionic sites that immobilise PF_6^- and provide continuous pathways for K^+ hopping. The long-term charge–discharge trace of a symmetric K‖MOF-808-SO_3K‖K cell in Fig. 20g shows highly stable overpotentials over hundreds of hours at different current densities, demonstrating that the

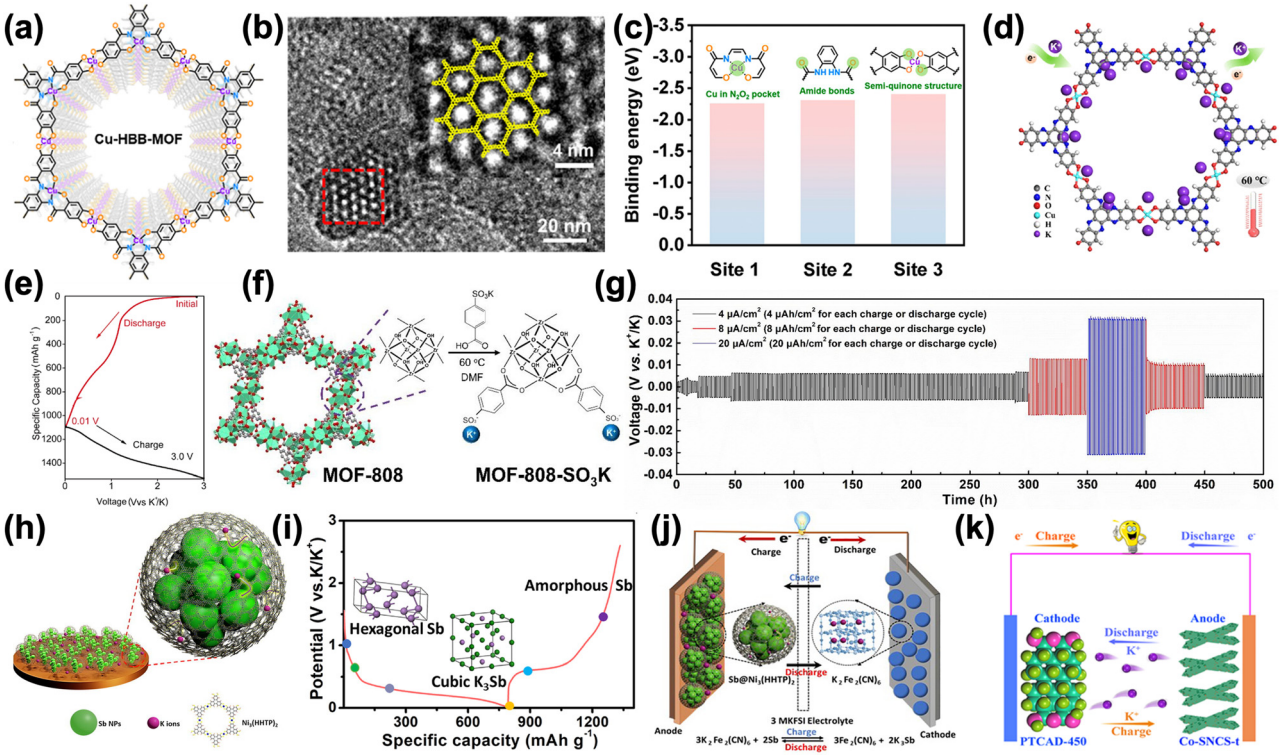

Fig. 20 (a) Molecular structure of the Cu-HBB-MOF featuring a highly ordered π-conjugated framework. (b) HRTEM image revealing its crystalline pore array. (c) Calculated binding energies for three distinct active sites, highlighting the role of Cu-N_2O_2 pockets, amide linkages, and semiquinone motifs. Reproduced with permission from ref. 72 Copyright 2016 Royal Society of Chemistry. (d) Schematic illustration of K^+ insertion/extraction through the open channels of the Cu-based conductive MOF, enabling efficient ion transport and thermal stability at 60 °C. (e) Charge–discharge profiles showing structural evolution during potassiation/depotassiation. Reproduced with permission from ref. 274 Copyright 2024 American Chemical Society. (f) Stepwise synthesis of MOF-808-SO_3K *via* SALI, with the incorporated sulfonate groups enhancing ionic pathways. (g) Long-term galvanostatic cycling of a symmetric K‖K cell employing MOF-808-SO_3K, demonstrating stable charge/discharge behavior over extended operation. Reproduced with permission from ref. 275 Copyright 2022 American Chemical Society. (h) Schematic of Sb nanoparticles encapsulated within a $Ni_3(HHTP)_2$ conductive MOF shell, where the porous lattice accommodates volume fluctuations and promotes smooth K^+ transport. (i) Potassiation/depotassiation mechanism of the Sb@$Ni_3(HHTP)_2$-10 anode, supported by *ex situ* FTIR. (j) Full-cell configuration and electrochemical performance of the Sb@$Ni_3(HHTP)_2$-10‖$K_3Fe(CN)_6$ system in 3 M KFSI electrolyte. Reproduced with permission from ref. 276 Copyright 2022 Elsevier. (k) Schematic of the PTCDA//Co-SNCS-t potassium-ion full cell operating at 45 °C. Reproduced with permission from ref. 277 Copyright 2025 Elsevier.

MOF framework can transport K^+ efficiently while suppressing parasitic reactions at the metal interface.[275] Next at the anode side, MOFs are increasingly used as conductive shells to manage alloying-type volume changes. In Fig. 20h–j, Sb nanoparticles are encapsulated by a $Ni_3(HHTP)_2$ c-MOF to form $Sb@Ni_3(HHTP)_2$.[276] The schematic in Fig. 20h illustrates how the porous, electrically conductive MOF network wraps Sb, leaving enough free volume to accommodate the large expansion during potassiation while maintaining electronic contact and offering short K^+ diffusion paths. The schematic electrochemical pathway in Fig. 20i depicts the sequential conversion from hexagonal Sb through K–Sb intermetallics to amorphous K_3Sb during discharge and the reverse process on charge, with *ex situ* spectroscopy confirming the reversibility of these transformations. Finally, Fig. 20j shows the configuration of a full K-ion cell pairing the $Sb@Ni_3(HHTP)_2$ anode with a Prussian-blue-type $K_3Fe(CN)_6$ cathode and illustrates the stable charge–discharge behaviour, underscoring that MOF-confined alloy anodes can deliver high capacity and long cycle life when integrated into practical devices.[276] To demonstrate that MOF chemistry can also be combined with organic redox frameworks, Fig. 20k summarizes a PIB full-cell concept based on a perylenetetracarboxylic dianhydride (PTCDA) cathode coupled with a Co-based layered coordination solid (Co-SNCS-t) anode.[277] The schematic highlights how both electrodes rely on well-defined, π-conjugated coordination/organic networks to provide accessible K^+ storage sites, fast charge transfer and good mechanical integrity. Together, the results in Fig. 20a–k show a clear evolution from using conductive MOFs purely as active cathodes, to ion-conducting separators, to structural/composite hosts for alloy anodes and fully coordinated organic–inorganic electrode pairs, mapping out a versatile design toolbox for next-generation PIBs. Moreover, Table 2 summarizes recent development of c-MOFs based materials employed in various types of batteries for energy storage and conversion.

Critical insight: Although c-MOFs demonstrate impressive performance across batteries, supercapacitors, and hybrid systems, many reported metrics are obtained under idealized testing conditions. Translating these results to practical devices will require standardized benchmarking, higher areal loadings, and long-term cycling studies. Emphasizing device-relevant metrics will be critical for assessing the true technological potential of c-MOF-based electrodes.

6. Emerging trends and challenges-durability, large-scale synthesis, computational design, and integration into flexible or solid-state systems

Conductive MOFs have entered a strikingly dynamic phase in their development, where emerging scientific trends and practical engineering realities are beginning to converge and redefine the boundaries of what these materials can achieve.[278] Initially celebrated for their structural elegance and unprecedented chemical programmability, c-MOFs are now being evaluated through the lens of durability and operational resilience-qualities that determine whether a material can meaningfully transition from laboratory demonstrations to real-world energy devices. This has given rise to an important trend focused on strengthening the intrinsic robustness of c-MOFs, where researchers are leveraging heterometallic nodes, stronger metal–ligand coordination motifs, mixed-valence stabilization, and topologically reinforced 2D architectures to reduce their inherent fragility. This shift reflects a new understanding: the same modularity that makes MOFs tunable can also make them vulnerable, and overcoming this requires a fundamental redesign of their structural backbone.

Simultaneously, the field has witnessed a powerful movement toward hybrid and multifunctional architectures, where c-MOFs are no longer regarded as isolated functional materials but are embedded within or anchored onto conductive networks such as graphene, carbon nanotubes, MXenes, conjugated polymers, and hierarchical carbons.[279] This integration does more than improve conductivity, it alters the way charges, ions, and mechanical stresses propagate through the material. Well-designed heterointerfaces can unlock electronic pathways that pristine MOFs cannot sustain alone, stabilize redox-active sites, buffer structural strain during cycling, and promote high-rate ion transport. This trend underscores a broader realization in the community: achieving device-level performance often requires uniting molecular precision with mesoscale engineering. Alongside this, a significant emerging trend centers on hierarchical pore engineering, as the field begins to move beyond the long-held assumption that uniform microporosity is sufficient for fast ion diffusion. Next-generation c-MOFs are being conceptualized with interconnected pore hierarchies-*meso*-micro channels, directional ion conduits, gradient pores, and programmable funnel-like pathways-to support high areal loading, efficient electrolyte penetration, and minimal ion-transport bottlenecks. Such architectures are especially important as the field shifts toward thicker electrodes, practical current densities, and commercial electrolytes.[40]

Perhaps the most transformative trend is the rapid adoption of computationally guided MOF design, where machine-learning models, large-scale linker and topology libraries, automated band-structure predictions, and stability simulations under realistic environments are accelerating discovery cycles. Instead of synthesizing hundreds of candidate MOFs, researchers can now digitally screen thousands for optimal π–d overlap, redox stability, defect tolerance, pore accessibility, and chemical robustness.[280] This approach is reshaping the philosophy of MOF development-from intuition-driven chemistry to data-assisted, predictive materials engineering-allowing the community to converge on promising candidates with unprecedented efficiency.

Parallel to these conceptual advancements, the field is also confronting the realities of manufacturing scalability and device integration. This has become one of the strongest emerging trends, driven by the recognition that many of the most celebrated c-MOFs remain confined to small-scale, solvent-

intensive, or slow crystallization routes. New synthesis strategies-including continuous-flow solvothermal reactors, microwave-assisted crystallization, electrochemical deposition of MOF nanosheets, spray-coating and slot-die casting of films, low-temperature solvothermal phase formation, and solvent-minimized protocols-seek to bridge the gap between elegant chemistry and scalable processing. This trend signals a maturing field that acknowledges that reproducibility, cost, throughput, and environmental impact are as important as conductivity or capacity.

Importantly, this review intentionally evaluates scalability and synthesis reproducibility in a comparative and integrative manner rather than as a standalone synthetic survey. Across Sections 4 and 5, high-performing case studies are contextualized alongside materials that demonstrate structural simplicity, defect tolerance, and compatibility with scalable processing routes. In particular, 2D π–d conjugated frameworks, MOF-derived carbons, and hybrid MOF–polymer or MOF–carbon architectures repeatedly emerge as more robust against batch-to-batch variability and processing-induced disorder. By contrast, frameworks requiring precise stoichiometry, slow crystallization, or highly specific solvents often exhibit outstanding intrinsic properties but face barriers to large-scale translation. This comparative perspective allows scalability and reproducibility to be assessed as emergent structure–property outcomes, rather than isolated synthetic constraints.

Finally, a rapidly expanding trend focuses on the integration of c-MOFs into practical device formats, especially flexible, wearable, and solid-state energy-storage systems. Ultrathin c-MOF nanosheets, MOF–polymer hybrid solid electrolytes, MOF-based ion-sieving interlayers, and deformable electrode architectures are emerging as promising candidates for next-generation portable and flexible electronics.[281] These directions highlight another crucial insight: materials that are intrinsically ordered and crystalline must also be mechanically adaptive if they are to operate in emerging device technologies that prioritize flexibility, safety, and compactness.

Despite these advances, several critical limitations continue to hinder the commercial translation of conductive MOFs. Foremost among these is long-term structural and electrochemical stability under realistic operating conditions, including high areal loadings, prolonged cycling, fluctuating temperatures, and exposure to commercial electrolytes. Many c-MOFs exhibit gradual loss of crystallinity, metal–ligand bond degradation, or interfacial delamination during extended operation, leading to performance decay that is not always apparent in short-term laboratory tests. In addition, maintaining high electrical conductivity while preserving porosity and mechanical integrity remains a fundamental trade-off, particularly in thick electrodes or solid-state configurations.

From a manufacturing perspective, scalable and reproducible synthesis remains a major unresolved challenge. A large fraction of high-performing c-MOFs rely on solvent-intensive, slow crystallization routes, precise stoichiometric control, or post-synthetic treatments that are difficult to translate to continuous or large-area processing. Batch-to-batch variability, sensitivity to trace impurities, and limited tolerance to structural disorder further complicate reproducibility at scale. Moreover, the cost and availability of redox-active organic linkers and transition metals, along with challenges in recycling or reprocessing MOF-based components, raise important economic and sustainability concerns.

Finally, device-level integration introduces additional barriers, including interfacial resistance between c-MOFs and current collectors, mismatch in mechanical properties within composite architectures, and limited understanding of failure mechanisms at MOF-electrolyte and MOF–polymer interfaces. Addressing these unresolved issues will require coordinated advances in framework chemistry, interfacial engineering, operando characterization, and scalable processing strategies, underscoring that commercialization of c-MOFs remains a multidisciplinary challenge rather than a single-material problem.

Looking ahead, several concrete research directions emerge that can accelerate the transition of conductive MOFs from conceptual materials to deployable energy components. First, future studies should prioritize operando and multiscale characterization-combining *in situ* spectroscopy, synchrotron techniques, and electrochemical diagnostics-to directly correlate framework degradation, defect evolution, and interfacial reconstruction with performance decay under realistic cycling conditions. Second, systematic benchmarking protocols are needed, where c-MOFs are evaluated under practical areal loadings, commercial electrolytes, and extended temperature or mechanical stress windows, enabling meaningful comparison across material families. Third, synthetic efforts should increasingly focus on chemistry-conserving scale-up strategies, such as solvent-minimized routes, continuous crystallization, and film-based growth, rather than laboratory-optimized solvothermal synthesis. Fourth, computational and data-driven approaches should move beyond property prediction toward inverse design, where target conductivities, ion transference numbers, or mechanical moduli dictate linker and metal selection. Finally, device-oriented research must emphasize interface engineering-particularly MOF–current collector, MOF–polymer, and MOF–solid electrolyte interfaces-as these junctions often govern failure modes more strongly than bulk conductivity alone. Addressing these challenges in parallel will define the next phase of conductive MOF research.

Taken together, these evolving trends paint a clear and compelling picture of where the field is heading. The future of conductive MOFs will be shaped not by a single breakthrough but by the thoughtful integration of molecular chemistry, computational intelligence, scalable manufacturing, and device-level engineering. Their ultimate success will depend on whether researchers can preserve the exquisite tunability that makes MOFs exceptional while ensuring that these properties remain intact under realistic cycling conditions, commercial electrolyte environments, high areal loadings, and mechanical or thermal stresses. If this convergence continues, c-MOFs may transition from scientifically fascinating frameworks to truly transformative materials capable of reshaping electrochemical energy storage at multiple scales-molecular, device, and system level.

7. Conclusion

In contrast to prior reviews that primarily emphasize synthetic routes or record-level electrochemical metrics, this review focuses on mechanistic differentiation, durability-aware structure–property relationships, and device-relevant constraints that ultimately govern the practical utility of conductive MOFs. By critically comparing high-performing case studies with structurally robust and scalable frameworks, we aim to move the discussion beyond performance benchmarking toward design principles that can guide future materials development. Conductive MOFs have reached an inflection point where fundamental chemistry and practical engineering are converging. Over the last decade, the field has moved beyond proving that extended π–d networks can conduct electrons and now focuses on understanding how coordination geometry, defect chemistry, pore hierarchy, and interfacial structure collectively govern transport. Importantly, a unifying insight emerging from recent studies is that charge storage and transport in c-MOFs are governed by tightly coupled electronic delocalization, redox-site accessibility, and ion-transport pathways that can be rationally co-engineered within a single crystalline framework. As this review shows, c-MOFs excel not simply because they are porous or crystalline, but because their modular chemistry allows electronic delocalization, redox accessibility, and ionic mobility to be tuned within the same framework-a level of multifunctional integration that is difficult to achieve in conventional carbons, metal oxides, or conducting polymers.

Distinct from prior reviews that emphasize either synthetic strategies, record conductivities, or isolated device demonstrations, this work provides a mechanism-centered perspective that explicitly links charge-transport pathways to structure–property–performance relationships across diverse c-MOF families. By organizing recent advances around conduction modes, coordination chemistry, defect topology, pore architecture, and interfacial design, this review highlights how molecular-level electronic structure governs macroscopic electrochemical behavior. This integrative approach enables direct comparison across batteries, supercapacitors, and hybrid systems, offering transferable design principles rather than material-specific case studies.

At the device level, c-MOFs have demonstrated impressive advances across multiple energy-storage technologies, from lithium and sodium batteries to zinc–air systems, supercapacitors, and redox-flow platforms. Their ability to stabilize redox centers, regulate ion transport, confine intermediates, and form electronically conductive pathways positions them as promising next-generation electrode and electrolyte materials. Beyond performance metrics, these studies collectively establish clear structure–property–performance relationships that provide mechanistic guidance for the rational design of future c-MOFs. Yet several barriers remain before widespread implementation: improving long-term structural integrity under cycling, expanding scalable synthesis routes, addressing interfacial mismatch in hybrid architectures, and ensuring robustness under realistic environmental and mechanical conditions.

Looking forward, future research on conductive MOFs should increasingly emphasize durability-driven design, scalable and reproducible synthesis, and predictive computational frameworks that bridge molecular-level chemistry with device-level behavior. Emerging trends-including heterometallic reinforcement, hierarchical porosity, data-driven discovery, hybrid MOF–carbon or MOF–polymer architectures, and printable or flexible processing-offer credible pathways to overcome these limitations. In particular, the integration of c-MOFs into flexible, hybrid, and solid-state energy-storage systems represents a promising direction where their ordered porosity, tunable chemistry, and intrinsic conductivity can be fully leveraged. If these developments continue to mature in parallel, c-MOFs are poised to evolve from finely tuned laboratory materials into practical, manufacturable, and durable components capable of redefining charge storage across batteries, capacitors, and solid-state devices.

Author contributions

Conceptualization and methodology: S. U. S. and H. J. Y. Investigation: S. U. S. Writing – original draft: S. U. S. Writing – review & editing: S. U. S., and H. J. Y. Visualization: S. U. S. Supervision: H. J. Y. All authors discussed the results and reviewed the manuscript.

Conflicts of interest

There are no conflicts to declare.

Data availability

No primary research results, software or code have been included and no new data were generated or analysed as part of this review.

Acknowledgements

S. U. S. acknowledges the postdoctoral fellowship program supported by Academia Sinica (AS-PD-1142-M07-2). H.-J. Yen acknowledges the financial support by National Science and Technology Council (NSTC 114-2113-M-001-018; NSTC 114-2113-M-001-015).

References

1 L. Wang, R. Fu, C. Li, X. Yang, C. Zhang, M. Ouyang, K. Wang and Q. Zhang, *Angew. Chem., Int. Ed.*, 2025, **64**, e202513165.
2 Y. Zhang, D. Ma, J. Li, C. Zhi, Y. Zhang, L. Liang, S. Mao and J.-W. Shi, *Coord. Chem. Rev.*, 2024, **517**, 215995.
3 H. Zheng, W. Yan and J. Zhang, *Electrochem. Energy Rev.*, 2025, **8**, 3.

4 Z. Ye, Y. Jiang, L. Li, F. Wu and R. Chen, *Escience*, 2023, **3**, 100107.
5 K. Wang, Y. Guo and Q. Zhang, *Small Struct.*, 2022, **3**, 2100115.
6 C. Li, K. Wang, J. Li and Q. Zhang, *Nanoscale*, 2020, **12**, 7870–7874.
7 O. M. Yaghi, M. J. Kalmutzki and C. S. Diercks, *Introduction to reticular chemistry: metal-organic frameworks and covalent organic frameworks*, John Wiley & Sons, 2019.
8 O. M. Yaghi, *ACS Cent. Sci.*, 2019, **5**, 1295–1300.
9 H. Lyu, Z. Ji, S. Wuttke and O. M. Yaghi, *Chem*, 2020, **6**, 2219–2241.
10 G. Kumar and R. Gupta, *Chem. Soc. Rev.*, 2013, **42**, 9403–9453.
11 T. D. Bennett, A. K. Cheetham, A. H. Fuchs and F.-X. Coudert, *Nat. Chem.*, 2017, **9**, 11–16.
12 Z. Ji, H. Wang, S. Canossa, S. Wuttke and O. M. Yaghi, *Adv. Funct. Mater.*, 2020, **30**, 2000238.
13 Y. Song and S. Ma, *Chem. Sci.*, 2025, **16**, 11740–11767.
14 M. A. Little and A. I. Cooper, *Adv. Funct. Mater.*, 2020, **30**, 1909842.
15 C. R. Murdock, B. C. Hughes, Z. Lu and D. M. Jenkins, *Coord. Chem. Rev.*, 2014, **258**, 119–136.
16 S. Seth and S. Jhulki, *Mater. Horiz.*, 2021, **8**, 700–727.
17 G. Férey and C. Serre, *Chem. Soc. Rev.*, 2009, **38**, 1380–1399.
18 A. G. Slater and A. I. Cooper, *Science*, 2015, **348**, aaa8075.
19 X.-Y. Yang, L.-H. Chen, Y. Li, J. C. Rooke, C. Sanchez and B.-L. Su, *Chem. Soc. Rev.*, 2017, **46**, 481–558.
20 A. Wang, Y. Ma and D. Zhao, *ACS Nano*, 2024, **18**, 22829–22854.
21 W. Fan, X. Zhang, Z. Kang, X. Liu and D. Sun, *Coord. Chem. Rev.*, 2021, **443**, 213968.
22 A. Felix Sahayaraj, H. Joy Prabu, J. Maniraj, M. Kannan, M. Bharathi, P. Diwahar and J. Salamon, *J. Inorg. Organomet. Polym. Mater.*, 2023, **33**, 1757–1781.
23 H. Daglar, H. C. Gulbalkan, G. Avci, G. O. Aksu, O. F. Altundal, C. Altintas, I. Erucar and S. Keskin, *Angew. Chem., Int. Ed.*, 2021, **60**, 7828–7837.
24 D. H. Hong, H. S. Shim, J. Ha and H. R. Moon, *Bull. Korean Chem. Soc.*, 2021, **42**, 956–969.
25 J. Guo, Y. Qin, Y. Zhu, X. Zhang, C. Long, M. Zhao and Z. Tang, *Chem. Soc. Rev.*, 2021, **50**, 5366–5396.
26 H. Musarurwa and N. T. Tavengwa, *Mater. Today Commun.*, 2022, **33**, 104823.
27 R. Abazari, S. Sanati, W. K. Fan, M. Tahir, S. Nayak, K. Parida, M. El-Shahat, R. M. Abdelhameed, D. S. Nesterov and A. M. Kirillov, *Coord. Chem. Rev.*, 2025, **523**, 216256.
28 R. Taghavi, S. Rostamnia, M. Farajzadeh, H. Karimi-Maleh, J. Wang, D. Kim, H. W. Jang, R. Luque, R. S. Varma and M. Shokouhimehr, *Inorg. Chem.*, 2022, **61**, 15747–15783.
29 H. D. Lawson, S. P. Walton and C. Chan, *ACS Appl. Mater. Interfaces*, 2021, **13**, 7004–7020.
30 E. A. Asl, M. Pooresmaeil and H. Namazi, *Mater. Chem. Phys.*, 2023, **293**, 126933.
31 N. T. T. Nguyen, T. T. T. Nguyen, S. Ge, R. K. Liew, D. T. C. Nguyen and T. Van Tran, *Nanoscale Adv.*, 2024, **6**, 1800–1821.
32 D. S. Khafaga, M. T. El-Morsy, H. Faried, A. H. Diab, S. Shehab, A. M. Saleh and G. A. Ali, *RSC Adv.*, 2024, **14**, 30201–30229.
33 D. Gong, X. Li, Y. Chen and T. Jiao, *Sustainable Mater. Technol.*, 2025, e01429.
34 B. Mohan, R. K. Gupta, A. J. Pombeiro and P. Ren, *Coord. Chem. Rev.*, 2024, **519**, 216090.
35 Y. Shen, A. Tissot and C. Serre, *Chem. Sci.*, 2022, **13**, 13978–14007.
36 H. Yuan, N. Li, W. Fan, H. Cai and D. Zhao, *Adv. Sci.*, 2022, **9**, 2104374.
37 B. Zhang, Y. Zheng, T. Ma, C. Yang, Y. Peng, Z. Zhou, M. Zhou, S. Li, Y. Wang and C. Cheng, *Adv. Mater.*, 2021, **33**, 2006042.
38 X. Lu, P. Zhang, H. Pan, P. Yin, P. Zhang, L. Yang, X. Suo, X. Cui and H. Xing, *Chem. Soc. Rev.*, 2025, **54**, 3061–3139.
39 A. Khandelwal, G. Mathew, S. Bhattacharya, A. Colsmann, G. C. Marques, M. Botros, F. Strauss, J. Xing, J. S. Raju and A. Ponnusamy, *Small*, 2025, e01703.
40 Z. A. Sandhu, M. A. Raza, N. S. Awwad, H. A. Ibrahium, U. Farwa, S. Ashraf, A. Dildar, E. Fatima, S. Ashraf and F. Ali, *Mater. Adv.*, 2024, **5**, 30–50.
41 Z. Zhu, J. Duan and S. Chen, *Small*, 2024, **20**, 2309119.
42 A. Ozcan, F.-X. Coudert, S. M. Rogge, G. Heydenrych, D. Fan, A. P. Sarikas, S. Keskin, G. Maurin, G. E. Froudakis and S. Wuttke, *J. Am. Chem. Soc.*, 2025, **147**, 23367–23380.
43 H. Li, M. Eddaoudi, M. O'Keeffe and O. M. Yaghi, *Nature*, 1999, **402**, 276–279.
44 S. S.-Y. Chui, S. M.-F. Lo, J. P. Charmant, A. G. Orpen and I. D. Williams, *Science*, 1999, **283**, 1148–1150.
45 Q. Chen, Q.-W. Chen, C. Zhuang, P.-P. Tang, N. Lin and L.-Q. Wei, *Inorg. Chem. Commun.*, 2017, **79**, 78–81.
46 N. L. Rosi, J. Eckert, M. Eddaoudi, D. T. Vodak, J. Kim, M. O'Keeffe and O. M. Yaghi, *Science*, 2003, **300**, 1127–1129.
47 G. Férey, C. Mellot-Draznieks, C. Serre, F. Millange, J. Dutour, S. Surblé and I. Margiolaki, *Science*, 2005, **309**, 2040–2042.
48 T. Loiseau, C. Serre, C. Huguenard, G. Fink, F. Taulelle, M. Henry, T. Bataille and G. Férey, *Chem. – Eur. J.*, 2004, **10**, 1373–1382.
49 K. S. Park, Z. Ni, A. P. Côté, J. Y. Choi, R. Huang, F. J. Uribe-Romo, H. K. Chae, M. O'Keeffe and O. M. Yaghi, *Proc. Natl. Acad. Sci. U. S. A.*, 2006, **103**, 10186–10191.
50 A. P. Côté, A. I. Benin, N. W. Ockwig, M. O'Keeffe, A. J. Matzger and O. M. Yaghi, *Science*, 2005, **310**, 1166–1170.
51 D. Li, A. Yadav, H. Zhou, K. Roy, P. Thanasekaran and C. Lee, *Global Challenge*, 2024, **8**, 2300244.
52 Y. Qian, F. Zhang and H. Pang, *Adv. Funct. Mater.*, 2021, **31**, 2104231.
53 X. Fang, J. Y. Choi, M. Stodolka, H. T. Pham and J. Park, *Acc. Chem. Res.*, 2024, **57**, 2316–2325.

54 S. O. Ajayi, T. H. Dolla, L. L. Sikeyi, A. O. Akinola, W. K. Maboya, X. Liu, P. R. Makgwane and M. K. Mathe, *Mater. Today Sustain*, 2024, **27**, 100899.
55 R. Zhu, L. Liu, G. Zhang, Y. Zhang, Y. Jiang and H. Pang, *Nano Energy*, 2024, **122**, 109333.
56 X. Zhang, Z. Chen, X. Liu, S. L. Hanna, X. Wang, R. Taheri-Ledari, A. Maleki, P. Li and O. K. Farha, *Chem. Soc. Rev.*, 2020, **49**, 7406–7427.
57 A. Bavykina, N. Kolobov, I. S. Khan, J. A. Bau, A. Ramirez and J. Gascon, *Chem. Rev.*, 2020, **120**, 8468–8535.
58 L. Sun, M. G. Campbell and M. Dincă, *Angew. Chem., Int. Ed.*, 2016, **55**, 3566–3579.
59 Y. Peng, S. Sanati, A. Morsali and H. García, *Angew. Chem., Int. Ed.*, 2023, **62**, e202214707.
60 L. Niu, T. Wu, M. Chen, L. Yang, J. Yang, Z. Wang, A. A. Kornyshev, H. Jiang, S. Bi and G. Feng, *Adv. Mater.*, 2022, **34**, 2200999.
61 Z. Wu, J. Xie, Z. J. Xu, S. Zhang and Q. Zhang, *J. Mater. Chem. A*, 2019, **7**, 4259–4290.
62 J. Aguila-Rosas, F. J. Cano, A. Nagaya, C. T. Quirino-Barreda, M. d, J. M. Ortiz, A. G. Vargas, I. A. Ibarra and E. Lima, *Chem. Commun.*, 2025, **61**, 11706–11731.
63 C. Verma, A. R. Pathania, I. Barsoum, K. Rhee, Y. Qiang and A. Alfantazi, *Coord. Chem. Rev.*, 2026, **549**, 217258.
64 C. Du, Y. Xu and G. Wei, *Chem. Rec.*, 2025, **25**, e202500001.
65 N. Pan, H. Zhang, B. Yang, H. Qiu, L. Li, L. Song and M. Zhang, *Chem. Commun.*, 2020, **56**, 13615–13618.
66 B. Li, J. Liu, Z. Nie, W. Wang, D. Reed, J. Liu, P. McGrail and V. Sprenkle, *Nano Lett.*, 2016, **16**, 4335–4340.
67 D. Sheberla, J. C. Bachman, J. S. Elias, C.-J. Sun, Y. Shao-Horn and M. Dincă, *Nat. Mater.*, 2017, **16**, 220–224.
68 E. Kim, J. Lee, J. Park, H. Kim and K. W. Nam, *Nano Lett.*, 2025, **25**, 619–627.
69 D. Cai, M. Lu, L. Li, J. Cao, D. Chen, H. Tu, J. Li and W. Han, *Small*, 2019, **15**, 1902605.
70 S.-W. Ke, Y. Wang, J. Su, K. Liao, S. Lv, X. Song, T. Ma, S. Yuan, Z. Jin and J.-L. Zuo, *J. Am. Chem. Soc.*, 2022, **144**, 8267–8277.
71 M. Yue, W. Chen, Y. Sheng, Y. Xiao, B. Cheng and S. Lei, *J. Energy Chem.*, 2025, **109**, 859–869.
72 X. Su, L. Cheng, X. Yan, H. Zhang, T. Wang, H.-G. Wang and L. Chen, *J. Am. Chem. Soc.*, 2025, **147**, 18338–18348.
73 D. Sheberla, L. Sun, M. A. Blood-Forsythe, S. Er, C. R. Wade, C. K. Brozek, A. Aspuru-Guzik and M. Dincă, *J. Am. Chem. Soc.*, 2014, **136**, 8859–8862.
74 M. G. Campbell, D. Sheberla, S. F. Liu, T. M. Swager and M. Dincă, *Angew. Chem., Int. Ed.*, 2015, **54**, 4349–4352.
75 L. Sun, C. H. Hendon, M. A. Minier, A. Walsh and M. Dincă, *J. Am. Chem. Soc.*, 2015, **137**, 6164–6167.
76 L. H. V. Nguyen, H. Huang, L. E. Roseng, Z. Masaud and K. Wang, *Mater. Today Energy*, 2025, **54**, 102132.
77 W. Zhao, T. Chen, W. Wang, B. Jin, J. Peng, S. Bi, M. Jiang, S. Liu, Q. Zhao and W. Huang, *Sci. Bull.*, 2020, **65**, 1803–1811.
78 Y. Jin, C. Zhao, Z. Sun, Y. Lin, L. Chen, D. Wang and C. Shen, *RSC Adv.*, 2016, **6**, 30763–30768.
79 D. Ji, H. Zhou, Y. Tong, J. Wang, M. Zhu, T. Chen and A. Yuan, *Chem. Eng. J.*, 2017, **313**, 1623–1632.
80 M. Saraf, R. Rajak and S. M. Mobin, *J. Mater. Chem. A*, 2016, **4**, 16432–16445.
81 S. Rani, S. Kapoor, B. Sharma, S. Kumar, R. Malhotra and N. Dilbaghi, *J. Alloys Compd.*, 2020, **816**, 152509.
82 J. Gu, H. Fan, C. Li, J. Caro and H. Meng, *Angew. Chem.*, 2019, **131**, 5351–5355.
83 K. Cao, W. Ye, Y. Zhang, Z. Chen, R. Zhao and W. Xue, *Chem. Eng. J.*, 2024, **489**, 151384.
84 M. A. Al-Tahan, B. Miao, S. Xu, M. Hou, M. R. Shatat, M. Asad, Y. Luo, A. E. Shrshr and J. Zhang, *Colloids Surf., A*, 2024, **682**, 132899.
85 Y. Dong, Z. Jin, H. Peng, M. Wang, S. Ma, X. Li, Y. Ren, L. Xie and J. Zhang, *Small*, 2025, **21**, 2412186.
86 S. Bibi, S. S. A. Shah, M. A. Nazir, M. H. Helal, S. M. El-Bahy, Z. M. El–Bahy, S. Ullah, M. A. Wattoo and A. u. Rehman, *Adv. Sustainable Syst.*, 2024, **8**, 2400011.
87 Y. Ji, Y. You, G. Xu, X. Yang and Y. Liu, *Chem. Eng. J.*, 2024, **483**, 149365.
88 Y. Ji, W. Li, Y. You and G. Xu, *Chem. Eng. J.*, 2024, **496**, 154009.
89 Y. Ji, W. Li, Y. You and G. Xu, *Colloids Surf., A*, 2024, **699**, 134680.
90 D. S. Shivade, A. N. Kurade, R. K. Bhosale, S. S. Kundale, A. R. Shelake, A. D. Patil, P. P. Waifalkar, R. K. Kamat, A. M. Teli and T. D. Dongale, *J. Energy Storage*, 2024, **100**, 113754.
91 Z. Zhang, Y. Jiang, Y. Du, J. Jiao, B. Liu, D. Cai and H. Shan, *Coord. Chem. Rev.*, 2025, **544**, 216970.
92 M. A. Nazir, M. Naseer, S. Ullah, K. Ahmad, M. A. Ismail, R. Iqbal, T. Najam, P. Rosaiah, M. A. Raza and S. S. A. Shah, *Inorg. Chem. Commun.*, 2024, **170**, 113262.
93 S. Zhou, Y. Kuang, H. Yang, L. Gan, X. Feng, C. Mao, L. Chen, J. Zheng and G. Ouyang, *Angew. Chem.*, 2024, **136**, e202412279.
94 X. Chu, S. Liu, B. B. Luan, Y. Zhang, Y. Xi, L. H. Shao, F. M. Zhang and Y. Q. Lan, *Angew. Chem.*, 2025, **137**, e202422940.
95 Y. Dong, J. Zhang, H. Zhang, W. Wang, B. Hu, D. Xia, K. Lin, L. Geng and Y. Yang, *Nano-Micro Lett.*, 2024, **16**, 171.
96 S. Zhang, D. K. Panda, A. Yadav, W. Zhou and S. Saha, *Chem. Sci.*, 2021, **12**, 13379–13391.
97 J. Calbo, M. J. Golomb and A. Walsh, *J. Mater. Chem. A*, 2019, **7**, 16571–16597.
98 G. Lee, G. Park and S. S. Park, *J. Am. Chem. Soc.*, 2024, **146**, 29767–29772.
99 L. Li, J. Qiu and S. Wang, *Electrochim. Acta*, 2013, **99**, 278–284.
100 S. Banerjee, R. I. Anayah, C. S. Gerke and V. S. Thoi, *ACS Cent. Sci.*, 2020, **6**, 1671–1684.
101 R. Chetry, R. Dutta, M. R. Das and P. Bharali, *Energy Fuels*, 2025, **39**, 2790–2798.
102 U. Shahzad, H. M. Marwani, M. Saeed, A. M. Asiri, R. H. Althomali and M. M. Rahman, *J. Energy Storage*, 2023, **74**, 109518.

103 L. S. Xie, G. Skorupskii and M. Dincă, *Chem. Rev.*, 2020, **120**, 8536–8580.
104 T. Ingsel and R. K. Gupta, in *Metal-Organic Framework-Based Nanomaterials for Energy Conversion and Storage*, ed. R. K. Gupta, T. A. Nguyen and G. Yasin, Elsevier, 2022, pp. 11–33, DOI: 10.1016/B978-0-323-91179-5.00003-6.
105 K. Li, J. Wang and H. Wang, *J. Mater. Chem. A*, 2024, **12**, 14245–14267.
106 P. Wu, X. Yin, Y. Zhao, F. Li, Y. Yang, N. Liu, J. Liao and T. Lan, *J. Hazard. Mater.*, 2023, **459**, 132179.
107 S. Fu, J. Zhang, X. Li, E. Jin, L. Gao, R. Dong, Z. Wang, X. Feng, H. I. Wang and M. Bonn, *Nat. Rev. Mater.*, 2025, 1–22.
108 K. Jayaramulu, S. Mukherjee, D. M. Morales, D. P. Dubal, A. K. Nanjundan, A. Schneemann, J. Masa, S. Kment, W. Schuhmann and M. Otyepka, *Chem. Rev.*, 2022, **122**, 17241–17338.
109 R. Abazari, S. Sanati, M. A. Bajaber, M. S. Javed, P. C. Junk, A. K. Nanjundan, J. Qian and D. P. Dubal, *Small*, 2024, **20**, 2306353.
110 P. Apostol, S. M. Gali, A. Su, D. Tie, Y. Zhang, S. Pal, X. Lin, V. R. Bakuru, D. Rambabu, D. Beljonne, M. Dincă and A. Vlad, *J. Am. Chem. Soc.*, 2023, **145**, 24669–24677.
111 T. Kambe, R. Sakamoto, K. Hoshiko, K. Takada, M. Miyachi, J.-H. Ryu, S. Sasaki, J. Kim, K. Nakazato and M. Takata, *J. Am. Chem. Soc.*, 2013, **135**, 2462–2465.
112 G. Xing, J. Liu, Y. Zhou, S. Fu, J.-J. Zheng, X. Su, X. Gao, O. Terasaki, M. Bonn, H. I. Wang and L. Chen, *J. Am. Chem. Soc.*, 2023, **145**, 8979–8987.
113 M. McVea, C. B. Nielsen, O. Fenwick and P. Á. Szilágyi, *Small Sci.*, 2025, **5**, 2400469.
114 S. Patel, K. McKelvey and L. Liu, *Chem. Mater.*, 2024, **36**, 10054–10087.
115 F. Zohra Zeggai, Z. Ait-Touchente, K. Bachari and A. Elaissari, *Chem. Phys. Impact*, 2025, 100864.
116 J. Wang, T. Chen, M. Jeon, J. J. Oppenheim, B. Tan, J. Kim and M. Dinca, *J. Am. Chem. Soc.*, 2024, **146**, 20500–20507.
117 J. G. Park, M. L. Aubrey, J. Oktawiec, K. Chakarawet, L. E. Darago, F. Grandjean, G. J. Long and J. R. Long, *J. Am. Chem. Soc.*, 2018, **140**, 8526–8534.
118 T. Yang, R. Xiao, F. Lu, X. Ke, M. Wang and K. Wang, *New J. Chem.*, 2025, **49**, 6674–6683.
119 R. Dong, Z. Zhang, D. C. Tranca, S. Zhou, M. Wang, P. Adler, Z. Liao, F. Liu, Y. Sun and W. Shi, *Nat. Commun.*, 2018, **9**, 2637.
120 M. Cai, Q. Loague and A. J. Morris, *J. Phys. Chem. Lett.*, 2020, **11**, 702–709.
121 T. Tanabe, L. Qu, K. Ueno, S. Takaishi, M. Yamashita, Y. Hijikata, R. Matsuda, R. Sakamoto and H. Iguchi, *Chem. Commun.*, 2025, **61**, 9500–9503.
122 S. Shukla, N. N. Joshi, S. Kadian, S. S. Sahoo and R. J. Narayan, *J. Mater. Chem. C*, 2025, **13**, 3886–3901.
123 H.-B. Luo, Q. Ren, P. Wang, J. Zhang, L. Wang and X.-M. Ren, *ACS Appl. Mater. Interfaces*, 2019, **11**, 9164–9171.
124 L. Kang, Q. Zhuang, Y. Zhang and G. Li, *Inorg. Chem.*, 2025, **64**(46), 23057–23067.
125 R. Saha, K. Gupta and C. J. Gomez Garcia, *Cryst. Growth Des.*, 2024, **24**, 2235–2265.
126 E. M. Johnson, S. Ilic and A. J. Morris, *ACS Cent. Sci.*, 2021, **7**, 445–453.
127 P. Apostol, S. M. Gali, A. Su, D. Tie, Y. Zhang, S. Pal, X. Lin, V. R. Bakuru, D. Rambabu and D. Beljonne, *J. Am. Chem. Soc.*, 2023, **145**, 24669–24677.
128 M. Yue, W. Chen, Y. Sheng, Y. Xiao, B. Cheng and S. Lei, *J. Energy Chem.*, 2025, **109**, 859–869.
129 H. Idris Abdu, S. A. Mahmood, T. Aboudou, Y. Guo, L. N. Nian, L. Xiaowei, L. Ziyu, K. Jlassi, J. K. El-Demellawi and K. Eid, *Ultrason. Sonochem.*, 2025, **121**, 107476.
130 A. Crake, K. C. Christoforidis, A. Gregg, B. Moss, A. Kafizas and C. Petit, *Small*, 2019, **15**, 1805473.
131 C. H. Hendon, D. Tiana, M. Fontecave, C. m. Sanchez, L. D'arras, C. Sassoye, L. Rozes, C. Mellot-Draznieks and A. Walsh, *J. Am. Chem. Soc.*, 2013, **135**, 10942–10945.
132 D. Feng, T. Lei, M. R. Lukatskaya, J. Park, Z. Huang, M. Lee, L. Shaw, S. Chen, A. A. Yakovenko, A. Kulkarni, J. Xiao, K. Fredrickson, J. B. Tok, X. Zou, Y. Cui and Z. Bao, *Nat. Energy*, 2018, **3**, 30–36.
133 Y. Cui, J. Yan, Z. Chen, J. Zhang, Y. Zou, Y. Sun, W. Xu and D. Zhu, *Adv. Sci.*, 2019, **6**, 1802235.
134 S. Tao, J. Wang and J. Zhang, *ACS Nano*, 2025, **19**, 9484–9512.
135 M. B. Robin and P. Day, in *Advances in inorganic chemistry and radiochemistry*, Elsevier, 1968, vol. 10, pp. 247–422.
136 J. N. Behera, D. M. D'Alessandro, N. Soheilnia and J. R. Long, *Chem. Mater.*, 2009, **21**, 1922–1926.
137 A. Ludi, *J. Chem. Educ.*, 1981, **58**, 1013.
138 D. Maspoch, D. Ruiz-Molina and J. Veciana, *Chem. Soc. Rev.*, 2007, **36**, 770–818.
139 H. Buser, D. Schwarzenbach, W. Petter and A. Ludi, *Inorg. Chem.*, 1977, **16**, 2704–2710.
140 S. Benmansour, A. Abhervé, P. Gómez-Claramunt, C. Vallés-García and C. J. Gómez-García, *ACS Appl. Mater. Interfaces*, 2017, **9**, 26210–26218.
141 P. Horcajada, S. Surblé, C. Serre, D.-Y. Hong, Y.-K. Seo, J.-S. Chang, J.-M. Grenèche, I. Margiolaki and G. Férey, *Chem. Commun.*, 2007, 2820–2822.
142 J. Yoon, Y. Seo, Y. Hwang, J. Chang, H. Leclerc, S. Wuttke, P. Bazin, A. Vimont, M. Daturi and E. Bloch, *Angew. Chem.*, 2010, **122**, 6085.
143 L. Sun, T. Miyakai, S. Seki and M. Dincă, *J. Am. Chem. Soc.*, 2013, **135**, 8185–8188.
144 M. L. Aubrey, B. M. Wiers, S. C. Andrews, T. Sakurai, S. E. Reyes-Lillo, S. M. Hamed, C.-J. Yu, L. E. Darago, J. A. Mason and J.-O. Baeg, *Nat. Mater.*, 2018, **17**, 625–632.
145 L. S. Xie, L. Sun, R. Wan, S. S. Park, J. A. DeGayner, C. H. Hendon and M. Dincă, *J. Am. Chem. Soc.*, 2018, **140**, 7411–7414.
146 A. Ahmed, C. M. Robertson, A. Steiner, T. Whittles, A. Ho, V. Dhanak and H. Zhang, *RSC Adv.*, 2016, **6**, 8902–8905.
147 S. Takaishi, M. Hosoda, T. Kajiwara, H. Miyasaka, M. Yamashita, Y. Nakanishi, Y. Kitagawa, K. Yamaguchi, A. Kobayashi and H. Kitagawa, *Inorg. Chem.*, 2009, **48**, 9048–9050.

148 Y. Kobayashi, B. Jacobs, M. D. Allendorf and J. R. Long, *Chem. Mater.*, 2010, **22**, 4120–4122.
149 W. Nan, Y. Li, J. Zhang, F. Wang, X. Liu, Z. Chen, J. Xiang, S. V. Savilov, A. V. Sobolev and L. Wang, *Surf. Coat. Technol.*, 2025, **497**, 131781.
150 S. Sun, M. Huang, P. Wang and M. Lu, *J. Electrochem. Soc.*, 2019, **166**, A1799.
151 R. Saha, K. Gupta and C. J. Gómez García, *Cryst. Growth Des.*, 2024, **24**, 2235–2265.
152 N.-S. Mussa, K. Toshtay and F. Dumeignil, *Appl. Catal., A*, 2025, **708**, 120555.
153 Y. Zhang, Q. Huang, J. Liu, J.-E. Zhou, X. Lin, A. Zeb, R. C. K. Reddy and X. Xu, *Sustainable Energy Fuels*, 2022, **6**, 2665–2691.
154 R. Ameloot, F. Vermoortele, J. Hofkens, F. C. De Schryver, D. E. De Vos and M. B. Roeffaers, *Angew. Chem., Int. Ed.*, 2012, **52**, 401.
155 Z. Fang, J. P. Dürholt, M. Kauer, W. Zhang, C. Lochenie, B. Jee, B. Albada, N. Metzler-Nolte, A. Pöppl and B. Weber, *J. Am. Chem. Soc.*, 2014, **136**, 9627–9636.
156 F. Vermoortele, M. Vandichel, B. Van de Voorde, R. Ameloot, M. Waroquier, V. Van Speybroeck and D. E. De Vos, *Angew. Chem., Int. Ed.*, 2012, **51**, 4887–4890.
157 S. Marx, W. Kleist and A. Baiker, *J. Catal.*, 2011, **281**, 76–87.
158 M. N. Khan, M. Shoeb, F. Mashkoor, K.-J. Kim, M.-S. Kang, J. Yu, H. S. Bae, I.-s. Jang and C. Jeong, *J. Energy Storage*, 2025, **127**, 117108.
159 M. Zheng, X. Zhang, C. Wu, B. Li, J. Guo, M. Wei and L. Chen, *J. Energy Storage*, 2025, **132**, 117896.
160 X. Yin, F. Yang, W. Mao, Y. Mei, J.-a. Qi, P. Li, Z. Li, T. Jiang, S. Ding and Y. Han, *Colloids Surf., A*, 2025, **707**, 135931.
161 S. Alizadeh and D. Nematollahi, *J. Am. Chem. Soc.*, 2017, **139**, 4753–4761.
162 C. McKinstry, E. J. Cussen, A. J. Fletcher, S. V. Patwardhan and J. Sefcik, *Chem. Eng. J.*, 2017, **326**, 570–577.
163 A. A. Talin, A. Centrone, A. C. Ford, M. E. Foster, V. Stavila, P. Haney, R. A. Kinney, V. Szalai, F. El Gabaly, H. P. Yoon, F. Léonard and M. D. Allendorf, *Science*, 2014, **343**, 66–69.
164 M. K. Muthukumaran, M. Govindaraj, S. Kogularasu, B. Sriram, B. K. Raja, S.-F. Wang and G.-P. Chang-Chien, *Talanta Open*, 2024, 100396.
165 W. Tang, G. Zhou, J. Cao, Z. Chen, Z. Yang, H. Huang, Y. Qu, C. Li, W. Zhang and H. Liu, *ACS Appl. Energy Mater.*, 2021, **4**, 2962–2975.
166 C. Y. Zhang, J. Yu, C. Huang, G. Cabello, X. Qi, G. W. Sun, C. Zhang, R. He, D. Yang, C. Li, J. Li, X. Qi, J. Rubio Garcia, M. Estrader, J. Arbiol, J. Y. Zhou and A. Cabot, *Commun. Mater.*, 2025, **6**, 256.
167 Y. Fang, D. Luan, Y. Chen, S. Gao and X. W. Lou, *Angew. Chem., Int. Ed.*, 2020, **59**, 2644–2648.
168 J. Liu, Y. Zhou, G. Xing, M. Qi, Z. Tang, O. Terasaki and L. Chen, *Adv. Funct. Mater.*, 2024, **34**, 2312636.
169 M. Qi, L. Cheng, H.-G. Wang, F. Cui, Q. Yang and L. Chen, *Adv. Mater.*, 2024, **36**, 2401878.
170 Y. Fang, Y. Zeng, Q. Jin, X. F. Lu, D. Luan, X. Zhang and X. W. Lou, *Angew. Chem., Int. Ed.*, 2021, **60**, 8515–8520.
171 Y. Fang, B. Y. Guan, D. Luan and X. W. Lou, *Angew. Chem., Int. Ed.*, 2019, **58**, 7739–7743.
172 Z. Xia, X. Jia, X. Ge, C. Ren, Q. Yang, J. Hu, Z. Chen, J. Han, G. Xie and S. Chen, *Angew. Chem.*, 2021, **133**, 10316–10326.
173 Z. Wang, Z. Xu, Y. Mu, B. Slater, J. Li, L. Zeng, B. Guo and K. Wang, *ACS Appl. Mater. Interfaces*, 2025, **17**, 25223–25236.
174 T. Chen, H. Xu, S. Li, J. Zhang, Z. Tan, L. Chen, Y. Chen, Z. Huang and H. Pang, *Adv. Mater.*, 2024, **36**, 2402234.
175 M. Deng, J. Sun, A. Laemont, C. Liu, L. Wang, L. Bourda, J. Chakraborty, K. Van Hecke, R. Morent and N. De Geyter, *Green Chem.*, 2023, **25**, 3069–3076.
176 W. Zhu, G. Wang, S. Zhou, Y. Min, C. Yang and J. Huang, *New J. Chem.*, 2024, **48**, 17961–17968.
177 P. Dong, X. Zhang, W. Hiscox, J. Liu, J. Zamora, X. Li, M. Su, Q. Zhang, X. Guo and J. McCloy, *Adv. Mater.*, 2023, **35**, 2211841.
178 J. W. Gittins, C. J. Balhatchet, S. M. Fairclough and A. C. Forse, *Chem. Sci.*, 2022, **13**, 9210–9219.
179 D. Wu, Z. Guo, X. Yin, Q. Pang, B. Tu, L. Zhang, Y.-G. Wang and Q. Li, *Adv. Mater.*, 2014, **26**, 3258–3262.
180 Q. Liu, Q. An, K. Zeng, M. Yang, H. Zhu, X. Liang, G. Zhao, M. Sun, Y. Zha and L. Yang, *Energy Environ. Sci.*, 2025, **18**, 4934–4948.
181 S. Wang, L. Zhang, Z. Huang, J. Sun, X. Qin, S. Song, Q. Xia, Z. Yao and Y. Yang, *J. Alloys Compd.*, 2025, 181908.
182 J. Barbosa, R. Gonçalves, A. Valverde, P. Martins, V. I. Petrenko, M. Márton, A. Fidalgo-Marijuan, R. F. de Luis, C. Costa and S. Lanceros-Méndez, *Chem. Eng. J.*, 2022, **443**, 136329.
183 J. Yuan, C. Zhang, Q. Qiu, Z.-Z. Pan, L. Fan, Y. Zhao and Y. Li, *Chem. Eng. J.*, 2022, **433**, 133564.
184 R. Naresh, K. Satchidhanandam, K. R. Ilancheran, B. Ambrose, M. Kathiresan and P. Ragupathy, *J. Mater. Chem. A*, 2024, **12**, 14669–14678.
185 Y. Xie, L. Zhou, J. Li, X. Zhang, K. Liu, H. Zhang and T. Qi, *J. Electroanal. Chem.*, 2024, **952**, 117863.
186 A. Chaouiki, M. Chafiq, R. Salghi, N. Elboughdiri, J.-H. Kang, Y. G. Ko and M. Abboud, *J. Energy Chem.*, 2025, **104**, 687–715.
187 G. Zhang, S. Hou, H. Zhang, W. Zeng, F. Yan, C. C. Li and H. Duan, *Adv. Mater.*, 2015, **27**, 2400–2405.
188 T. Jiang, F. Bu, X. Feng, I. Shakir, G. Hao and Y. Xu, *ACS Nano*, 2017, **11**, 5140–5147.
189 R. Liu, H. Cheng, W. Tai, Y. Chen, B. Zhao, Y. Sun and H. Hu, *ACS Sustainable Chem. Eng.*, 2025, **13**, 4108–4119.
190 J. Yuan, C. Zhang, T. Liu, Y. Zhen, Z.-Z. Pan and Y. Li, *J. Membr. Sci.*, 2020, **612**, 118463.
191 D. Capková, T. Kazda, O. Čech, N. Király, T. Zelenka, P. Čudek, A. Sharma, V. Hornebecq, A. S. Fedorková and M. Almáši, *J. Energy Storage*, 2022, **51**, 104419.
192 S. J. Yang, T. Kim, J. H. Im, Y. S. Kim, K. Lee, H. Jung and C. R. Park, *Chem. Mater.*, 2012, **24**, 464–470.

193 W. Kukułka, V. Montes-García, S. Sarwar, D. Pakulski, P. Samorì and A. Ciesielski, *J. Mater. Chem. A*, 2025, **13**, 22755–22760.
194 Z. Wang, T. Wu, L. Zeng, J. Peng, X. Tan, D. Yu, M. Gao and G. Feng, *Adv. Mater.*, 2025, **37**, 2500943.
195 M. Yan, Z. Bowman, Z. J. Knepp, A. Peterson, L. A. Fredin and A. J. Morris, *J. Phys. Chem. Lett.*, 2024, **15**, 11919–11926.
196 X. Deng, J. Li, S. Zhu, L. Ma and N. Zhao, *Energy Storage Mater.*, 2019, **23**, 491–498.
197 Y. Zhang, A. Pan, L. Ding, Z. Zhou, Y. Wang, S. Niu, S. Liang and G. Cao, *ACS Appl. Mater. Interfaces*, 2017, **9**, 3624–3633.
198 H. Guo, T. Li, W. Chen, L. Liu, J. Qiao and J. Zhang, *Sci. Rep.*, 2015, **5**, 13310.
199 P. Lakshmanan, S. Rengapillai, S. Marimuthu and S. Vembu, *Energies*, 2022, **15**, 7635.
200 J. Yang, B. Wang, F. Jin, Y. Ning, H. Luo, J. Zhang, F. Wang, D. Wang and Y. Zhou, *Nanoscale*, 2020, **12**, 4552–4561.
201 X. Liu, J. Wang, P. Lv, Y. Zhang, J. Li and Q. Wei, *Energy Storage Mater.*, 2024, **69**, 103382.
202 Y. Zhang, Y.-R. Wang, L. Zhou, C. Guo, M. Shi, Z. Chen, Y. Tian, Y. Chen and Y.-Q. Lan, *Coord. Chem. Rev.*, 2025, **536**, 216670.
203 P. Liu, Y. Wang, R. Lv, G. Zhang, X. Liu and L. Wang, *Energy Storage Mater.*, 2025, 104155.
204 Y. Qin, H. Wang, H. Zhang, C. Jing, P. Jia, L. Zhuo, X. Liu and J. Luo, *J. Mater. Chem. A*, 2025, **14**, 763–782.
205 Q. Xia, X. Ma, P. Qiu, G. Yuan and X. Chen, *J. Am. Chem. Soc.*, 2025, **147**, 23331–23338.
206 M. Liu, J. Zhao, H. Dong, H. Meng, D. Cao, K. Zhu, J. Yao and G. Wang, *Small*, 2024, **20**, 2405309.
207 W. Zhang, W. Qi, K. Yang, Y. Hu, F. Jiang, W. Liu, L. Du, Z. Yan and J. Sun, *Energy Storage Mater.*, 2024, **71**, 103616.
208 P. Lakshmanan, P. J. Janshirani, S. Rengapillai and M. Sivakumar, *ChemPhysChem*, 2023, **24**, e202300283.
209 L. Xin, D. Zhang, K. Qu, Y. Lu, Y. Wang, K. Huang, Z. Wang, W. Jin and Z. Xu, *Adv. Funct. Mater.*, 2021, **31**, 2104629.
210 P. Wang, K. Zhang, J. Hu and M. Zheng, *Electrochim. Acta*, 2024, **504**, 144949.
211 J.-E. Zhou, Z. Xu, Y. Li, X. Lin, Y. Wu, A. Zeb and S. Zhang, *Coord. Chem. Rev.*, 2023, **494**, 215348.
212 K. Wang, C. Chen, Y. Li, Y. Hong, H. Wu, C. Zhang and Q. Zhang, *Small*, 2023, **19**, 2300054.
213 M. Gao, Z. Wang, Z. Liu, Y. Huang, F. Wang, M. Wang, S. Yang, J. Li, J. Liu, H. Qi, P. Zhang, X. Lu and X. Feng, *Adv. Mater.*, 2023, **35**, 2305575.
214 W. Zhao, M. Jiang, W. Wang, S. Liu, W. Huang and Q. Zhao, *Adv. Funct. Mater.*, 2021, **31**, 2009136.
215 A. Zhang, Q. Zhang, H. Fu, H. Zong and H. Guo, *Small*, 2023, **19**, 2303911.
216 T. Guo, D. Zhou, L. Pang, S. Sun, T. Zhou and J. Su, *Small*, 2022, **18**, 2106360.
217 A. K. Bindra, D. Wang and Y. Zhao, *Adv. Mater.*, 2023, **35**, 2300700.
218 Y. Zhao, Q. Liang, S. M. Mugo, L. An, Q. Zhang and Y. Lu, *Adv. Sci.*, 2022, **9**, 2201039.
219 R. M. Bhattarai, K. Chhetri, N. Le, D. Acharya, S. Saud, M. C. H. P. L. Nguyen, S. J. Kim and Y. S. Mok, *Carbon Energy*, 2024, **6**, e392.
220 P. Moni, W. F. Chaves, M. Wilhelm and K. Rezwan, *J. Colloid Interface Sci.*, 2019, **542**, 91–101.
221 H. Kashani, L. Chen, Y. Ito, J. Han, A. Hirata and M. Chen, *Nano Energy*, 2016, **19**, 391–400.
222 M. R. Lukatskaya, S. Kota, Z. Lin, M.-Q. Zhao, N. Shpigel, M. D. Levi, J. Halim, P.-L. Taberna, M. W. Barsoum and P. Simon, in *MXenes*, Jenny Stanford Publishing, 2023, pp. 723–743.
223 W. H. Li, K. Ding, H. R. Tian, M. S. Yao, B. Nath, W. H. Deng, Y. Wang and G. Xu, *Adv. Funct. Mater.*, 2017, **27**, 1702067.
224 S. Zhou, X. Kong, B. Zheng, F. Huo, M. Strømme and C. Xu, *ACS Nano*, 2019, **13**, 9578–9586.
225 M. R. Lukatskaya, D. Feng, S.-M. Bak, J. W. F. To, X.-Q. Yang, Y. Cui, J. I. Feldblyum and Z. Bao, *ACS Nano*, 2020, **14**, 15919–15925.
226 M. K. Singh, S. Krishnan, K. Singh and D. K. Rai, *Energy Fuels*, 2024, **38**, 12098–12110.
227 M. Yu, D. Lin, H. Feng, Y. Zeng, Y. Tong and X. Lu, *Angew. Chem.*, 2017, **129**, 5546–5551.
228 M. Hmadeh, Z. Lu, Z. Liu, F. Gándara, H. Furukawa, S. Wan, V. Augustyn, R. Chang, L. Liao, F. Zhou, E. Perre, V. Ozolins, K. Suenaga, X. Duan, B. Dunn, Y. Yamamto, O. Terasaki and O. M. Yaghi, *Chem. Mater.*, 2012, **24**, 3511–3513.
229 S. S. Park, E. R. Hontz, L. Sun, C. H. Hendon, A. Walsh, T. Van Voorhis and M. Dincă, *J. Am. Chem. Soc.*, 2015, **137**, 1774–1777.
230 Y. Tian, G. Zeng, A. Rutt, T. Shi, H. Kim, J. Wang, J. Koettgen, Y. Sun, B. Ouyang and T. Chen, *Chem. Rev.*, 2020, **121**, 1623–1669.
231 K. Roy, A. Banerjee and S. Ogale, *ACS Appl. Mater. Interfaces*, 2022, **14**, 20326–20348.
232 N. Zhang, T. Deng, S. Zhang, C. Wang, L. Chen, C. Wang and X. Fan, *Adv. Mater.*, 2022, **34**, 2107899.
233 F. Shi, C. Chen and Z.-L. Xu, *Adv. Fiber Mater.*, 2021, **3**, 275–301.
234 Y. Ouyang, W. Gong, Q. Zhang, J. Wang, S. Guo, Y. Xiao, D. Li, C. Wang, X. Sun and C. Wang, *Adv. Mater.*, 2023, **35**, 2304685.
235 L. Xu, X. Xiao, H. Tu, F. Zhu, J. Wang, H. Liu, W. Huang, W. Deng, H. Hou and T. Liu, *Adv. Mater.*, 2023, **35**, 2303193.
236 D. Liu, Z. Shadike, R. Lin, K. Qian, H. Li, K. Li, S. Wang, Q. Yu, M. Liu and S. Ganapathy, *Adv. Mater.*, 2019, **31**, 1806620.
237 B. Zhang, L. Yang, L.-W. Wang and F. Pan, *Nano Energy*, 2019, **62**, 844–852.
238 R. Fang, K. Chen, L. Yin, Z. Sun, F. Li and H. M. Cheng, *Adv. Mater.*, 2019, **31**, 1800863.

239 C. M. Ngue, F. Baskoro, H. Q. Wong, H.-J. Yen and M.-K. Leung, *Cryst. Growth Des.*, 2022, **22**, 5872–5882.
240 F. Baskoro, C.-M. Ngue, K. B. Labasan, H. Q. Wong, M.-K. Leung and H.-J. Yen, *Energy Technol.*, 2021, **9**, 2100212.
241 F. Baskoro, H. Q. Wong, K. B. Labasan, C.-W. Cho, C.-W. Pao, P.-Y. Yang, C.-C. Chang, C.-I. Chen, C.-C. Chueh, W. Nie, H. Tsai and H.-J. Yen, *Energy Fuels*, 2021, **35**, 9669–9682.
242 J. C. Yin, X. Lian, Z. G. Li, M. Cheng, M. Liu, J. Xu, W. Li, Y. Xu, N. Li and X. H. Bu, *Adv. Funct. Mater.*, 2024, **34**, 2403656.
243 D. Rambabu, A. E. Lakraychi, J. Wang, L. Sieuw, D. Gupta, P. Apostol, G. Chanteux, T. Goossens, K. Robeyns and A. Vlad, *J. Am. Chem. Soc.*, 2021, **143**, 11641–11650.
244 Q. Jiang, P. Xiong, J. Liu, Z. Xie, Q. Wang, X.-Q. Yang, E. Hu, Y. Cao, J. Sun, Y. Xu and L. Chen, *Angew. Chem., Int. Ed.*, 2020, **59**, 5273–5277.
245 J. Yin, N. Li, M. Liu, Z. Li, X. Wang, M. Cheng, M. Zhong, W. Li, Y. Xu and X.-H. Bu, *Adv. Funct. Mater.*, 2023, **33**, 2211950.
246 X. Wang, X. Zhang, Y. Zhao, D. Luo, L. Shui, Y. Li, G. Ma, Y. Zhu, Y. Zhang and G. Zhou, *Angew. Chem.*, 2023, **135**, e202306901.
247 L. Li, H. Tu, J. Wang, M. Wang, W. Li, X. Li, F. Ye, Q. Guan, F. Zhu and Y. Zhang, *Adv. Funct. Mater.*, 2023, **33**, 2212499.
248 X. Hu, T. Huang, G. Zhang, S. Lin, R. Chen, L.-H. Chung and J. He, *Coord. Chem. Rev.*, 2023, **475**, 214879.
249 C. Zhou, M. Chen, C. Dong, H. Wang, C. Shen, X. Wu, Q. An, G. Chang, X. Xu and L. Mai, *Nano Energy*, 2022, **98**, 107332.
250 J. Liu, X. Song, T. Zhang, S. Liu, H. Wen and L. Chen, *Angew. Chem.*, 2021, **133**, 5672–5684.
251 D. Yang, Z. Liang, P. Tang, C. Zhang, M. Tang, Q. Li, J. J. Biendicho, J. Li, M. Heggen and R. E. Dunin-Borkowski, *Adv. Mater.*, 2022, **34**, 2108835.
252 Q. Zeng, L. Xu, G. Li, Q. Zhang, S. Guo, H. Lu, L. Xie, J. Yang, J. Weng and C. Zheng, *Adv. Funct. Mater.*, 2023, **33**, 2304619.
253 W. Wang, J. Si, L. Yue, W. Zhang, Q. Chen, H. Huang, F. Lin, Y. Zhao, S. Meng and L. Liu, *Chem. Eng. J.*, 2025, **507**, 160363.
254 H. Kang, J. Shin, T.-H. Kim, Y. Lee, D. Lee, J. Lee, G. Kim and E. Cho, *ACS Sustainable Chem. Eng.*, 2023, **11**, 1344–1354.
255 Q. Zeng, R. Zhang, H. Lu, J. Yang, J. Rong, J. Weng, B. Zhang, S. Xiong, Q. Zhang and S. Huang, *Energy Environ. Sci.*, 2025, **18**, 1343–1353.
256 S.-W. Ke, Y. Wang, J. Su, K. Liao, S. Lv, X. Song, T. Ma, S. Yuan, Z. Jin and J.-L. Zuo, *J. Am. Chem. Soc.*, 2022, **144**, 8267–8277.
257 W. Qin, D. Han, X. Zhang, H. Ma, Y. Wu, Z. Li, S. Bi and L. Zhai, *Adv. Mater.*, 2025, **37**, 2418638.
258 S. Luo, N. Deng, H. Wang, Q. Zeng, Y. Li, W. Kang and B. Cheng, *Chem. Eng. J.*, 2023, **474**, 145683.
259 L. Liu, L. Zhu, Y. Wang, X. Guan, Z. Zhang, H. Li, F. Wang, H. Zhang, Z. Zhang and Z. Yang, *Angew. Chem., Int. Ed.*, 2025, **64**, e202420001.
260 Z. Zhang, L. Tian, H. Zhang, H. Xu, P. Dong, Y. Zhang and D. Long, *ACS Appl. Energy Mater.*, 2022, **5**, 1095–1105.
261 W. Xu, X. Pei, C. S. Diercks, H. Lyu, Z. Ji and O. M. Yaghi, *J. Am. Chem. Soc.*, 2019, **141**, 17522–17526.
262 Q. An, Q. Liu, P. Mao, L. Duan, H. y. Zhu, L. Liu, G. Zhao, Y. Zha, L. Yang and M. Sun, *Angew. Chem., Int. Ed.*, 2025, **64**, e202422539.
263 T. S. Tedla, N. W. Hlongwa, T. T. I. Nkambule and M. A. Kebede, *Energy Rep.*, 2025, **14**, 3175–3203.
264 H. Bi, X. Sun, B. Zhao, R. Li, Y. Zhang, X. Wang, M. Zhang, D. Luo and Z. Chen, *Adv. Funct. Mater.*, 2025, e07781.
265 J.-E. Zhou, R. C. K. Reddy, A. Zhong, Y. Li, Q. Huang, X. Lin, J. Qian, C. Yang, I. Manke and R. Chen, *Adv. Mater.*, 2024, **36**, 2312471.
266 Y. Fang, B. Y. Guan, D. Luan and X. W. Lou, *Angew. Chem., Int. Ed.*, 2019, **58**, 7739–7743.
267 Z. Lu, P. Zhang, D. Li, F. Yin, J. Weng and H. Cong, *Chem. Eng. J.*, 2025, **506**, 159896.
268 H. Ou, Q. Mo, Y. Chen, Y. Liu, Y. Luo, X. Lin, Y. Wu and L. Zhang, *J. Colloid Interface Sci.*, 2025, **700**, 138333.
269 H. Zhao, W. Xu, M. Li, Z. Meng, I. Ullah, M. Z. Nawaz, J. Wang, C. Wang and P. K. Chu, *J. Power Sources*, 2025, **626**, 235793.
270 S. Wang, L. Zhang, Z. Huang, J. Sun, X. Qin, S. Song, Q. Xia, Z. Yao and Y. Yang, *J. Alloys Compd.*, 2025, **1036**, 181908.
271 Y. Luo, G. Chen, Z. Ma, X. Gao, W. Zhao, W. Tong, Y. Pu, P. Niu, W. Yao, H. Fang, M. Yang, L. Cao, W. Yin, T. Yang, M. Chu, G. Schuck, W. Ji, R. Wang and Y. Xiao, *J. Mater. Chem. A*, 2025, **13**, 21564–21574.
272 H. J. Noh, H. Qing, P. Wang, W. Li and K. A. Mirica, *Angew. Chem., Int. Ed.*, 2025, e16381.
273 A. V. B. John and M. Td, *ACS Appl. Energy Mater.*, 2020, **3**, 9478–9492.
274 M. Yang, X. Zeng, M. Xie, Y. Wang, J.-M. Xiao, R.-H. Chen, Z.-J. Yi, Y.-F. Huang, D.-S. Bin and D. Li, *J. Am. Chem. Soc.*, 2024, **146**, 6753–6762.
275 Y.-J. Gu, Y.-A. Lo, A.-C. Li, Y.-C. Chen, J.-H. Li, Y.-S. Wang, H.-K. Tian, W. Kaveevivitchai and C.-W. Kung, *ACS Appl. Energy Mater.*, 2022, **5**, 8573–8580.
276 A. Nazir, H. T. T. Le, A.-G. Nguyen, J. Kim and C.-J. Park, *Chem. Eng. J.*, 2022, **450**, 138408.
277 S. Xiong, S. Liu, K. Sun, Q. Wu, Y. Gao, Y. Zhou, L. Hou and F. Gao, *Chem. Eng. J.*, 2025, **505**, 159921.
278 G. Xu, C. Zhu and G. Gao, *Small*, 2022, **18**, 2203140.
279 H. B. Wu and X. W. Lou, *Sci. Adv.*, 2017, **3**, eaap9252.
280 H. Daglar, H. C. Gulbalkan, G. O. Aksu and S. Keskin, *Adv. Mater.*, 2024, 2405532.
281 S. Kumar, J. Kesavan and Y.-P. Fu, *J. Mater. Chem. A*, 2025, **13**, 19236–19251.
282 P. Naveenkumar, M. Maniyazagan, N. Kang, H.-W. Yang and S.-J. Kim, *Electrochim. Acta*, 2025, **513**, 145546.

283 X. Yang, C. Xu, S. Li, Y.-P. Wu, X.-Q. Wu, Y.-M. Yin and D.-S. Li, *J. Colloid Interface Sci.*, 2022, **617**, 633–640.
284 M. Pei, M. Cui, J. Y. Kim, Y. Jung and S. Kim, *Electrochim. Acta*, 2025, **537**, 146866.
285 K. Zhang, X. Mao, W. Yan, C. Li, L. He, Y. Long, M. Wu, C. Luo, H. Zeng and M. Zhang, *Small*, 2025, **21**, e07135.
286 X. Xu, J. Tang, H. Qian, S. Hou, Y. Bando, M. S. A. Hossain, L. Pan and Y. Yamauchi, *ACS Appl. Mater. Interfaces*, 2017, **9**, 38737–38744.
287 Z. Wang, C. Gao, Y. Liu, D. Li, W. Chen, Y. Ma, C. Wang and J. Zhang, *Mater. Lett.*, 2017, **193**, 216–219.
288 P. Dubey, V. Shrivastav, S. Sundriyal and P. H. Maheshwari, *ACS Appl. Nano Mater.*, 2024, **7**, 18554–18565.
289 C. Wang, Y. He, J. Xie, S. Wang, Y. Chen, X. Yang, Y. Pei, N. Shi, M.-F. Chiou and L. Xie, *Chem. Eng. J.*, 2025, 167834.
290 Y. Xie, X. Gao, H. Wang, C. G. Nuñez, F. Jiang, Q. Li, H. Bai, F. Yao and H. Yue, *Chem. Eng. J.*, 2025, 164964.
291 H. Esfandian and M. M. Sadeghi, *Electrochim. Acta*, 2025, **509**, 145352.
292 D. Nguyen, I. Schepisi and F. Amir, *Chem. Eng. J.*, 2019, **378**, 122150.
293 S. Zhou, X. Kong, B. Zheng, F. Huo, M. Strømme and C. Xu, *ACS Nano*, 2019, **13**, 9578–9586.
294 H. Wu, W. Zhang, S. Kandambeth, O. Shekhah, M. Eddaoudi and H. N. Alshareef, *Adv. Energy Mater.*, 2019, **9**, 1900482.
295 S. Bi, H. Banda, M. Chen, L. Niu, M. Chen, T. Wu, J. Wang, R. Wang, J. Feng and T. Chen, *Nat. Mater.*, 2020, **19**, 552–558.
296 R. Iqbal, M. Q. Sultan, S. Hussain, M. Hamza, A. Tariq, M. B. Akbar, Y. Ma and L. Zhi, *Adv. Mater. Technol.*, 2021, **6**, 2000941.
297 J. W. Gittins, C. J. Balhatchet, Y. Chen, C. Liu, D. G. Madden, S. Britto, M. J. Golomb, A. Walsh, D. Fairen-Jimenez and S. E. Dutton, *J. Mater. Chem. A*, 2021, **9**, 16006–16015.
298 X. Du, J. Zhang, H. Wang, Z. Huang, A. Guo, L. Zhao, Y. Niu, X. Li, B. Wu and Y. Liu, *Mater. Chem. Front.*, 2020, **4**, 243–251.
299 D. Feng, T. Lei, M. R. Lukatskaya, J. Park, Z. Huang, M. Lee, L. Shaw, S. Chen, A. A. Yakovenko and A. Kulkarni, *Nat. Energy*, 2018, **3**, 30–36.
300 S. Wechsler and F. Z. Amir, *ChemSusChem*, 2020, **13**, 1491–1495.
301 P. Zhang, M. Wang, Y. Liu, S. Yang, F. Wang, Y. Li, G. Chen, Z. Li, G. Wang and M. Zhu, *J. Am. Chem. Soc.*, 2021, **143**, 10168–10176.
302 R. Díaz, M. G. Orcajo, J. A. Botas, G. Calleja and J. Palma, *Mater. Lett.*, 2012, **68**, 126–128.
303 J. Yang, Z. Ma, W. Gao and M. Wei, *Chem. – Eur. J.*, 2017, **23**, 631–636.
304 D. Y. Lee, S. J. Yoon, N. K. Shrestha, S.-H. Lee, H. Ahn and S.-H. Han, *Microporous Mesoporous Mater.*, 2012, **153**, 163–165.
305 B. Zhang, S. Song, W. Li, L. Zheng and X. Ma, *Ionics*, 2021, **27**, 3553–3566.
306 X. Zhang, N. Qu, S. Yang, D. Lei, A. Liu and Q. Zhou, *Mater. Chem. Front.*, 2021, **5**, 482–491.
307 Y. Yan, P. Gu, S. Zheng, M. Zheng, H. Pang and H. Xue, *J. Mater. Chem. A*, 2016, **4**, 19078–19085.
308 J. Yang, P. Xiong, C. Zheng, H. Qiu and M. Wei, *J. Mater. Chem. A*, 2014, **2**, 16640–16644.
309 Y. Y. Kannangara, U. A. Rathnayake and J.-K. Song, *Electrochim. Acta*, 2019, **297**, 145–154.
310 H. Zhang, Y. Sun, X. Zhang, H. Yang and B. Lin, *Electrochim. Acta*, 2021, **389**, 138684.
311 R. Ramachandran, C. Zhao, D. Luo, K. Wang and F. Wang, *Appl. Surf. Sci.*, 2018, **460**, 33–39.
312 J. Park, M. Lee, D. Feng, Z. Huang, A. C. Hinckley, A. Yakovenko, X. Zou, Y. Cui and Z. Bao, *J. Am. Chem. Soc.*, 2018, **140**, 10315–10323.
313 Z. Wu, D. Adekoya, X. Huang, M. J. Kiefel, J. Xie, W. Xu, Q. Zhang, D. Zhu and S. Zhang, *ACS Nano*, 2020, **14**, 12016–12026.
314 L. Guo, J. Sun, W. Zhang, L. Hou, L. Liang, Y. Liu and C. Yuan, *ChemSusChem*, 2019, **12**, 5051–5058.
315 R. R. Kapaev, S. Olthof, I. S. Zhidkov, E. Z. Kurmaev, K. J. Stevenson, K. Meerholz and P. A. Troshin, *Chem. Mater.*, 2019, **31**, 5197–5205.
316 K. Wada, K. Sakaushi, S. Sasaki and H. Nishihara, *Angew. Chem., Int. Ed.*, 2018, **57**, 8886–8890.
317 Q. Jiang, P. Xiong, J. Liu, Z. Xie, Q. Wang, X. Q. Yang, E. Hu, Y. Cao, J. Sun and Y. Xu, *Angew. Chem., Int. Ed.*, 2020, **59**, 5273–5277.
318 Z. Zhu, Y. Zeng, Z. Pei, D. Luan, X. Wang and X. W. Lou, *Angew. Chem., Int. Ed.*, 2023, **62**, e202305828.
319 S. Gu, Z. Bai, S. Majumder, B. Huang and G. Chen, *J. Power Sources*, 2019, **429**, 22–29.
320 L. Guo, J. Sun, X. Sun, J. Zhang, L. Hou and C. Yuan, *Nanoscale Adv.*, 2019, **1**, 4688–4691.
321 J. Yan, Y. Cui, M. Xie, G. Z. Yang, D. S. Bin and D. Li, *Angew. Chem., Int. Ed.*, 2021, **60**, 24467–24472.
322 K. Kon, K. Uchida, K. Fuku, S. Yamanaka, B. Wu, D. Yamazui, H. Iguchi, H. Kobayashi, Y. Gambe and I. Honma, *ACS Appl. Mater. Interfaces*, 2021, **13**, 38188–38193.
323 H. Chen, Y. Xiao, C. Chen, J. Yang, C. Gao, Y. Chen, J. Wu, Y. Shen, W. Zhang and S. Li, *ACS Appl. Mater. Interfaces*, 2019, **11**, 11459–11465.
324 C.-L. Song, G.-H. Li, Y. Yang, X.-J. Hong, S. Huang, Q.-F. Zheng, L.-P. Si, M. Zhang and Y.-P. Cai, *Chem. Eng. J.*, 2020, **381**, 122701.
325 Y.-H. Liu, L.-X. Li, A.-Y. Wen, F.-F. Cao and H. Ye, *Energy Storage Mater.*, 2023, **55**, 652–659.
326 Y. Zhang, R. He, H. Liu, H. Liu and X.-x. Zhang, *Electrochim. Acta*, 2025, **517**, 145757.
327 J. Li, G. Yin, Y. Wang, Y. Xiang, N. Yu, X. Li, Y. Jiang, M. Xu and X. Zhang, *Chem. Eng. J.*, 2025, **507**, 160148.
328 X. Fan, L. Zuo, X. Shi, D. Lu, Q. Guo, J. Wang, C. Zheng, P. Xiao and Y. Chen, *ACS Nano*, 2025, **19**, 30195–30210.

329 S. Sun, B. Jin and Y. Li, *ACS Appl. Nano Mater.*, 2025, **8**, 9492–9501.
330 H. Dai, Y. Xu, Y. Han, S. Sun, X. Zhang, F. Xiong, C. Huang, C. Fang, J. Han and P. K. Chu, *ACS Appl. Mater. Interfaces*, 2023, **15**, 29170–29177.
331 S. Dong, L. Wu, M. Xue, Z. Li, D. Xiao, C. Xu, L. Shen and X. Zhang, *ACS Appl. Energy Mater.*, 2021, **4**, 1568–1574.
332 W. Shuang, H. Huang, L. Kong, M. Zhong, A. Li, D. Wang, Y. Xu and X.-H. Bu, *Nano Energy*, 2019, **62**, 154–163.
333 H. Li, T. Wang, X. Wang, G. Li, J. Shen and J. Chai, *Electrochim. Acta*, 2021, **373**, 137905.
334 W. Li, S. Hu, X. Luo, Z. Li, X. Sun, M. Li, F. Liu and Y. Yu, *Adv. Mater.*, 2017, **29**, 1605820.
335 F. Xiao, H. Wang, T. Yao, X. Zhao, X. Yang, D. Y. Yu and A. L. Rogach, *ACS Appl. Mater. Interfaces*, 2021, **13**, 18010–18020.
336 M. Qi, L. Cheng, H. G. Wang, F. Cui, Q. Yang and L. Chen, *Adv. Mater.*, 2024, **36**, 2401878.
337 X. Xu, J. Liu, J. Liu, L. Ouyang, R. Hu, H. Wang, L. Yang and M. Zhu, *Adv. Funct. Mater.*, 2018, **28**, 1707573.
338 J. C. Yin, X. Lian, J. Zhang, Z. G. Li, M. Liu, J. Pang, W. Li, Y. Xu, N. Li and X. H. Bu, *Angew. Chem., Int. Ed.*, 2025, **64**, e202510698.
339 H. Lu, J. Hu, K. Zhang, J. Zhao, S. Deng, Y. Li, B. Xu and H. Pang, *Adv. Mater.*, 2024, **36**, 2309753.
340 K. W. Nam, S. S. Park, R. Dos Reis, V. P. Dravid, H. Kim, C. A. Mirkin and J. F. Stoddart, *Nat. Commun.*, 2019, **10**, 4948.
341 S. Khan, S. Chand, P. Thippeswamy, D. Ghosh and C. Chakraborty, *Sustainable Energy Fuels*, 2025, **9**, 2698–2706.
342 Z. Sang, J. Liu, X. Zhang, L. Yin, F. Hou and J. Liang, *ACS Nano*, 2023, **17**, 3077–3087.
343 C. Yang, K. Feng, J. Chen, Z. Liu and Y. Yu, *Chem. Eng. J.*, 2025, 165857.
344 H. Ding, P. Liu, C. Liu, T. Li, W. Guo, H. Xie, G. Wang and T. Gu, *ChemSusChem*, 2025, **18**, e202401606.
345 J. Wang, C. Li, S. Zhao, R. Xia, Q. Zhang, L. Wang and Q. Lv, *Chem. Eng. J.*, 2025, **504**, 158492.
346 K. Sun, Y. Shen, J. Min, J. Pang, Y. Zheng, T. Gu, G. Wang and L. Chen, *Chem. Eng. J.*, 2023, **454**, 140394.
347 Y. Fu, Q. Wei, G. Zhang, X. Wang, J. Zhang, Y. Hu, D. Wang, L. Zuin, T. Zhou and Y. Wu, *Adv. Energy Mater.*, 2018, **8**, 1801445.
348 P. Xiao, S. Li, C. Yu, Y. Wang and Y. Xu, *ACS Nano*, 2020, **14**, 10210–10218.
349 P. Mao, H. Fan, C. Liu, G. Lan, W. Huang, Z. Li, H. Mahmoud, R. Zheng, Z. Wang and H. Sun, *Sustainable Energy Fuels*, 2022, **6**, 4075–4084.
350 S. Su, Q. Liu, J. Wang, L. Fan, R. Ma, S. Chen, X. Han and B. Lu, *ACS Appl. Mater. Interfaces*, 2019, **11**, 22474–22480.
351 J. H. Na, Y. C. Kang and S.-K. Park, *Chem. Eng. J.*, 2021, **425**, 131651.
352 E. M. Miner, T. Fukushima, D. Sheberla, L. Sun, Y. Surendranath and M. Dincă, *Nat. Commun.*, 2016, **7**, 10942.
353 N. Király, D. Capková, M. Almáši, T. Kazda, O. Čech, P. Čudek, A. S. Fedorková, M. Lisnichuk, V. Meynen and V. Zeleňák, *RSC Adv.*, 2022, **12**, 23989–24002.
354 A. González-Banciella, D. Martinez-Diaz, J. de Prado, M. V. Utrilla, M. Sánchez and A. Ureña, *J. Energy Storage*, 2024, **90**, 111904.
355 H. Hu, J. Zhang, B. Guan and X. W. Lou, *Angew. Chem., Int. Ed.*, 2016, **55**, 9514–9518.
356 Q. Xia, X. Ma, P. Qiu, G. Yuan and X. Chen, *J. Am. Chem. Soc.*, 2025, **147**(26), 23331–23338.
357 H. F. Wang, D. H. Guan, X. K. Chang, X. Y. Ma, X. Y. Yuan, X. X. Wang and J. J. Xu, *Small*, 2025, **21**, 2411747.
358 Y. V. Kaneti, J. Zhang, Y.-B. He, Z. Wang, S. Tanaka, M. S. A. Hossain, Z.-Z. Pan, B. Xiang, Q.-H. Yang and Y. Yamauchi, *J. Mater. Chem. A*, 2017, **5**, 15356–15366.
359 Z. Li and L. Yin, *ACS Appl. Mater. Interfaces*, 2015, **7**, 4029–4038.
360 J.-H. Lee, R. Kim, S. Kim, J. Heo, H. Kwon, J. H. Yang and H.-T. Kim, *Energy Environ. Sci.*, 2020, **13**, 2839–2848.
361 J. Y. Kim, Y. C. Kang, W. Ahn, S. A. Song, K. Kim, J. Y. Woo, J. Park and S. N. Lim, *J. Energy Storage*, 2024, **86**, 111225.
362 Q.-C. Jiang, J. Li, Y.-J. Yang, Y.-J. Ren, L. Dai, J.-Y. Gao, L. Wang, J.-Y. Ye and Z.-X. He, *Rare Met.*, 2023, **42**, 1214–1226.
363 C. Wang, Q. Lai, K. Feng, P. Xu, X. Li and H. Zhang, *Nano Energy*, 2018, **44**, 240–247.
364 L. Li, X. Chen, Z. Feng, Y. Jiang, L. Dai, J. Zhu, Y. Liu, L. Wang and Z. He, *Green Chem.*, 2024, **26**, 6339–6360.
365 J. Sun, H. Jiang, C. Zhao, X. Fan, C. Chao and T. Zhao, *Sci. Bull.*, 2021, **66**, 904–913.
366 Y. Liu, L. Yu, X. Liu, L. Liu and J. Xi, *J. Energy Chem.*, 2022, **72**, 545–553.
367 Y.-T. Ou, D. M. Kabtamu, A. W. Bayeh, H.-H. Ku, Y.-L. Kuo, Y.-M. Wang, N.-Y. Hsu, T.-C. Chiang, H.-C. Huang and C.-H. Wang, *Catalysts*, 2021, **11**, 1188.
368 A. M. Demeku, D. M. Kabtamu, G.-C. Chen, Y.-T. Ou, Z.-J. Huang, T.-C. Chiang, H.-C. Huang and C.-H. Wang, *ACS Appl. Mater. Interfaces*, 2024, **16**, 7047–7056.
369 Y. Li, S. Yang, Y. Zhao, N. Mubarak, M. Xu, M. Ihsan-Ul-Haq, T. Zhao, Q. Chen and J.-K. Kim, *J. Mater. Chem. A*, 2022, **10**, 5605–5613.
370 Q. Jiang, Y. Ren, Y. Yang, H. Liu, L. Wang, J. Li, L. Dai and Z. He, *Chem. Eng. J.*, 2023, **460**, 141751.
371 F. Xing, T. Liu, Y. Yin, R. Bi, Q. Zhang, L. Yin and X. Li, *Adv. Funct. Mater.*, 2022, **32**, 2111267.
372 Y. Jiang, G. Cheng, Y. Li, Z. He, J. Zhu, W. Meng, L. Dai and L. Wang, *Chem. Eng. J.*, 2021, **415**, 129014.
373 H. Sheng, Q. Ma, J.-G. Yu, X.-D. Zhang, W. Zhang, Y.-X. Yin, X. Wu, X.-X. Zeng and Y.-G. Guo, *ACS Appl. Mater. Interfaces*, 2018, **10**, 38922–38927.
374 H. J. Choi, C. Youn, S. C. Kim, D. Jeong, S. N. Lim, D. R. Chang, J. W. Bae and J. Park, *Microporous Mesoporous Mater.*, 2022, **341**, 112054.
375 B. Wu, C. Yang, F. Liu, H. Zhu, G. Xie, Z.-X. Li and Y. Yang, *Appl. Therm. Eng.*, 2023, **227**, 120384.

376 C.-K. Ho, C.-Y. V. Li, L. Gao, K.-Y. Chan, J. Chen, J. Tang, J. F. Olorunyomi, C. Liao and T. Zhao, *ACS Energy Letters*, 2021, **6**, 3769–3779.
377 Y. Jiang, G. Cheng, Y. Li, Z. He, J. Zhu, W. Meng, L. Dai and L. Wang, *Chem. Eng. J.*, 2021, **415**, 129014.
378 P. Sharma, R. Goswami, S. Neogi and V. K. Shahi, *J. Mater. Chem. A*, 2022, **10**, 11150–11162.
379 J. Yuan, X. Shi, Q. Qiu, P. Yao, Y. Xia, Y. Zhao and Y. Li, *ACS Appl. Energy Mater.*, 2022, **6**, 416–423.
380 C. Zhao, H. Wang, L. Li, L. Liu, X. Cui and H. Shi, *J. Mater. Chem. A*, 2024, **12**, 12876–12888.
381 S. Peng, L. Zhang, C. Zhang, Y. Ding, X. Guo, G. He and G. Yu, *Adv. Energy Mater.*, 2018, **8**, 1802533.
382 D. Zhang, L. Xin, Y. Xia, L. Dai, K. Qu, K. Huang, Y. Fan and Z. Xu, *J. Membr. Sci.*, 2021, **624**, 119047.
383 P. Sharma and V. K. Shahi, *ACS Appl. Mater. Interfaces*, 2023, **15**, 9171–9181.
384 J. Wu, Q. Dai, H. Zhang and X. Li, *Energy Storage Mater.*, 2021, **35**, 687–694.
385 B. Pang, F. Cui, W. Chen, X. Wang, R. Du, X. Wu, X. Yan, Y. Dai and G. He, *J. Power Sources*, 2022, **526**, 231132.
386 C. Li, T. Gao, W. Wu, X. Zhou, S. Zhang, G. Ma, X. Guan and S. Wang, *ACS Appl. Energy Mater.*, 2024, **7**, 7534–7544.
387 Y. Lu, S. Lin, H. Cao, Y. Xia, Y. Xia, L. Xin, K. Qu, D. Zhang, Y. Yu, K. Huang, W. Jing and Z. Xu, *J. Membr. Sci.*, 2023, **671**, 121347.